

國立交通大學

電子工程學系 電子研究所碩士班

碩士論文

單晶片寬頻電感設計
以及等效電路模擬及分析



**A Broadband On-Chip Inductor Design,
Modeling and Analysis**

研究生：詹仁嘉

指導教授：郭治群 博士

中華民國九十七年九月

單晶片寬頻電感設計
以及等效電路模擬及分析

**A Broadband On-Chip Inductor Design,
Modeling and Analysis**

研究生：詹仁嘉

Student : Ren-Jia Chan

指導教授：郭治群 博士

Advisor : Dr. Jyh-Chyurn Guo

國立交通大學

電子工程學系 電子研究所



Submitted to Department of Electronics Engineering & Institute of Electronics

College of Electrical and Computer Engineering

National Chiao Tung University

in partial Fulfillment of the Requirements

for the Degree of Master

In

Electronics Engineering

September 2008

Hsinchu, Taiwan, Republic of China

中華民國九十七年九月

單晶片寬頻電感設計以及等效電路模擬及分析

研究生：詹仁嘉

指導教授：郭治群博士

國立交通大學

電子工程系電子研究所

中文摘要

近年來次微米乃至奈米Si CMOS應用於通訊產品，已成為極重要之技術研發領域。而RF IC為通訊產品中最重要的building block，其設計面臨諸多問題與挑戰，其中on-chip電感設計與模擬，成為Si CMOS RF IC最佳化設計之關鍵技術。電感設計最重要的參數為品質因子(Q)、共振頻率(f_{SR})與面積等。On-chip電感往往消耗大部份晶片面積，造成單晶片電路面積微縮之瓶頸。再者On-chip電感Q值的特性往往被矽基板損耗侷限，導致Q值不佳而使電路無法達到更高頻，因Layout的不對稱也會造成port-1 與port-2 可達的Q值不相等，造成最佳化設計之困難。此外，On-chip電感模型的準確度是決定設計最佳化的一關鍵因子，往往設計者所模擬與量測的結果不一致，有許多問題皆出在元件模型的準確度，已有許多文獻提出討論，並且量測的結果直接影響汲取參數的可靠性與準確度。至於電感結構設計，對稱性已成為另一重要參數，對於廣泛使用之差動式電路設計(differential topology)，有極大影響。

本研究主題為利用 0.13 μm RF CMOS製程技術設計新的對稱電感，以應用於V-band高頻微波電路。在我們的設計中，所有尺寸的量測特性均符合共振頻率 f_{SR} 高於80 GHz的寬頻表現而且高於預訂規格的 70GHz，HFSS模擬器的電磁模擬和本研究所發展的等效電路模型enhanced T-model均可正確模擬高達 110 GHz的寬頻特性，而利用本研究團隊之前發展的簡單分析模型可以準確的預測不同尺寸的共振頻率 f_{SR} 。

透過設計小電感之實習我們可以發現一些關鍵的問題，例如集膚效應和鄰近效應為限制Q值之關鍵物理機制、高頻訊號的輸入和接地環的位置決定了電磁模擬的準確性、超高頻率的量測、和去寄生效應的方法。藉由理論分析來探討金屬線圈或是繞線在高頻操作下的能量損耗並且導致Q值的下降。推導分析模型來計算集膚效應和鄰近效應所造成的額外電阻值 R_{skin} 和 $\overline{R_{eddy}}$ ，我們所推導的模型包含頻率和幾何材料參數等之相依性，可以預測電感輸入端的阻抗 $\text{Re}(Z_{in})$ ，並且有效輔助寬頻電感的最佳化設計。



A Broadband On-Chip Inductor Design, Modeling and Analysis

Student : Ren-Jia Chan

Advisor : Dr. Jyh-Chyurn Guo

**Department of Electronic Engineering and Institute of Electronics
National Chiao Tung University**

Abstract

Si RF CMOS has become a vital technology to realize a single-chip communication integrated circuit. On-chip inductors are one of key elements, which will determine RF circuit performance in terms of gain, power, and noise. However, the on-chip inductor design faces several challenges, such as broadband and high-Q, as well as area estate. The major difficulty comes from the energy loss associated with low resistivity of the silicon substrate. The lossy substrate introduces challenges, not only in performance optimization but also in simulation and modeling. Furthermore, 2-port symmetry is one more important feature, which is desired for the widely used differential circuits for low noise and high gain design.

In this thesis, new symmetric inductors targeting for applications in V-band microwave circuits have been designed and fabricated in 0.13 μm RF CMOS process. The measured characteristics can meet broadband performance with f_{SR} higher than 80 GHz for all dimensions in the design, which is above the target of 70GHz. EM simulation (HFSS) and the developed equivalent circuit model (enhanced T-model) can simulate the broadband characteristics over 110 GHz. A simple analytical model previously derived from T-model


can precisely predict f_{SR} associated with various dimensions.

Some critical issues emerge from this practice on small inductor design, such as Q limitation due to skin effect and proximity effect, EM simulation accuracy determined by RF signal injection and guard ring placement, ultra-high frequency measurement, and de-embedding methods. A theoretical analysis has been performed to explore the mechanisms responsible for the energy losses in metal traces or coils under a high frequency operation, and the introduced Q degradation. Analytical models have been derived for calculating the excess resistances, namely R_{skin} and $\overline{R_{eddy}}$ corresponding to skin effect and proximity effect. The derived models incorporating frequency dependence, and geometry as well as material parameters can predict the input impedance $Re(Z_{in})$ and guide an optimal design for broadband inductors.



誌 謝

能夠完成此篇論文，首先要感謝我的指導老師 郭治群教授持續給我的指導與鼓勵，在研究方向和資料分析都給了我很多的意見，以及提供最好的電腦設備與研究所需的模擬軟體，讓學生有最佳的研究環境可以全力專心的研究，並且時常與學生討論研究上所遇到的問題與阻礙，讓學生可以有最清晰的思緒來面對問題。

此外要特別感謝林益民和葉致廷兩位學長，雖然與我做不一樣的研究，但也是熱心的給我很多相關的意見以及生活上的關心，讓我倍感溫馨。也感謝一起在實驗室打拼的同學，依修、冠旭、國良，因為有你們的陪伴讓我在被老師定的時候不至於太苦悶。還有實驗室的學弟們，大家一起研究模擬軟體、打球、打屁聊天、一起開戰，讓實驗室氣氛非常融洽，使我的碩士生活中在苦悶中也留下許多美好的回憶。還有感謝一起修課認識的永旭，熱心提供我很多考古題以及在研究上的討論，讓我受益匪淺。

最後還要感謝我的父母給我的栽培與鼓勵，以及毓容在精神上給我許多的支持，不管我遇到什麼樣的問題總是默默地支持我，給我鼓勵讓我萌生勇氣，一步一步地走完這段求學路。其他要感謝的人還有很多，在此一併謝過。

Contents

Chinese Abstract	i
English Abstract	iii
Acknowledgement	v
Contents	vi
Figure Captions	viii
Table Captions	xiv
Chapter 1 Introduction	
1.1 Motivation	1
1.2 Overview	2
Chapter 2 Inductor Theory and Inductor Measurement Technique	
2.1 Geometries of the inductors	5
2.2 Losses in Inductor	7
2.3 Definition of Quality Factor	8
2.4 Single-ended one-port excitation	14
2.5 Single-ended two-port excitation	19
2.6 Differential excitation	20
Chapter 3 EM Theory and Simulation for Broadband Inductor Design	
3.1 EM simulation tool and simulation method	25
3.2 HFSS for 3D EM simulation	27
3.3 HFSS simulation condition setup	31
3.4 Electromagnetic theory for inductor analysis	33
3.4.1 Conductor loss – Skin effect and proximity effect	35
3.4.2 Substrate loss – Capacitive coupling and inductive eddy current ...46	

Chapter 4 Broadband and symmetric Inductor Design

4.1 Symmetric inductor design and fabrication.....	50
4.2 EM simulation for layout optimization.....	54
4.3 De-embedding structure design for new symmetric inductors.....	57
4.4 High frequency characteristics of new symmetric inductors – measurement and EM simulation.....	61
4.5 Comparison between new symmetric inductors and conventional symmetric inductors	66
4.5.1 Two-port high frequency parameters under a single-ended excitation.....	66
4.5.2 Comparison of high frequency performance between single-ended and differential excitations – new and conventional symmetric inductors.....	68
4.6 Enhanced T-model – the equivalent circuit and model parameters....	71
4.7 Enhanced T-model simulation results and comparison with measurement for new symmetric inductors.....	73
4.7.1 Broadband Accuracy of the enhanced T-model and guideline for broadband on-chip inductor design.....	73
4.7.2 Scalability of the enhanced T-model.....	82

Chapter 5 Conclusions and Future work

.....	86
--------------	-----------

References

.....	89
--------------	-----------

Figure Captions

Chapter 2

	page
Fig. 2.1 Spiral inductor structure. (a)rectangle, (b)hexagonal, (c)octagonal, (d)circular.....	6
Fig. 2.2 Illustration of inductor layouts (a) conventional symmetric inductor (b)fully symmetric inductor (c) multi-layer stack inductor.....	7
Fig. 2.3 The electric and magnetic substrate losses in an on-chip inductor.....	8
Fig. 2.4 Inductor with a series resistance.....	9
Fig. 2.5 Inductor with a parallel resistance.....	10
Fig. 2.6 Parallel RLC circuit.....	11
Fig. 2.7 Alternative method for determining the Q in real inductors.....	14
Fig. 2.8 Cross-section of a spiral inductor.....	15
Fig. 2.9 π -Model.....	15
Fig. 2.10 A single- π model as a simple two-port equivalent circuit for on-chip inductors.....	15
Fig. 2.11 Y-parameter conversion for a single- π network with port-2 grounded.....	16
Fig. 2.12 Two-port single- π equivalent circuit with port-2 grounded.....	17
Fig. 2.13 A single- π model for an on-chip inductor with a single-ended excitation.....	18
Fig. 2.14 An equivalent circuit conversion for a single- π model under a singled-ended excitation to a parallel RLC network where the original network consisting of C_{ox1} series with C_{sub1} shunt R_{sub1} in Fig.2.12 is replaced by C_{o1} shunt R_{o1}	18
Fig. 2.15 Two-port single- π equivalent circuit with both ports terminated with Z_0	19
Fig. 2.16 A lumped element π -model for a differential excitation.....	21
Fig. 2.17 An equivalent circuit conversion for a lumped element π model under a differential excitation to a parallel RLC network.....	21

Chapter 3

Fig. 3.1	The device cross section and representative π -model for an inductor integrated on Si substrate.....	25
Fig. 3.2	Vertical mode with RF signal injection at top metal (M8) and grounded ring (GR) at M1.....	28
Fig. 3.3	Horizontal mode with RF signal injection and grounded ring (GR), both at top metal (M8).....	29
Fig. 3.4	Horizontal mode with RF signal injection at top metal (M8) and ground ring (GR) at M1.....	30
Fig. 3.5	Comparison between measurement and HFSS simulation using horizontal injection mode with different guard ring (GR) layouts, at M1 and M8 respectively. (a) $\text{Im}(Z_{in})/\omega$ (b) $\text{Re}(Z_{in})$ (c) $R_s=\text{Re}(-1/Y_{21})$, and (d) $Q=\text{Im}(Z_{in})/\text{Re}(Z_{in})$	31
Fig. 3.6	Inductor structure setup for HFSS simulation (a) a 3D structure incorporating spiral inductor and guard ring (2) a 2D layout from a projection of the original 3D structure in (a).....	32
Fig. 3.7	(a) Multi-layer metals and inter-metal dielectrics with various dielectric constants and thicknesses and Effective oxide dielectric constant and thickness (b) effective dielectric constant representing the composite dielectric layers.....	33
Fig. 3.8	EM (HFSS) simulation reveals skin effect apparent in the conductors in which non-uniform current distribution and current crowding near surface will lead to increase of effective resistance in conductors under high frequency operation.....	35
Fig. 3.9	The cross section and skin depth definition in a metal line for the analysis of non-uniform current distribution under high frequency operation.....	36
Fig. 3.10	Current density distribution in the multi-turn metal coils of an inductor, at very low frequency 0.01 GHz. The EM simulation done by HFSS indicates a perfect uniform distribution in the metal trace, free from current crowding effect.....	38
Fig. 3.11	Current density distribution in the multi-turn metal coils of an inductor, at very high frequency, 10 GHz. The EM simulation done by HFSS indicates a dramatic non-uniform current distribution in the metal trace, accounting for proximity effect.....	39
Fig. 3.12	Eddy currents generated according to Lenz's law, with a direction in phase with excitation current on the inner edge (near the center of spiral coils) but opposite to the excitation current on the outer edge. The phenomenon explains current crowding caused by proximity effect in multi-turn spiral	

	inductors.....	40
Fig. 3.13	Eddy currents generated according to Lenz’s law, with a direction in phase with excitation current on the inner edge (near the center of spiral coils) but opposite to the excitation current on the outer edge. The phenomenon explains current crowding caused by proximity effect in multi-turn spiral inductors.....	41
Fig. 3.14	Cross section of a metal trace showing the normal magnetic field $B(x, y)$, and eddy current flowing round the edges within a width of w_{ed}	42
Fig. 3.15	Cross section of a metal trace showing the normal magnetic field $B(x, y)$, and eddy current flowing within a width w_{ed} round the edges.....	44
Fig. 3.16	Analysis of input impedance $\text{Re}(Z_{in})$ for conventional symmetric inductor by full wave EM simulation and simplified model incorporating proximity effect. The comparison with measurement indicates the simplified model with proximity effect only under-estimates $\text{Re}(Z_{in})$	48
Fig. 3.17	Analysis of input impedance $\text{Re}(Z_{in})$ for quadruple semi-symmetric inductor (new design for broadband applications) by full wave EM simulation and analytical model incorporating proximity effect. The comparison with measurement indicates the simplified model with proximity effect can fit $\text{Re}(Z_{in})$ of quadruple semi-symmetric inductor....	48
Chapter 4		
Fig. 4.1	The layout of a conventional differential inductor.....	50
Fig. 4.2	The layout of a fully symmetrical inductor.....	52
Fig. 4.3	The layout of a quadruple symmetric inductor.....	52
Fig. 4.4	The layout of a quadruple semi-symmetric inductor.....	53
Fig. 4.5	The series resistances due to skin effect and proximity effect R_{skin} and $\overline{R_{eddy}}$ calculated by (3.36) and (3.37) under specified metal thickness $t = 3.35\mu m$ and over varying widths $w = 1 \sim 15\mu m$, associated with different operating frequencies $f = 1, 5, 10, 15, 20 GHz$	56
Fig. 4.6	The total series resistance consisting of R_{skin} and $\overline{R_{eddy}}$ calculated by (3.38) under specified metal thickness $t = 3.35\mu m$ and over varying widths $w = 1 \sim 15\mu m$, associated with different operating frequencies $f = 1, 5, 10, 15, 20 GHz$	57
Fig. 4.7	On-wafer measurement setup with Agilent E8364B PNA and probe station for two-port test structures.....	58

Fig. 4.8	Coplanar GSG RF probes with the device under test (DUT) at the center enclosed by the pair of GSG pads.....	58
Fig. 4.9	The layouts of a Quadruple symmetric inductor and open dummy pads for open de-embedding.....	60
Fig. 4.10	The schematics and procedure for illustrating open-pad de-embedding method.....	60
Fig. 4.11	Comparison between measurement and HFSS simulation with two conventional (vertical mode) and new (horizontal mode) setups, for a quadruple symmetric inductor with a small dimension of $R=10\mu\text{m}$, $W=6\mu\text{m}$ (a) magnitude(S_{11}) (b) phase(S_{11}) (c) magnitude(S_{21}) (d) phase(S_{21}).....	63
Fig. 4.12	Comparison between measurement and HFSS simulation with two conventional (vertical mode) and new (horizontal mode) setups, for a quadruple symmetric inductor with a small dimension of $R=10\mu\text{m}$, $W=6\mu\text{m}$ (a) $L= \text{Im}(Z_{in})/\omega$ (b) $\text{Re}(Z_{in})$ (c) $\text{Re}(-1/Y_{21})$ (d) Q	63
Fig. 4.13	Comparison between measurement and HFSS simulation with two conventional (vertical mode) and new (horizontal mode) setups, for a quadruple symmetric inductor with a small dimension of $R=20\mu\text{m}$, $W=6\mu\text{m}$ (a) magnitude(S_{11}) (b) phase(S_{11}) (c) magnitude(S_{21}) (d) phase(S_{21}).....	64
Fig. 4.14	Comparison between measurement and HFSS simulation with two conventional (vertical mode) and new (horizontal mode) setups, for a quadruple symmetric inductor with a small dimension of $R=20\mu\text{m}$, $W=6\mu\text{m}$ (a) $L= \text{Im}(Z_{in})/\omega$ (b) $\text{Re}(Z_{in})$ (c) $\text{Re}(-1/Y_{21})$ (d) Q	64
Fig. 4.15	Comparison between measurement and HFSS simulation with two conventional (vertical mode) and new (horizontal mode) setups, for a quadruple symmetric inductor with a small dimension of $R=30\mu\text{m}$, $W=6\mu\text{m}$ (a) magnitude(S_{11}) (b) phase(S_{11}) (c) magnitude(S_{21}) (d) phase(S_{21}).....	65
Fig. 4.16	Comparison between measurement and HFSS simulation with two conventional (vertical mode) and new (horizontal mode) setups, for a quadruple symmetric inductor with a small dimension of $R=30\mu\text{m}$, $W=6\mu\text{m}$ (a) $L= \text{Im}(Z_{in})/\omega$ (b) $\text{Re}(Z_{in})$ (c) $\text{Re}(-1/Y_{21})$ (d) Q	65
Fig. 4.17	Comparison between the conventional and quadruple symmetric inductors in the measured S-parameters over frequencies in 1~110GHz (a) magnitude (S_{11}) (b) phase(S_{11}) (c) magnitude (S_{21}) (d) phase(S_{21}). The coil radius and metal trace width are $R=30\mu\text{m}$ and $W=6\mu\text{m}$ for both conventional and quadruple symmetric inductors.....	67

Fig. 4.18	Comparison between the conventional and quadruple symmetric inductors in performance parameters derived from S-parameters over frequencies in 1~110GHz (a) $L = \text{Im}(Z_{in})/\omega$ (b) $\text{Re}(Z_{in})$ (c) $\text{Re}(-1/Y_{21})$ (d) Q. The coil radius and metal trace width are $R=30\mu\text{m}$ and $W=6\mu\text{m}$ for both conventional and quadruple symmetric inductors.....	68
Fig. 4.19	Comparison of Z_{in} under a single-ended excitation and Z_d under a differential excitation from measurement and HFSS simulation (a) $\text{Re}(Z_{in})$ and $\text{Re}(Z_d)$ (b) $\text{Im}(Z_{in})/\omega$ and $\text{Im}(Z_d)/\omega$ for quadruple symmetric inductors (c) $\text{Re}(Z_{in})$ and $\text{Re}(Z_d)$ (d) $\text{Im}(Z_{in})/\omega$ and $\text{Im}(Z_d)/\omega$ for conventional symmetric inductors. The coil radius and metal trace width are $R=30\mu\text{m}$ and $W=6\mu\text{m}$ for both conventional and quadruple symmetric inductors.....	70
Fig. 4.20	Comparison of Q_{se} under a single-ended excitation and Q_d under a differential excitation from measurement and HFSS simulation (a) Q_{se} and Q_d for quadruple symmetric inductors (b) Q_{se} and Q_d for conventional symmetric inductors. The coil radius and metal trace width are $R=30\mu\text{m}$ and $W=6\mu\text{m}$ for both conventional and quadruple symmetric inductors.....	70
Fig. 4.21	The enhanced T-model for on-chip quadruple symmetric and semi-symmetric inductors.....	71
Fig. 4.22	Comparison of S_{11} and S_{21} between measurement and simulation by enhanced T-model for quadruple symmetric inductor with $R=10$ and $W=6\mu\text{m}$ (a) $\text{Mag}(S_{11})$ (b) $\text{Phase}(S_{11})$ (c) $\text{Mag}(S_{21})$ (d) $\text{Phase}(S_{21})$	76
Fig. 4.23	Comparison of high frequency impedances and Q between measurement and simulation by enhanced T-model for quadruple symmetric inductor, $R=10$, $W=6\mu\text{m}$ (a) $L=\text{Im}(Z_{in})/\omega$ (b) $\text{Re}(Z_{in})$ (c) $\text{Re}(-1/Y_{21})$ (d) Q.....	76
Fig. 4.24	Comparison of S_{11} and S_{21} between measurement and simulation by enhanced T-model for quadruple symmetric inductor with $R=20\mu\text{m}$ and $W=6\mu\text{m}$ (a) $\text{Mag}(S_{11})$ (b) $\text{Phase}(S_{11})$ (c) $\text{Mag}(S_{21})$ (d) $\text{Phase}(S_{21})$	77
Fig. 4.25	Comparison of high frequency impedances and Q between measurement and simulation by enhanced T-model for quadruple symmetric inductor, $R=20\mu\text{m}$, $W=6\mu\text{m}$ (a) $L=\text{Im}(Z_{in})/\omega$ (b) $\text{Re}(Z_{in})$ (c) $\text{Re}(-1/Y_{21})$ (d) Q.....	77
Fig. 4.26	Comparison of S_{11} and S_{21} between measurement and simulation by enhanced T-model for quadruple symmetric inductor with $R=30\mu\text{m}$ and $W=6\mu\text{m}$ (a) $\text{Mag}(S_{11})$ (b) $\text{Phase}(S_{11})$ (c) $\text{Mag}(S_{21})$ (d) $\text{Phase}(S_{21})$	78
Fig. 4.27	Comparison of high frequency impedances and Q between measurement and simulation by enhanced T-model for quadruple symmetric inductor, $R=30\mu\text{m}$, $W=6\mu\text{m}$ (a) $L=\text{Im}(Z_{in})/\omega$ (b) $\text{Re}(Z_{in})$ (c) $\text{Re}(-1/Y_{21})$ (d) Q.....	78
Fig. 4.28	Comparison of S_{11} and S_{21} between measurement and simulation by	

	enhanced T-model for quadruple semi-symmetric inductor with $R=10$ and $W=6\mu\text{m}$ (a) $\text{Mag}(S_{11})$ (b) $\text{Phase}(S_{11})$ (c) $\text{Mag}(S_{21})$ (d) $\text{Phase}(S_{21})$	79
Fig. 4.29	Comparison of high frequency impedances and Q between measurement and simulation by enhanced T-model for quadruple semi-symmetric inductor, $R=10$, $W=6\mu\text{m}$ (a) $L = \text{Im}(Z_{in})/\omega$ (b) $\text{Re}(Z_{in})$ (c) $\text{Re}(-1/Y_{21})$ (d) Q.....	79
Fig. 4.30	Comparison of S_{11} and S_{21} between measurement and simulation by enhanced T-model for quadruple semi-symmetric inductor with $R=20$ and $W=6\mu\text{m}$ (a) $\text{Mag}(S_{11})$ (b) $\text{Phase}(S_{11})$ (c) $\text{Mag}(S_{21})$ (d) $\text{Phase}(S_{21})$	80
Fig. 4.31	Comparison of high frequency impedances and Q between measurement and simulation by enhanced T-model for quadruple semi-symmetric inductor, $R=20$, $W=6\mu\text{m}$ (a) $L = \text{Im}(Z_{in})/\omega$ (b) $\text{Re}(Z_{in})$ (c) $\text{Re}(-1/Y_{21})$ (d) Q.....	80
Fig. 4.32	Comparison of S_{11} and S_{21} between measurement and simulation by enhanced T-model for quadruple semi-symmetric inductor with $R=30$ and $W=6\mu\text{m}$ (a) $\text{Mag}(S_{11})$ (b) $\text{Phase}(S_{11})$ (c) $\text{Mag}(S_{21})$ (d) $\text{Phase}(S_{21})$	81
Fig. 4.33	Comparison of high frequency impedances and Q between measurement and simulation by enhanced T-model for quadruple semi-symmetric inductor, $R=30$, $W=6\mu\text{m}$ (a) $L = \text{Im}(Z_{in})/\omega$ (b) $\text{Re}(Z_{in})$ (c) $\text{Re}(-1/Y_{21})$ (d) Q..	81
Fig. 4.34	Enhanced T-model parameters for quadruple symmetric inductors. Spiral coil RLC network parameters versus radius (a) L_s (b) R_s (c) C_p and C_{ox} (d) R_p	83
Fig. 4.35	Enhanced T-model parameters for quadruple symmetric inductors. Skin effect and proximity effect parameters versus radius (a) L_{sk} (b) R_{sk} (c) L_{ddy} (d) R_{ddy} , in spiral coil network.....	83
Fig. 4.36	Enhanced T-model parameters for quadruple symmetric inductors. Substrate RLC network parameters versus radius (a) C_{sub} (b) $1/R_{sub}$ (c) L_{sub} (d) R_{loss}	84
Fig. 4.37	Enhanced T-model parameters for quadruple semi-symmetric inductors. Spiral coil RLC network parameters versus radius (a) L_s (b) R_s (c) C_p and C_{ox} (d) R_p	84
Fig. 4.38	Enhanced T-model parameters for quadruple semi-symmetric inductors. Skin effect and proximity effect parameters versus radius (a) L_{sk} (b) R_{sk} (c) L_{ddy} (d) R_{ddy} , in spiral coil network.....	85
Fig. 4.39	Enhanced T-model parameters for quadruple semi-symmetric inductors. Substrate RLC network parameters versus radius (a) C_{sub} (b) $1/R_{sub}$ (c) L_{sub} (d) R_{loss} .	85

Table Captions

Chapter 4

Table 4.1	Equivalent circuit model parameters effect on inductor performance Q_{\max} , f_{\max} and f_{SR} – single- π model as an example.....	55
Table 4.2	Enhanced T-model parameters for quadruple symmetric and quadruple semi-symmetric inductors with $W=6\mu\text{m}$ and $R= 10, 20, 30 \mu\text{m}$	74



Chapter 1

Introduction

1.1 Research Motivation

Wireless communication is one of the fastest growing domain in modern microelectronic industry. The strong demand for mobile communications and wireless data or voice transmission becomes a key driving force for high frequency IC technology development and creates a new market for global semiconductor manufacturing. The rapid growth of wireless communication market has fueled a tremendous competition in lower cost and enhanced functionalities. Traditionally, radio systems were implemented on the board level incorporating a lot of discrete components. Compared with discrete and hybrid designs, the monolithic approach offers the advantages of low cost, improved reliability and reproducibility, small size and weight, broadband performance, and circuit design flexibility.

Inductors acting as a key element in microwave and radio frequency (RF) integrated circuits and system draw an increasing focus and effort in recent research, due to the impact on monolithic chip area and overall cost. Although off-chip bonding wires generally adopted in conventional board design other than on-chip inductors can provide relatively higher Q, they sometimes suffer from larger variations in inductance value originated from mechanical process as compared with Si process for ICs. Note that tight variation control in Si IC process has been successful due to the steady advancement of photolithographic technology. Unfortunately, the process for integrating RF passive devices on a single chip requires a challenging endeavor, as compared with integration of active devices for wireless communication ICs.

Two more challenges associated with on-Si-chip inductors must be solved. One is the problem with on-chip inductor model in accuracy and scalability. Another one is the degraded quality factor (Q) and self-resonant frequency (f_{SR}), due to the worse substrate loss in Si as compared with GaAs technology, particularly at very high frequency. Regarding the database of monolithic inductors required for RF or MS (mixed signal) circuit simulation and design, a look-up table built based on test key generally invokes a time consuming process and restricts itself to few device dimensions or structures available in the test key, i.e. lacking scalability. Full wave EM simulation emerges as a popular approach in recent years, but the extensive computation time and memory makes it not suitable for circuit simulation and design, which generally require a fast turn-around cycle. One more problem with EM simulation is that an extensive calibration cannot be avoided to ensure the accuracy over a wide range of frequencies and various substrate resistivities.

To overcome the drawbacks apparent in mentioned approaches such as look-up table and EM simulation, an equivalent circuit model was developed in this thesis aimed at broadband accuracy, scalability, and computation efficiency. Besides, symmetric inductors aimed at applications in differential circuits widely used in RF ICs were designed and fabricated in 0.13 μ m RF CMOS process. Most importantly, new layouts were employed in the symmetric inductors for achieving ultra high f_{SR} beyond 70GHz and sufficient quality factor at $Q \geq 10$.

1.2 Thesis Overview

Chapter 2 provides an overview on the basic concept and fundamental theory for monolithic inductors. Monolithic inductors with various structures and features will be introduced. The mechanisms responsible for energy loss and Q degradation in monolithic inductors were investigated and discussed. Input impedance (Z_{in}), Quality factor (Q), and

self-resonance frequency of a monolithic inductor corresponding to single-ended and differential excitations will be seriously verified and discussed.

Chapter 3 introduces EM theory and simulation for broadband inductor design. The analytical model equations for calculating effective resistances and power losses due to skin effect and proximity effect have been derived. Furthermore, substrate losses which may dominate proximity effect at very high frequency was discussed and demonstrated with comparison between the conventional symmetric inductors and the broadband symmetric inductor of new design in this work. EM simulation was employed to explore and verify the mechanisms.

In Chapter 4, we propose a new inductor design with features of broadband up to 70 GHz and sufficiently high Q. Then, a broadband and scalable model was developed for the new inductors in this design, named as quadruple symmetric and semi-symmetric inductors. A parameter extraction flow has been established through an equivalent circuit analysis to enable an automatic parameter extraction and optimization.

Chapter 5 addresses the future work motivated by current achievements and worthy of continuous research effort in layout, experimental, measurement, and equivalent circuit (lumped element) model for facilitating RF circuit simulation and design.

Chapter 2

Inductor Theory and Inductor Measurement Technique

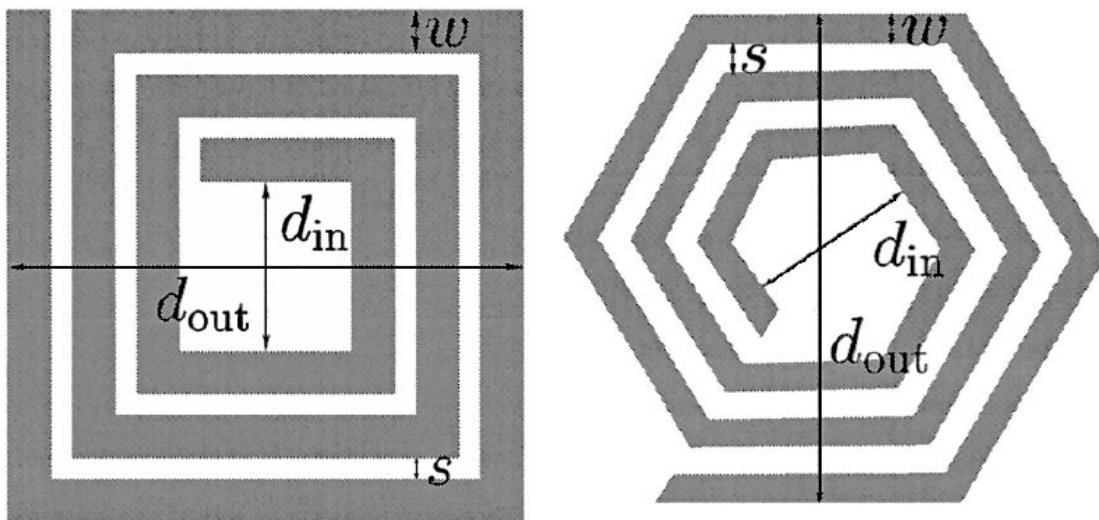
Monolithic inductor is an important component in radio frequency integrated circuits for communication systems such as satellite communication, personal communication services, wireless local area networks, and global positioning system. The rapid growth of the wireless communication market has driven a large demand for low cost and portable products. Traditionally, radio systems are implemented on the board level making use a lot of discrete components. As for a new approach such as monolithic ICs, all the passive components are fabricated on a single chip and then the external components can be minimized. In the monolithic ICs, on-chip inductors generally act as narrow-band loads in RF circuits such as amplifiers, oscillators, mixer, and impedance-matching circuits. The on-chip inductors can offer lower cost, smaller size and weight, improved reliability, broadband performance, and enhanced circuits flexibility.

However, a well known and critical problem with on-chip inductors is the lower Q-factor arising from conductor loss in the metal coils, substrate loss in semi-conducting silicon substrate, and degraded self-resonance frequency f_{SR} due to substrate parasitic capacitances. Several approaches have been used to improve the Q-factor and f_{SR} of monolithic inductors in silicon. One major category of the approaches are focused on reducing conductor loss, such as thicker metal, stacked metals, or lower resistivity metals. Another one segment cover substrate engineering and shielding method, such as high-resistivity substrate ($\rho > 1k\Omega \cdot \text{cm}$) or patterned ground shielding in low-resistivity substrates ($\rho < 10 \Omega \cdot \text{cm}$) for suppressing substrate losses. Note that patterned ground shielding sometimes leads to the penalty of degraded f_{SR} . Regarding chip area reduction, multilayer inductors with stacked spiral coils attract certain interest. However, both

Q-factor and f_{SR} are unfavorably affected by increased overlap and parasitic capacitances due to elevated coupling from the lower metals to the semi-conducting substrate in the multilevel stack structures.

2.1 Inductor Geometries and Structures

There are many ways to lay out an on-chip inductor, such as rectangle, hexagonal, octagonal and circular shown in figure 2.1 separately [8]. Square spiral inductors are popular because of the simple layout and easy implementation in mask. However, polygonal other than square spiral inductors become increasingly popular in practice of circuit design, due to the improved Q and smaller area for a specified inductance. The optimum structure is a circular spiral as shown in figure 2.1(d). The circular spiral can make a specified inductance in the smallest area, reducing the series resistance of metal line and parasitic capacitance and increasing the storage of magnetic energy of the spiral inductor. However, one major drawback of the circular structure is its layout complexity. In general, CADENCE virtuso is employed to assist the inductor layout



(a)

(b)

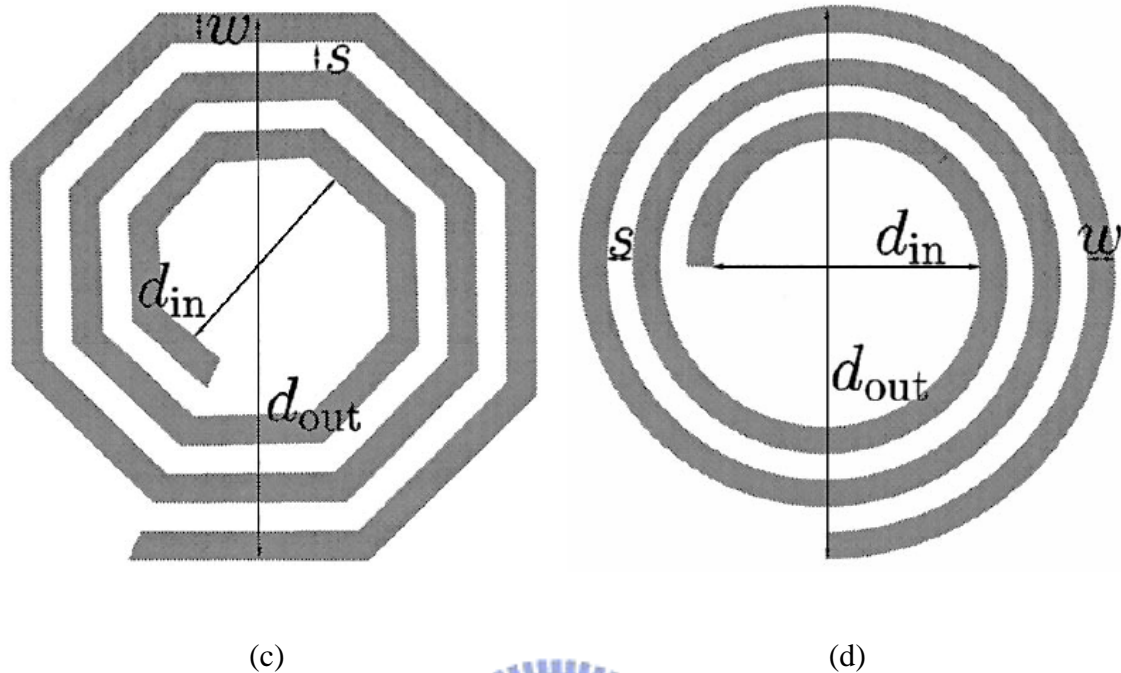


Figure 2.1 Spiral inductor structure. (a)rectangle, (b)hexagonal, (c)octagonal, (d)circular

In addition to the spiral inductors for single-end operation, there are other structures, such as conventional symmetric and fully symmetric inductors for differential operations, as shown in Fig.2.2(a) and (b). Multi-layer stack inductors in Fig.2.2(c) mentioned previously can be adopted for saving chip area, particularly useful for large inductances. The conventional symmetric inductor in Fig.2.2(a) is generally used in differential circuit topologies for increasing Q attributed to reduced substrate loss and more storage of magnetic energy. Viewing the layout of conventional symmetric inductors in Fig 2.2(a), a number of cross-over and cross-under connections are used to join groups of coupled metal traces from one side of an axis of symmetry to the other. Unfortunately, this connection results in undesired mismatch between two ports. The differential signals applied at port-1 and port-2 would no longer be 180° out of phase after they flew through the intersection since they passed different paths and materials. For some applications, circuit designer has to use differential inductor with center-tap. However, the center-tap of

a conventional differential inductor that we defined is not real center. We cannot determine where the exact center is. To overcome the addressed problems, a fully symmetrical inductor is proposed as shown in Fig.2.2(b) in which port-1 and port-2 are ensured identical in layout so that S_{11} should be exactly the same as S_{22} in magnitude and phase. As a result, the fully symmetrical inductors can realize significant improvement in symmetrical characteristics as compared to conventional symmetrical inductors.

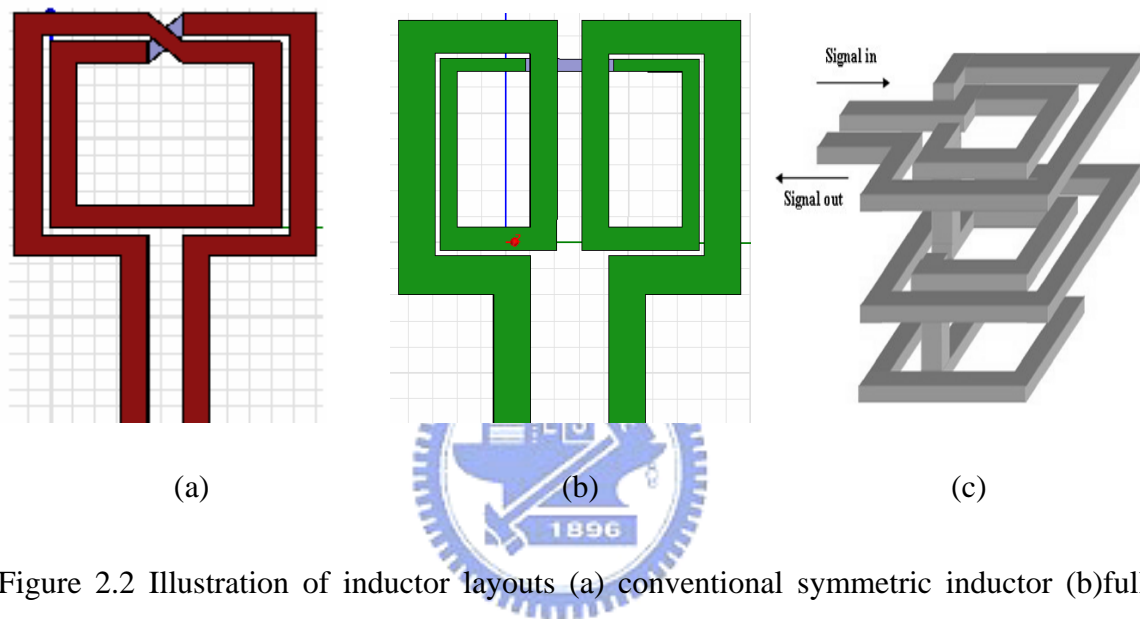


Figure 2.2 Illustration of inductor layouts (a) conventional symmetric inductor (b) fully symmetric inductor (c) multi-layer stack inductor

2.2 Losses in Inductor

There are several sources of loss in a monolithic inductor. One of the well known loss mechanisms is the series resistance in winding metals. The DC resistance of monolithic inductor is calculated as the product of the sheet resistance and the square number determined by the ratio of total length over width in the winding metals. However, at higher frequency the resistance of metal strips increases due to skin effect and proximity effect. Moreover, substrate losses increase with frequency due to the dissipative current that flow in the silicon substrate. In fact, there are two different mechanisms that cause the induction of these currents. One is the capacitive coupling between the metal strips of

inductors and the substrate underneath, which introduces displacement currents and energy loss, namely electric substrate loss. The other is the magnetic coupling caused by the time varying magnetic field linked to the strip, which induces eddy currents and energy loss, namely magnetic substrate losses.

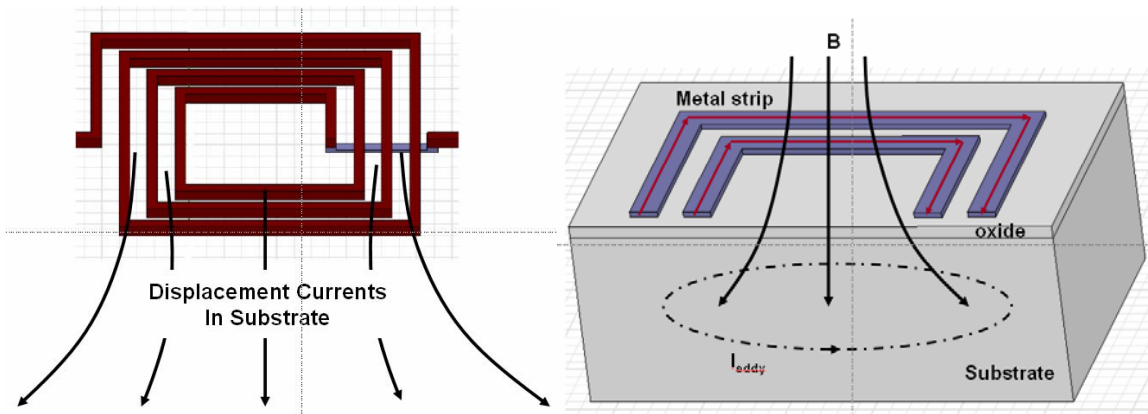


Figure 2.3 The electric and magnetic substrate losses in an on-chip inductor.

Figure 2.3 shows the electric and magnetic substrate losses of monolithic inductors. The magnetic field \vec{B} extends around the windings and into the substrate. The mechanism can be understood from Faraday's Law, which states that a time-varying magnetic field will induce an electric field in the substrate, and the induced electric field will force an image eddy current on the substrate with a direction opposite to that of current in the winding metals directly above the substrate.

2.3 Definition of Quality Factor

Inductors allow the storage of magnetic energy. It can be easily derived that the energy stored in an inductor is given by,

$$E_L = \frac{1}{2} L i_L^2 \quad (2.1)$$

where L is the inductance and i_L is the instantaneous current through the inductor.

From equation (2.1), the peak magnetic energy stored in an inductor in sinusoidal

steady state is given by,

$$E_{\text{peak inductor}} = \frac{1}{2} L |I_L|^2 = \frac{|V_L|^2}{2\omega^2 L} \quad (2.2)$$

where $|I_L|$ and $|V_L|$ correspond to the peak current through and the peak voltage across the inductor.

The quality factor Q of an inductor is a measure of the performance of the elements defined for a sinusoidal excitation and given by [2],

$$Q = 2\pi \cdot \frac{\text{energy stored}}{\text{energy loss per cycle}} = \omega \cdot \frac{\text{energy stored}}{\text{average power loss}} \quad (2.3)$$

The above definition is a general expression. In the case of an inductor, energy stored refers to the net peak magnetic energy.

To illustrate the determination of Q , consider an ideal inductor in series with a resistor in Fig. 2.4. This simple equivalent circuit model was composed of an inductor with resistance in the winding.

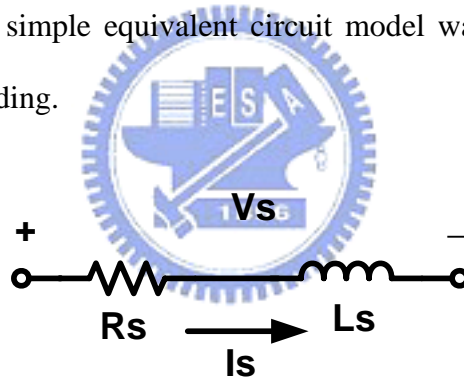


Figure 2.4 Inductor with a series resistance.

Since the current in both elements is equal, we use the equation for the peak magnetic energy in terms of current given in equation (2.4) as follows,

$$\begin{aligned} Q &= 2\pi \cdot \frac{\text{peak magnetic energy stored}}{\text{energy loss per cycle}} \\ &= 2\pi \cdot \frac{\frac{1}{2} L_s |I_s|^2}{\frac{1}{2} R_s |I_s|^2 \cdot \tau} = \frac{\omega L_s}{R_s} \end{aligned} \quad (2.4)$$

τ : the period of sinusoidal excitation

Note that the quality factor of an inductor with a lossy winding increases with

frequency provided that the series resistance R_s is a constant independent of frequency. In case that the resistance in series with the inductor can be reduced, it can help increase the quality factor Q of the inductor. Under an ideal condition that R_s can be eliminated, Q will become infinite since there is no loss. Using the above procedure, the quality factor of a lossy inductor in another equivalent circuit can be determined. We repeat the detail in the following.

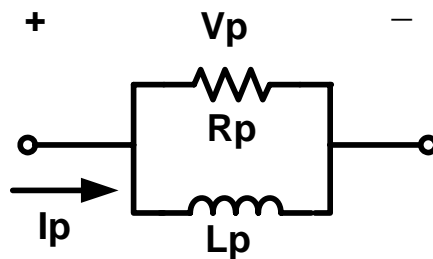


Figure 2.5 Inductor with a parallel resistance.

Since the voltage in both elements is equal, we use the equation for the peak magnetic energy in terms of voltage given in equation (2.2) to derive Q as follows,

$$\begin{aligned}
 Q &= 2\pi \cdot \frac{\text{peak magnetic energy stored}}{\text{energy loss per cycle}} \\
 &= 2\pi \cdot \frac{\frac{|V_p|^2}{2\omega^2 L_p}}{\frac{|V_p|^2}{2R_p} \cdot \tau} = \frac{R_p}{\omega L_p} \quad (2.5)
 \end{aligned}$$

τ : the period of sinusoidal excitation

The definition of quality factor is generally in the sense that it does not specify what stores or dissipates the energy. The subtle distinction between an inductor and an LC tank for the quality factor Q lies in the intended form of energy storage. For example, only the magnetic energy is of interest and any electric energy due to inevitable parasitic capacitances in a real inductor is counterproductive. Therefore, the Q of an inductor is proportional to the net magnetic energy stored and is given by,

$$\begin{aligned}
Q_{inductor} &= 2\pi \cdot \frac{\text{net magnetic energy stored}}{\text{energy loss per cycle}} \\
&= 2\pi \cdot \frac{\text{peak magnetic energy stored} - \text{peak electric energy}}{\text{energy loss per cycle}}
\end{aligned}
\tag{2.6}$$

An inductor is said to be at a state of self-resonance when the peak magnetic energy and peak electric energy are equal. According to (2.6), Q of an inductor vanishes to zero at the self-resonance frequency. At frequency above self-resonance frequency, no net magnetic energy is available from an inductor to any external circuit. In contrast, for an LC tank, the Q is defined at the resonant frequency ω_0 , and the term of stored energy in the expression for Q given by equation (2.3) is the sum of the average magnetic and electric energy. Since at resonance the average magnetic and electric energies are equal, so we have,

$$\begin{aligned}
Q_{tank} &= 2\pi \cdot \frac{\text{average magnetic energy} + \text{average electric energy}}{\text{energy loss per cycle}} \Big|_{\omega=\omega_0} \\
&= 2\pi \cdot \frac{\text{peak magnetic energy}}{\text{energy loss per cycle}} \Big|_{\omega=\omega_0} = 2\pi \cdot \frac{\text{peak electric energy}}{\text{energy loss per cycle}} \Big|_{\omega=\omega_0}
\end{aligned}
\tag{2.7}$$

The average magnetic or electric energy at resonance for sinusoidal excitation is $\frac{1}{4}L|I_L|^2 = \frac{1}{4}C|V_C|^2$ which are half the peak magnetic energy given by equation (2.2) Lets look at parallel RLC circuit in Fig. 2.6 to clarify the difference in defined Q between an inductor and an LC tank.

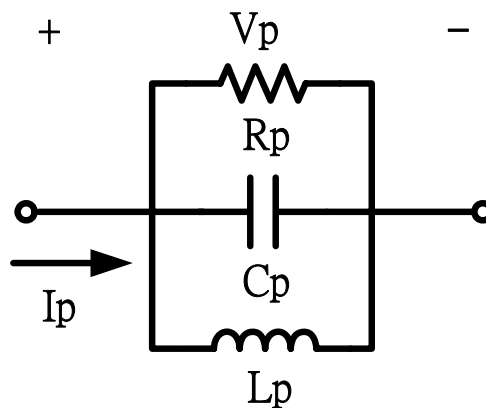


Figure 2.6 Parallel RLC circuit.

The quality of the inductor is calculated as follows,

$$\begin{aligned}
 Q_{inductor} &= 2\pi \cdot \frac{\text{peak magnetic energy stored} - \text{peak electric energy}}{\text{energy loss per cycle}} \\
 &= 2\pi \cdot \frac{\frac{|V_p|^2}{2\omega^2 L_p} - \frac{1}{2} C_p |V_p|^2}{\frac{|V_p|^2}{2R_p} \cdot \tau} = \frac{1}{\omega L_p} - \omega C_p \\
 &= \frac{R_p}{\omega L_p} \cdot \left[1 - \left(\frac{\omega}{\omega_0} \right)^2 \right]
 \end{aligned} \tag{2.8}$$

τ : the period of sinusoidal excitation

where the resonant frequency $\omega_0 = \frac{1}{\sqrt{L_p C_p}}$. Here $\frac{R_p}{\omega L_p}$ accounts for the magnetic energy stored in the inductor and ohmic loss of the parallel resistance in Fig. 2.4. The second term in equation (2.8) is the self-resonance factor describing the reduction in Q due to the increase in the peak electric energy with frequency and the vanishing of Q at the self-resonant frequency. In the parallel RLC circuit, $V_L = V_C = V_p$ which is depicted in the Fig. 2.5. Note that in each quarter cycle, when energy is being stored in the inductor, it is being released from the capacitor and vice versa. As the frequency ω increases, the magnitude of I_L decreases while that of I_C increases until they become equal at the resonant-frequency ω_0 , so that an equal amount of energy is being transferred back and forth between the inductor and capacitor. At this frequency, $Q_{inductor}$ given by equation (2.8) is zero. As ω increases above ω_0 , the magnitude of I_L becomes increasingly less than the magnitude of I_C , and the net magnetic energy stored becomes increasingly more negative. It explains previous comment that no net magnetic energy is available from an inductor to any external circuit at frequency above ω_0 . The inductor becomes capacitive in nature, and $Q_{inductor}$ given by equation (2.8) becomes negative at frequency beyond ω_0 . In the following, Q for a n LC tank will be derived based on the original definition in equation (2.7).

$$\begin{aligned}
Q_{\text{tank}} &= 2\pi \cdot \frac{\text{peak magnetic energy}}{\text{energy loss per cycle}} \Big|_{\omega=\omega_0} \\
&= 2\pi \cdot \frac{\frac{|V_p|^2}{2\omega^2 L_p}}{\frac{|V_p|^2}{2R_p} \cdot \tau} \Big|_{\omega=\frac{1}{\sqrt{L_p C_p}}} = \frac{R_p}{\sqrt{L_p / C_p}} \quad (2.9)
\end{aligned}$$

τ : the period of sinusoidal excitation

Note that the tank Q is not zero at resonance $\omega = \omega_0$, which is absolutely different from what happened in inductor with zero Q at resonance. Also, note that the same result can be derived using the ratio of the resonant-frequency to -3 dB bandwidth as follows,

$$\begin{aligned}
Q_{\text{tank}} &= 2\pi \cdot \frac{f}{BW_{-3dB}} \Big|_{f=f_0} \\
&= 2\pi \cdot \frac{f}{\frac{1}{2\pi R_p C_p}} \Big|_{f=\frac{1}{2\pi\sqrt{L_p C_p}}} = \frac{R_p}{\sqrt{L_p / C_p}} \quad (2.10)
\end{aligned}$$

Equation (2.9) and (2.10) are the same as we expect.

Both Q definitions discussed above are important, and their applications are determined by the intended function in a circuit. When evaluating the quality of on-chip inductors as a single element, the definition of inductor quality given by equation (2.6) is more appropriate. However, if the inductor is being used in an LC tank, the definition should be referred to equation (2.7).

Figure 2.7 illustrates a real inductor, which was represented by a parallel RLC circuit.

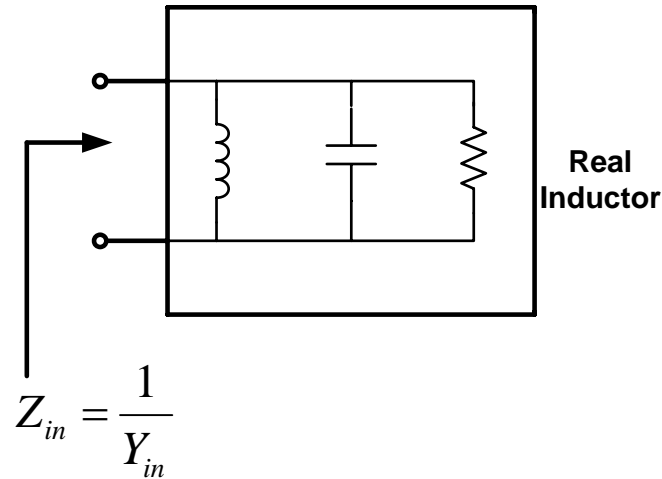


Figure 2.7 An alternative method for determining the Q in real inductors.

In contrast with equation (2.8), it can be easily determined that the real inductor quality factor of a parallel RLC circuit is given by the negative of the ratio of the imaginary part to the real part of the input admittance, namely the ratio of the imaginary part to the real part of the input impedance. The above definitions are expressed in equation (2.11) and are appropriate for determining the Q of inductors from simulation or measurement results.

$$Q_{inductor} = \frac{\text{Im}\{Z_{in}\}}{\text{Re}\{Z_{in}\}} = -\frac{\text{Im}\{Y_{in}\}}{\text{Re}\{Y_{in}\}} \quad (2.11)$$

2.4 Single-ended one-port excitation

A cross-sectional view of a monolithic spiral inductor on a lightly doped substrate is illustrated in Fig. 2.8, and the corresponding lumped element model is shown in Fig. 2.9 [5],[6].

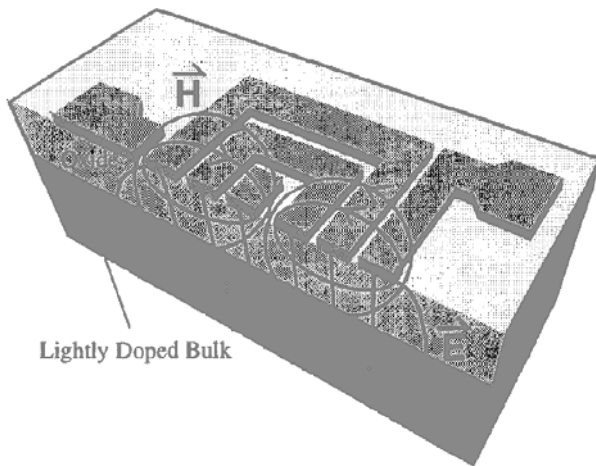


Figure 2.8 Cross-section of a spiral inductor

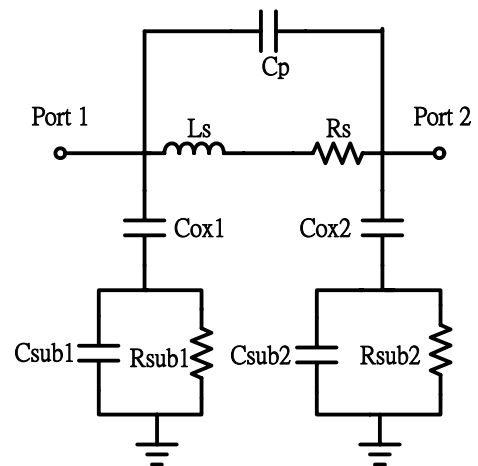


Figure 2.9 π -Model

Typically, the inductance of a monolithic inductor is determined by Y- or Z-parameters, which can be converted from measured or simulated S-parameters. Note that both inductance (L) and quality factor (Q) are extracted from Y or Z-parameters and differentiated in two operation modes, such as single-ended and differentially driven schemes. To understand the inductor characteristics under a single-ended excitation, a simple two-port equivalent circuit model, namely single- π model in Fig.2.10 is frequently used for performance parameter extraction and simulation.

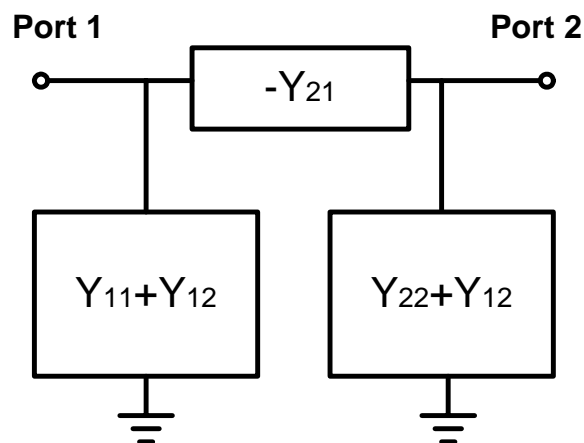


Figure 2.10 A single- π model as a simple two-port equivalent circuit for on-chip inductors

This equivalent circuit model is established as a single- π network, represented by two-port Y-parameters in Fig.10. To define L and Q, this single- π model must be reduced

to a single inductor element like the parallel RLC circuit shown in figure 2.7. As the frequency is below self-resonant frequency, this simple inductor element is inductive. Therefore, its input impedance can be expressed as $R + jX$.

Then, we have,

$$L = \frac{X}{2\pi f} \Big|_{\text{at low frequency}} \quad \text{and} \quad Q = \frac{X}{R} = \frac{\omega L}{R} \quad (2.12)$$

As shown in Fig. 2.11, if port-2 of the single- π network is grounded, the $Y_{22} + Y_{12}$ element in Fig. 2.10 is bypassed and the circuit looking into port-1 reduces to the admittance Y_{11} connected to ground due to the Y_{12} is eliminated by admittance in parallel

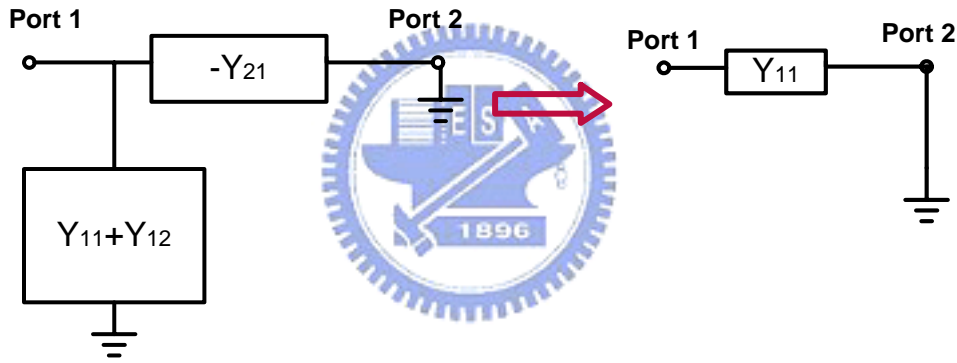


Figure 2.11 Y-parameter conversion for a single- π network with port-2 grounded.

Consequently, we have,

$$R + jX = \frac{1}{Y_{11}} = Z_{11} \quad \Rightarrow \quad L = \text{Im}\left(\frac{1}{Y_{11}}\right) = \text{Im}\left(\frac{Z_{11}}{2\pi f}\right) \Big|_{\text{low frequency}} \quad (2.13)$$

$$\text{and} \quad Q = \frac{\text{Im}\left(\frac{1}{Y_{11}}\right)}{\text{Re}\left(\frac{1}{Y_{11}}\right)} = \frac{\text{Im}(Z_{11})}{\text{Re}(Z_{11})} \quad (2.14)$$

Note that equation (2.14) is equivalent to eq.(2.11) derived previously.

Actually, this method is also equivalent to taking one-port S-parameter measurements

with one terminal of the inductor grounded or two-port S-parameter measurements with one port grounded. The later can be converted into one-port S-parameter buy using the formula in equatioin (2.15) [3].

$$S_{11(\text{one port})} = S_{11(\text{two port})} + \frac{S_{12}\Gamma_L S_{21}}{1 - S_{22}\Gamma_L} \quad (2.15)$$

When port-2 is grounded, namely $\Gamma_L = -1$, we have,

$$S_{11(\text{one port})} = S_{11(\text{two port})} - \frac{S_{12}S_{21}}{1 + S_{22}} \quad (2.16)$$

Then, for single-ended one-port excitation, the input impedance shown in Fig. 2.12 is calculated by equation (2.17) using the result of equation 2.16 [3].

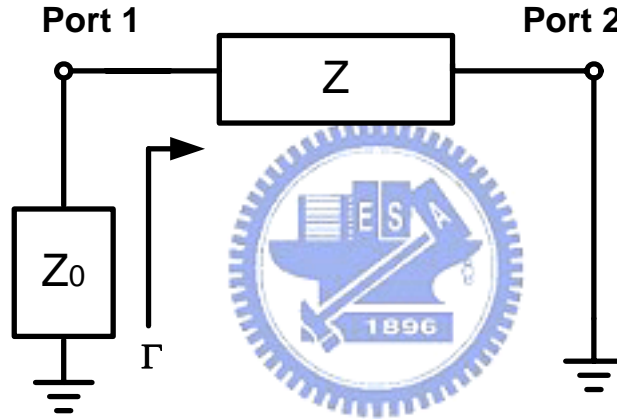


Figure 2.12 Two-port sing- π equivalent circuit with port-2 grounded.

$$R + jX = Z_{11(\text{one-port})} = Z_{in} = Z_0 \cdot \frac{1 + \Gamma}{1 - \Gamma} = Z_0 \cdot \frac{1 + S_{11(\text{one port})}}{1 - S_{11(\text{one port})}} \quad (2.17)$$

The quality factor Q under single-port excitation can be calculated by (2.18) using the derived input impedance in eq.(2.17)

$$Q = \frac{\text{Im}(Z_{in})}{\text{Re}(Z_{in})} = \frac{\text{Im}(Z_{11(\text{one-port})})}{\text{Re}(Z_{11(\text{one-port})})} \quad (2.18)$$

$$Z_{11(\text{one-port})} = Z_0 \frac{1 + S_{11(\text{one-port})}}{1 - S_{11(\text{one-port})}}$$

A single- π equivalent circuit model with single-ended excitation at port-1 and port-2 grounded is shown in Fig. 2.13 and Fig. 2.14.

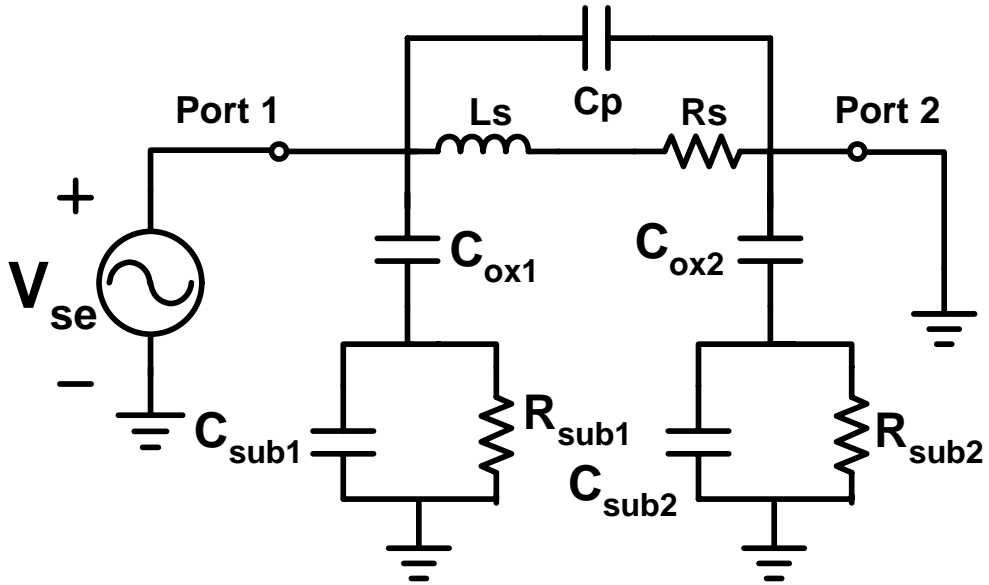


Figure 2.13 A single- π model for an on-chip inductor with a single-ended excitation.

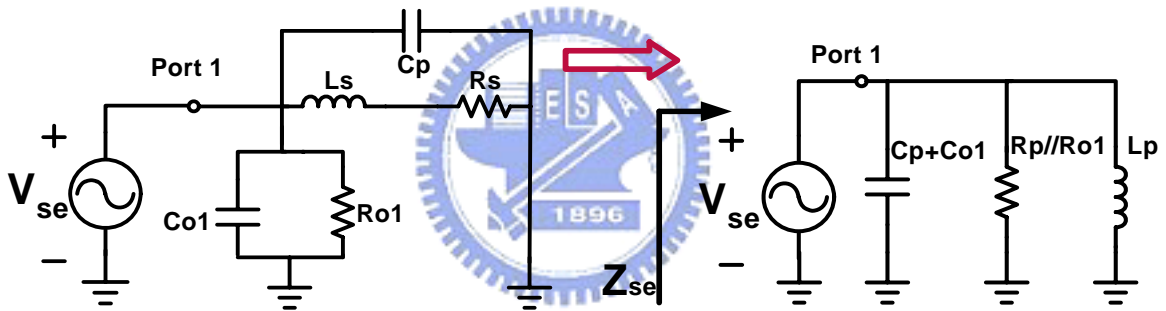


Figure 2.14 An equivalent circuit conversion for a single- π model under a single-ended excitation to a parallel RLC network where the original network consisting of C_{ox1} series with C_{sub1} shunt R_{sub1} in Fig.2.12 is replaced by C_{o1} shunt R_{o1} .

The single-ended one-port Q and self-resonant frequency can be calculated by way of Fig. 2.14, and shown in equations (2.19) ~ (2.21) [10].

$$Q_{se} = \frac{\frac{1}{\omega L_p} - \omega(C_p + C_{o1})}{\frac{1}{R_{o1}} + \frac{1}{R_p}} \quad (2.19)$$

$$= \frac{R_p R_{o1} \left[1 - \left(\frac{\omega}{\omega_r} \right)^2 \right]}{\omega L_p (R_p + R_{o1})} = \frac{\omega L_s}{R_s} \frac{R_{o1}}{R_{o1} + R_s} \frac{1}{\left[1 + \left(\frac{\omega L_s}{R_s} \right)^2 \right]} \left[1 - \left(\frac{\omega}{\omega_{se}} \right)^2 \right] \quad (2.20)$$

where ω_{se} is the self-resonance frequency under a single-ended excitation, given by

$$\omega_{se} = \frac{1}{\sqrt{L_p (C_p + C_{o1})}} = \frac{1}{\sqrt{L_s (C_p + C_{o1})}} \frac{1}{\sqrt{1 + \left(\frac{\omega L_s}{R_s} \right)^2}} \quad (2.21)$$

2.5 Single-ended two-port excitation [3]

For single-ended two-port excitation, the input impedance shown in Fig. 2.15 is given by equation (2.22) [3]. The single-ended two-port Q and self-resonant frequency can be calculated by the same way as before.

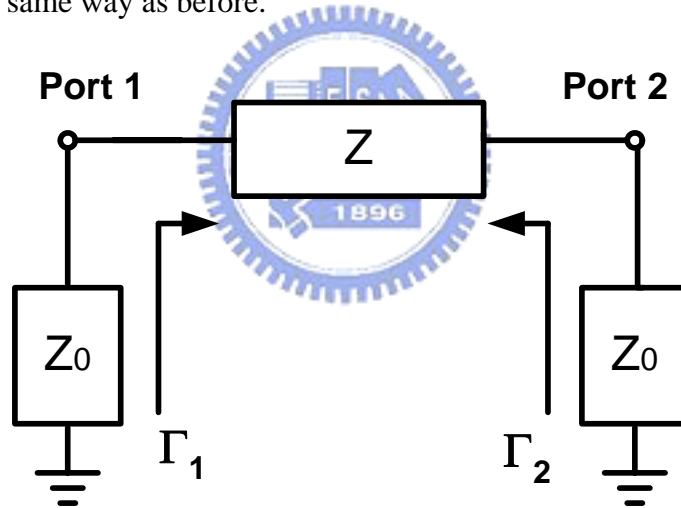


Figure 2.15 Two-port single- π equivalent circuit with both ports terminated with Z_0 .

$$Z_1 = Z + Z_0 = Z_0 \cdot \frac{1 + \Gamma_1}{1 - \Gamma_1} \Rightarrow Z = Z_0 \cdot \left[\left(\frac{1 + \Gamma_1}{1 - \Gamma_1} \right) - 1 \right] = Z_0 \cdot \frac{2\Gamma_1}{1 - \Gamma_1}$$

$$\therefore Z = Z_0 \cdot \frac{2\Gamma_i}{1 - \Gamma_i}, \quad i = 1, 2 \quad (2.22)$$

$$Z_{in} = Z_0 \cdot \frac{2\Gamma_i}{1 - \Gamma_i} = Z_0 \cdot \frac{2S_{ii(two\ port)}}{1 - S_{ii(two\ port)}}, \quad (i = 1, 2)$$

The quality factor Q under single-ended and two-port excitation can be calculated by (2.23) using the derived input impedance in eq.(2.22)

$$Q = \frac{\text{Im}(Z_{in})}{\text{Re}(Z_{in})} = \frac{\text{Im}\left(Z_0 \frac{2S_{ii}}{1-S_{ii}}\right)}{\text{Re}\left(Z_0 \frac{2S_{ii}}{1-S_{ii}}\right)}, \quad i = 1, 2 \quad (2.23)$$

2.6 Differential excitation [7],[11]

On the other hand, if the inductor will be used in a differential configuration, that is, neither port is at AC ground potential, a different approach is required. The one-port differential S-parameter (S_d) is defined in equation (2.24) [11].

$$S_d = \frac{S_{11} + S_{22} - S_{12} - S_{21}}{2} \quad (2.24)$$

For differential excitation, the input impedance is given by equation (2.25) by using the result of equation (2.24) [11].

$$Z_d = Z_{in} = Z_{11} + Z_{22} - Z_{12}Z_{21} = 2Z_0 \cdot \frac{1+S_d}{1-S_d} \quad (2.25)$$

To understand the differential excitation it's helpful to look at the lumped equivalent-circuit model in Fig. 2.16 and Fig. 2.17. For a differential excitation, the signal is applied between the two ports and the differential input impedance Z_d is the parallel combination of two substrate parasitic networks and winding network itself. At lower frequencies, the input impedance in either the single-ended or differential connections is approximately the same, but as the frequency increases, substrate parasitic C_o and R_o come into play.

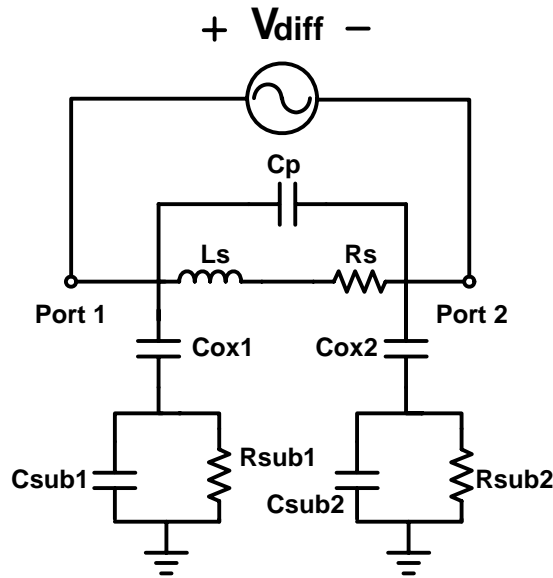


Figure 2.16 A lumped element π -model for a differential excitation.

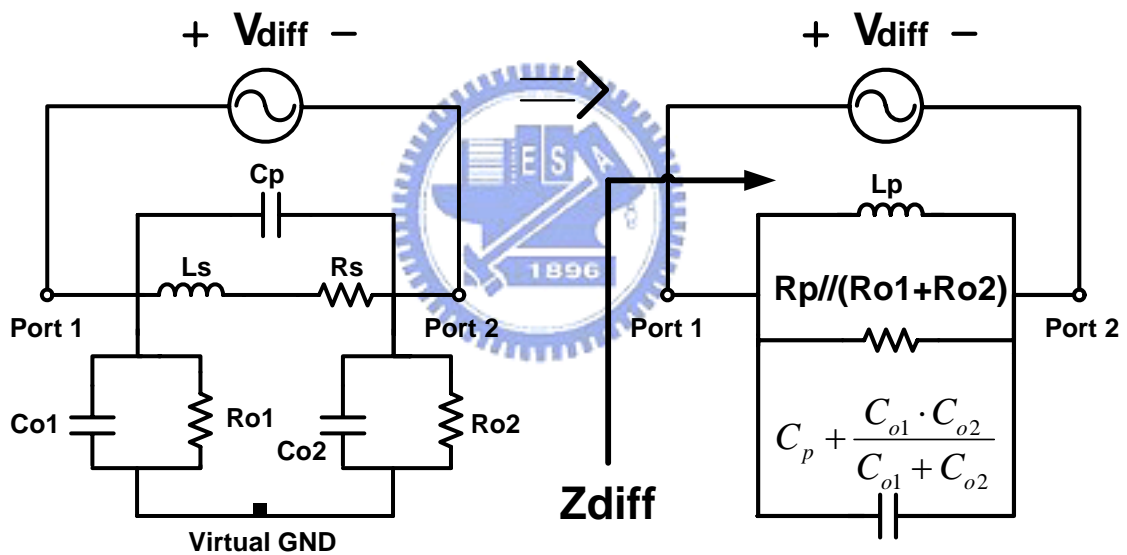


Figure 2.17 An equivalent circuit conversion for a lumped element π model under a differential excitation to a parallel RLC network

For differential excitation, these parasitics have a higher impedance at a given frequency than in the single-ended connection. This reduces the real part and increases the reactive component of the input impedance. Therefore, the inductor Q is improved when driven differentially, and the self-resonant frequency increases due to the reduction in the effective parasitic capacitance from $(C_p + C_{o1})$ to $[C_p + C_{o1}C_{o2}/(C_{o1} + C_{o2})]$.

The differential quality factor Q_d and self-resonant frequency ω_d can be derived based on circuit analysis in Fig. 2.17, and the results given in (2.26) ~ (2.28).

$$Q_d = \frac{\frac{1}{\omega L_p} - \omega \left(C_p + \frac{C_{o1} C_{o2}}{C_{o1} + C_{o2}} \right)}{\frac{1}{R_{o1} + R_{o2}} + \frac{1}{R_p}} \quad (2.26)$$

$$\begin{aligned} Q_d &= \frac{R_p}{\omega L_p} \frac{(R_{o1} + R_{o2})}{(R_p + R_{o1} + R_{o2})} \left[1 - \left(\frac{\omega}{\omega_d} \right)^2 \right] \\ &= \frac{\omega L_s}{R_s} \frac{(R_{o1} + R_{o2})}{(R_{o1} + R_{o2}) + R_s} \left[1 + \left(\frac{\omega L_s}{R_s} \right)^2 \right]^{-1} \left[1 - \left(\frac{\omega}{\omega_d} \right)^2 \right] \end{aligned} \quad (2.27)$$

$$Q_s = \frac{\omega L_s}{R_s} = Q_p = \frac{R_p}{\omega L_p}, \quad R_p = R_s(1 + Q_s^2), \quad L_p = L_s(1 + 1/Q_s^2)$$

$$\omega_d = \frac{1}{\sqrt{L_p \left\{ C_p + \left[\frac{C_{o1} C_{o2}}{C_{o1} + C_{o2}} \right] \right\}}} = \frac{1}{\sqrt{L_s \left(C_p + \frac{C_{o1} C_{o2}}{C_{o1} + C_{o2}} \right)}} \sqrt{1 + \left(\frac{R_s}{\omega L_s} \right)^2} \quad (2.28)$$

Chapter 3

EM Theory and Simulation for Broadband Inductor Design

Wireless communication emerges as one of the fastest growing area in modern microelectronic industry. The strong demand for mobile communications and wireless data or voice transmission becomes a key driving force for high frequency IC technology development and creates a new market for global semiconductor manufacturing. Moreover, it has fueled a drastic competition in production and marketing for lower cost, easy portability, and enhanced functionalities. To realize system on a single chip (SoC), some effort has been tried on different technologies like CMOS, SiGe HBT, or BiCMOS, or maybe a heterogeneous integration. The latter two, i.e. SiGe and BiCMOS may offer better performance in terms of active device speed, bandwidth or current drivability. Unfortunately, both SiGe and BiCMOS reveal the penalties of process complexity and higher cost, as compared to CMOS. Furthermore, the aggressive advancement of CMOS technology in recent years to nanoscale era escalates active device speed, such as f_T and f_{max} to above 100 GHz and makes itself the most competitive technology in aspects of cost, performance, and integration level, etc. Due to the mentioned advantages, RF CMOS technology is becoming the main stream of choice for manufacturing wireless communication. It explains the focus of our choice in this research for on-Si-chip inductors.

The most critical challenges encountered for high frequency circuits and products built on bulk Si CMOS technology are two folds, one is the degraded quality factor (Q) and self-resonant frequency (f_{SR}) in passive devices like inductors, due to worse substrate loss compared to GaAs, and another one is lack of an accurate model for RF CMOS circuit simulation in which substrate loss plays a key role, particularly at very high frequency.

Although off-chip bonding wires generally adopted in conventional board design can provide relatively higher Q as compared with on-chip inductors, they sometimes suffer much larger variations in inductance value originated from mechanical process. Regarding the problem of lacking an accurate inductor model for RF circuit simulation, one of alternative solutions is a table look-up method based on inductor test-key's data base. However, this kind of trial-and-error approach is time consuming and not suitable for advanced development in an aggressive time frame. What is worse, the table look-up method causes resource wasted and restricts RF designers in a limited database with little room for tuning and optimization. Another approach is by using EM simulators; however this kind of numerical simulation generally requires extensive computation time as well as memories and cannot fit circuit simulation, which always demands a fast turn-around cycle. One more drawback with EM simulation is the need of an extensive calibration over material and process parameters for ensuring accuracy. The sensitivity of 3D EM simulation to wave injection methods and guard-ring layout, particularly significant for very small inductors in broadband design is identified and introduces difficulty in this approach.

Based on the consideration, the equivalent circuit model was selected as the most appropriate approach to fit application in RF circuit simulation and design. The equivalent circuit model simply represent the inductor as a lumped element circuit and π -model is the most popular one due to its simplicity and easy implementation in circuit simulators. examples. A typical π -model includes series metal resistance and inductance, coupling capacitance between port-1 and port-2 and that between spiral metals and substrate underneath, and substrate effects. A physical model is proposed to capture the high-frequency behavior as shown in Fig. 3.1. Therefore, the spiral inductor was built on Si-substrate where the high-frequency behavior is complicated due to semi-conducting

substrate nature. The conventional π -model reveals limitation in broadband accuracy due to some neglected effects such as eddy current on metal and substrate. In order to overcome this disadvantage, 3D EM simulation was performed using HFSS to investigate the lossy substrate effect.

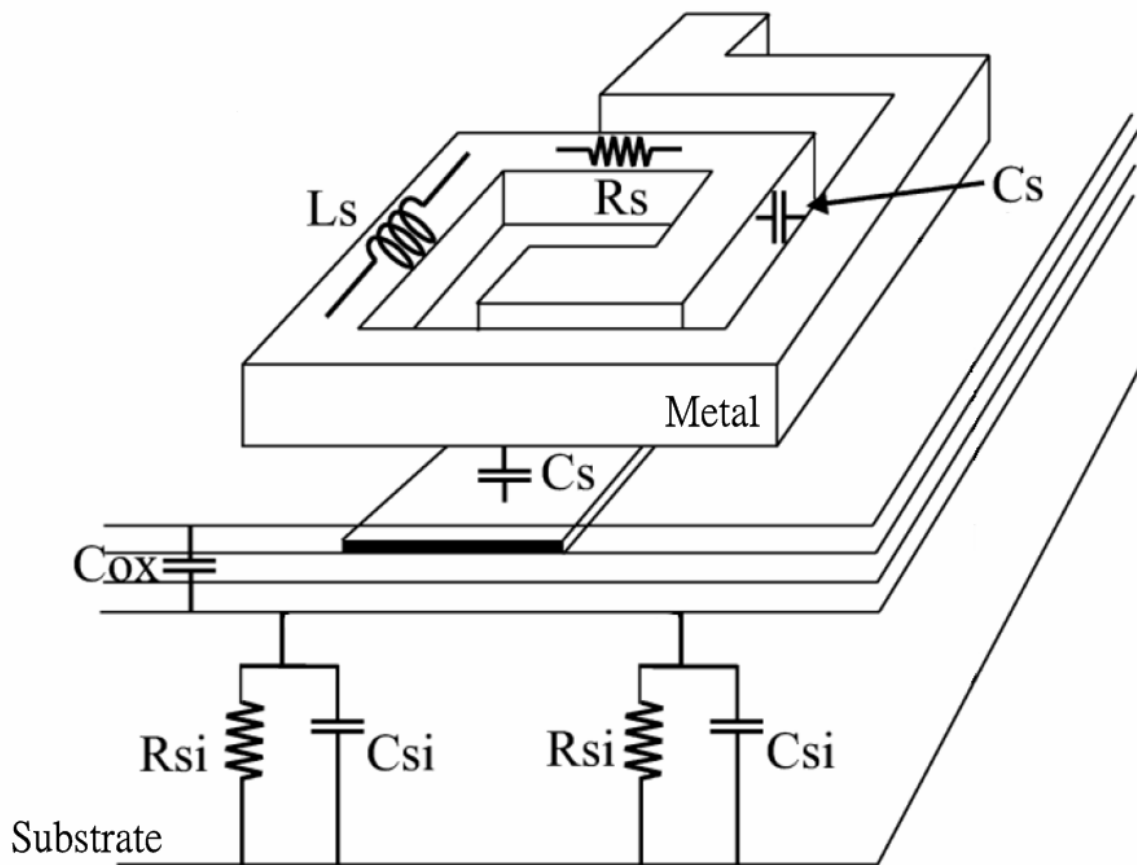


Figure 3.1 The device cross section and representative π -model for an inductor integrated on Si substrate.

3.1 EM Simulation tool and simulation method

In a conventional approach, the development of an equivalent model depends on model parameter extraction from measured data. Unfortunately, the availability of measured data is determined by the fabrication of test key, which generally requires a long

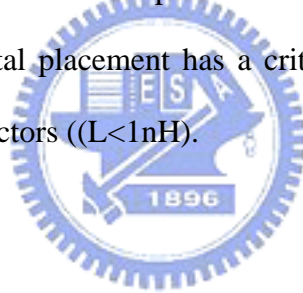
cycle time of around 3 months or more for advanced processes like 130nm or 90nm technologies. Besides, limited quota for test chip tape-out in advanced processes due to extremely high fabrication cost is another difficulty encountered for academic community compared to semiconductor industry. To overcome the mentioned restrictions and difficulties, EM simulation is recognized as a promising method in consideration of time, cost, flexibility in test structure design, and optimization. Besides, EM simulation can help verify the de-embedding methods, which are particularly critical for very small inductors.

Currently, there are many commercialized or proprietary EM simulation tools, which can calculate high frequency characteristics of RF components, transmission lines (TML), or package, etc. Sonnet, Microwave office, Ansoft HFSS, and Agilent ADS Momentum are popular and frequently used tools among the commercialized tools. ADS Momentum is a planar full-wave EM solver that can simulate electric and magnetic fields in the conductors, dielectric and substrate. This kind of 2.5D EM wave simulators can save computation time to a certain extent as compared with truly 3D simulators like HFSS. However, some critical problems, such as degraded accuracy and failure in convergence may happen in this kind of tools. To overcome the critical issues, particularly worse in very small inductors for our study, HFSS is of our choice in this research, even though an extensive computation time and memories are required. It is desirable to achieve high frequency parameters, such as S-parameters and derived Y- as well as Z-parameters with sufficient accuracy for inductors on Si substrate, over a broadband of frequencies. To ensure the accuracy over high frequencies, a number of key mechanisms, such as skin effect, proximity effect, and substrate coupling effect must be adequately implemented in the simulation tools. The ultimate goal is to predict S-parameters with guaranteed accuracy up to self-resonance frequency and beyond. Subsequently, the key performance parameters like quality factor Q , maximum Q (Q_{\max}), f_m corresponding to Q_{\max} , and self-resonance

frequency (f_{SR}) can be predicted before chip fabrication. In this way, the EM simulation results can serve as measured data for model parameter extraction and optimization aimed for an equivalent circuit model build-up.

3.2 HFSS for 3D EM simulation

As mentioned previously, an extensive calibration is indispensable for general EM simulators to attaining required accuracy. The calibration should cover parameters related to material, process, layout, topology, and substrate. Unfortunately, the calibration done on HFSS and ADS momentum in previous work is limited to inductors with sufficiently large size ($L > 1nH$) but reveals increasing deviation in very small inductors for broadband design targeting frequency up to 70 GHz in this topic. Through a careful study, it is identified that simulation environment setup in terms of RF signal injection direction and guard ring (GR) layout or metal placement has a critical effect on simulation accuracy, particularly for very small inductors ($L < 1nH$).



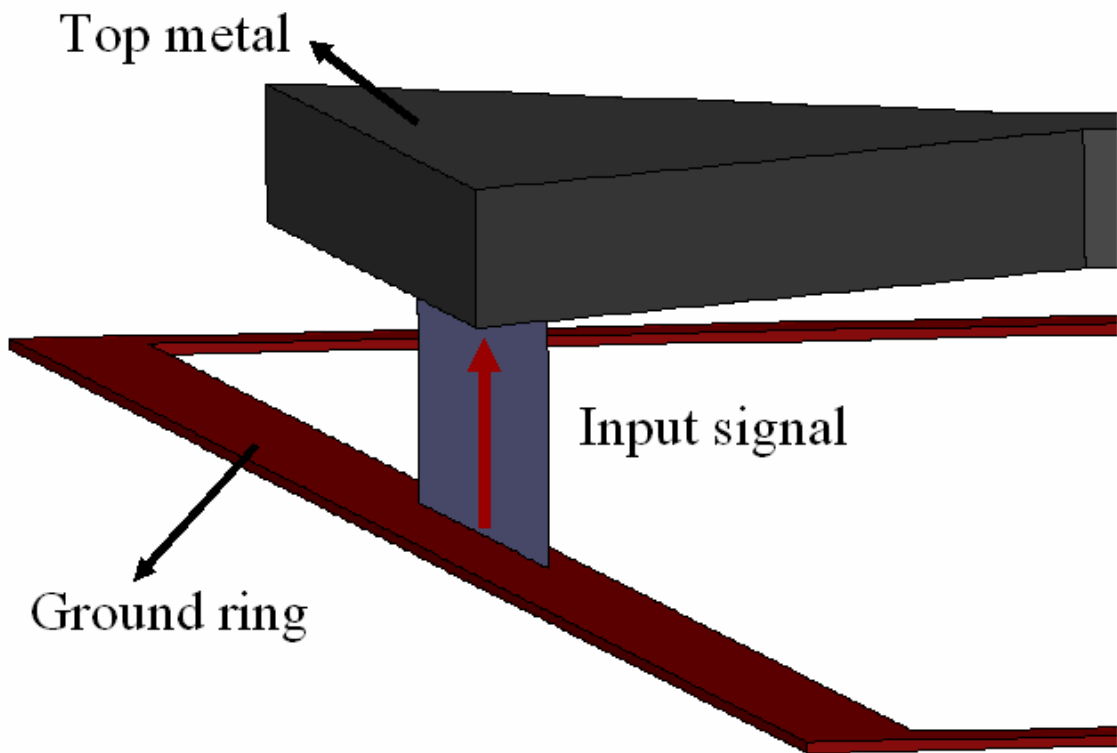


Figure 3.2 Vertical mode with RF signal injection at top metal (M8) and grounded ring (GR) at M1.



Fig. 3.2 illustrates the simulation environment setup, which was suggested in HFSS user manual and commonly used in on-chip inductor simulation. The RF signal was applied in a vertical way through the vias, then reaching top metal (M8) and the guard ring (GR) was placed in the bottom metal (M1). This kind of setup can enable acceptable accuracy over higher frequencies but over-estimates the real part of input impedance $\text{Re}(Z_{in})$ for miniaturized inductor ($L < 1\text{nH}$) in lower frequencies.

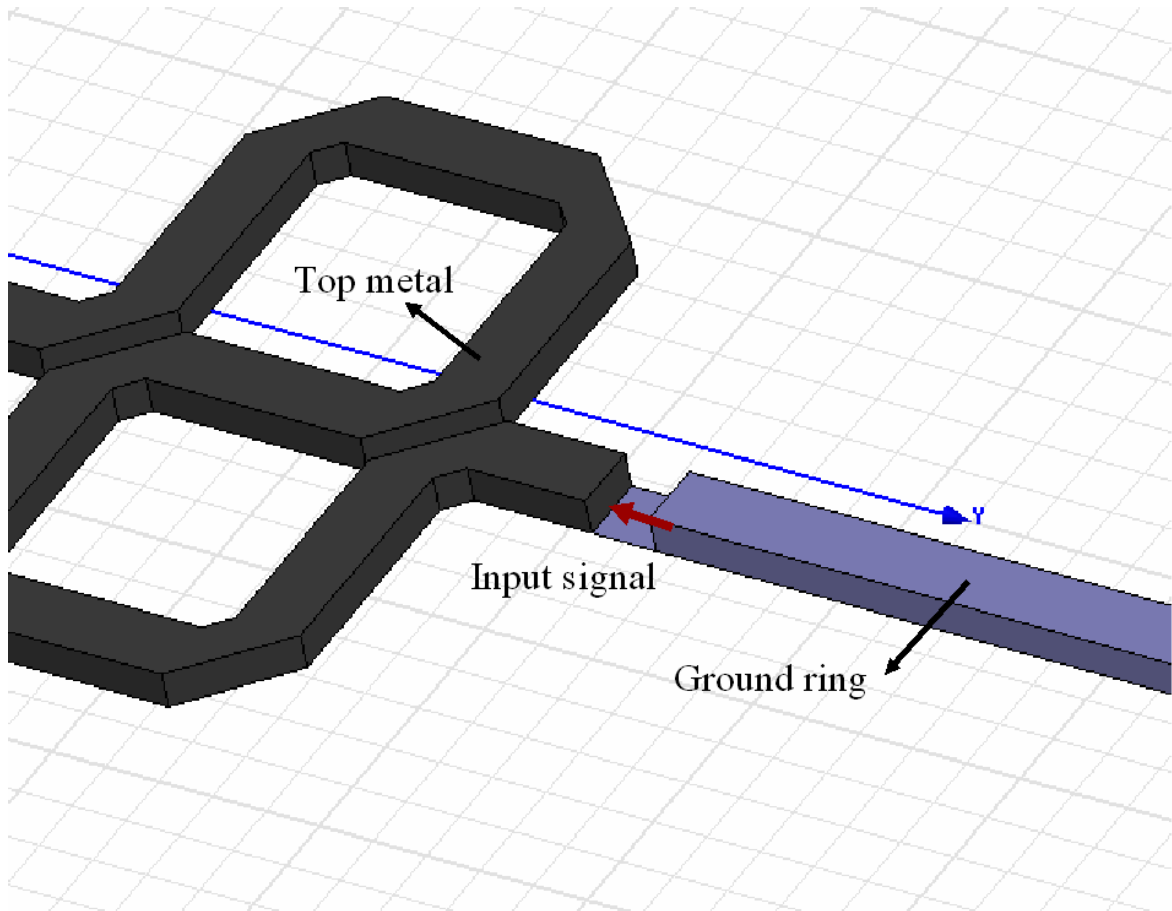


Figure 3.3 Horizontal mode with RF signal injection and grounded ring (GR), both at top metal (M8).

Trying to solve the mentioned problem identified from vertical mode setup in Fig. 3.2, a different one namely horizontal mode with RF signal injection in a horizontal way through the top metal (M8) and GR at the same plane, i.e. M8 was proposed as shown in Fig. 3.3. In this setup, RF signal injection approaches the real condition but the GR at M8 is inconsistent with the practice in real layout. The inconsistency introduced in 3D EM simulation causes a dramatic deviation from measured data in terms of $L = \text{Im}(Z_{in})/\omega$, $\text{Re}(Z_{in})$, $R_s = \text{Re}(-1/Y_{21})$, and $Q = \text{Im}(Z_{in})/\text{Re}(Z_{in})$, as shown in Fig. 3.5. This horizontal setup with GR at M1 under-estimates $\text{Re}(Z_{in})$ and over-estimates Q .

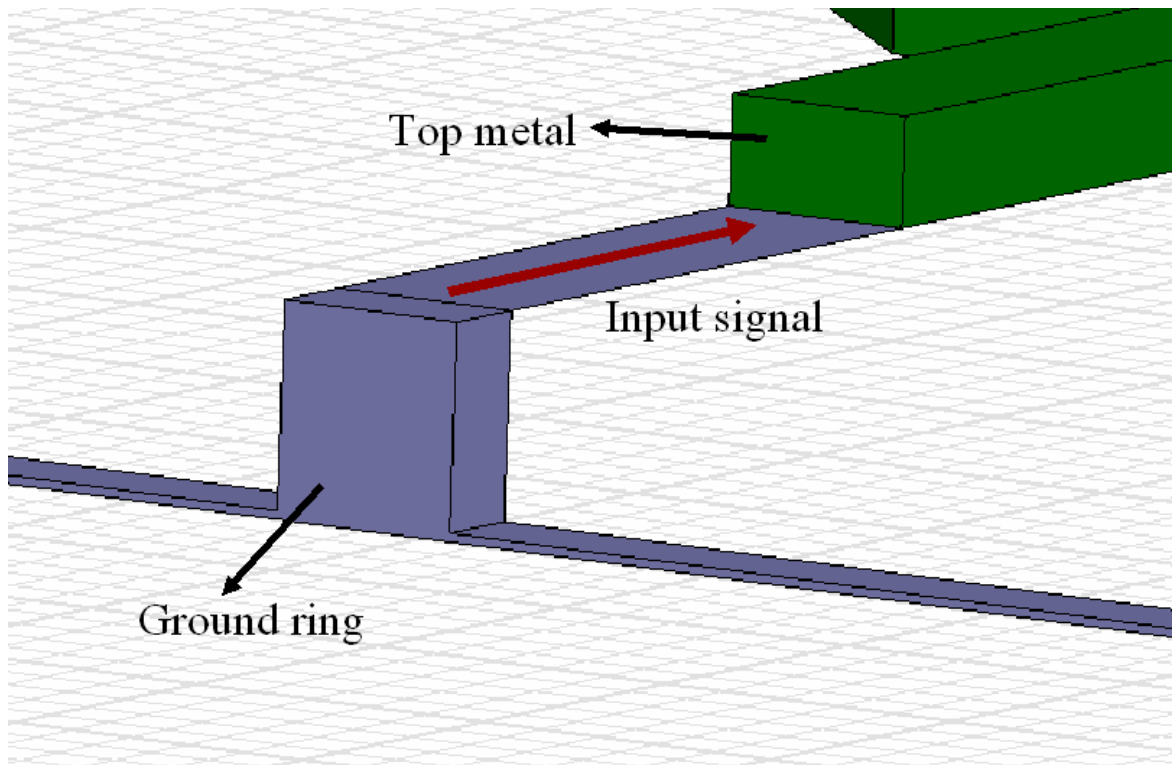


Figure 3.4 Horizontal mode with RF signal injection at top metal (M8) and ground ring (GR) at M1.

To overcome the deviation revealed by the first version of horizontal mode in Fig. 3.3, a modification was done in terms of 3D topology for RF signal injection and GR placement to fit miniaturized inductors. Fig. 3.4 presented an improved horizontal mode built up following the actual layout in which the ground ring (GR) is implemented with the ground metal (M1) and RF signal is injected through the top metal (M8). As shown in Fig. 3.5, this improved horizontal mode with GR at M1 can fix the deviation suffered by the previous one with GR at M8 and achieve a much better match with measurement in the specified key parameters (L , $\text{Re}(Z_{in})$, R_s , and Q) over ultra high frequency to 110 GHz.

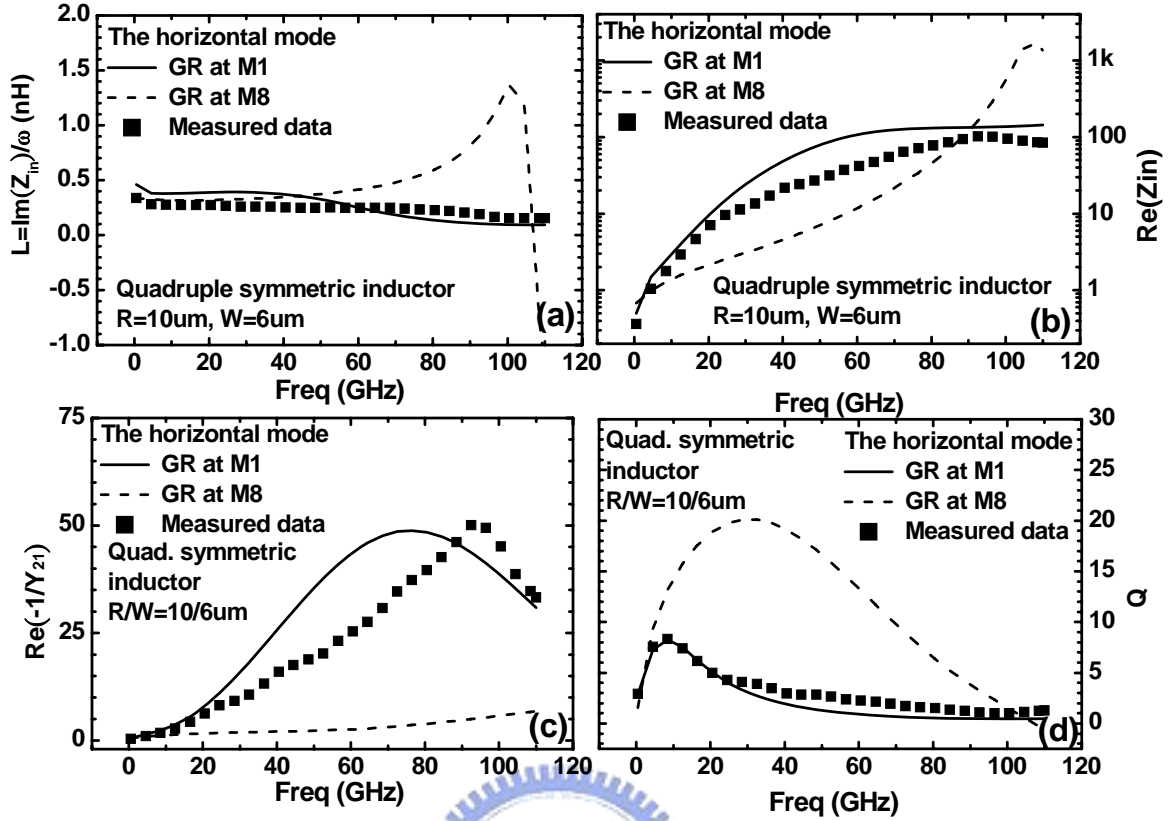


Figure 3.5 Comparison between measurement and HFSS simulation using horizontal injection mode with different guard ring (GR) layouts, at M1 and M8 respectively. (a) $\text{Im}(Z_{in})/\omega$ (b) $\text{Re}(Z_{in})$ (c) $R_s = \text{Re}(-1/Y_{21})$, and (d) $Q = \text{Im}(Z_{in})/\text{Re}(Z_{in})$.

3.3 HFSS simulation condition setup

In a real process, spiral inductors adopted in this work were fabricated by $0.13\mu\text{m}$ back end technology with eight layers of Cu and FGS as the inter-metal dielectric (IMD). However, it is a difficult task using an EM simulator like HFSS to build a 3D structure, which exactly follows the 3D topology consisting of multi-layer metal (Cu), IMD, and vias. The major problems are excessive computation time as well as memories, and the introduced failure in convergence.

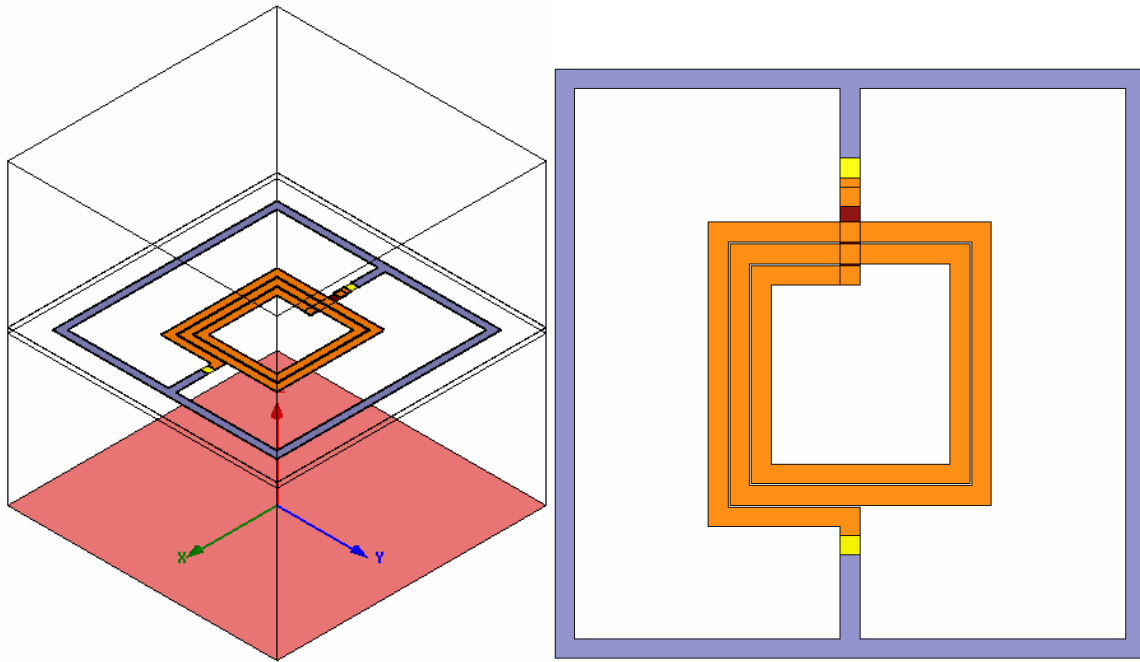


Figure 3.6 Inductor structure setup for HFSS simulation (a) a 3D structure incorporating spiral inductor and guard ring (b) a 2D layout from a projection of the original 3D structure in (a).

Fig. 3.6 illustrates the 3D structure and 2D layout of a spiral inductor built for HFSS simulation. In a real process such as 0.13 μm back-end technology for fabricating on-chip inductors, the 3D structure incorporates 8 layers of metals (Cu) and composite dielectric layers in the IMD. To simplify the problem for EM simulation, an effective dielectric constant $\epsilon_{r,eff}$ corresponding to the composite dielectric layers, was derived from eqs. (3.1) ~ (3.2), based on a simple theory of series capacitance.

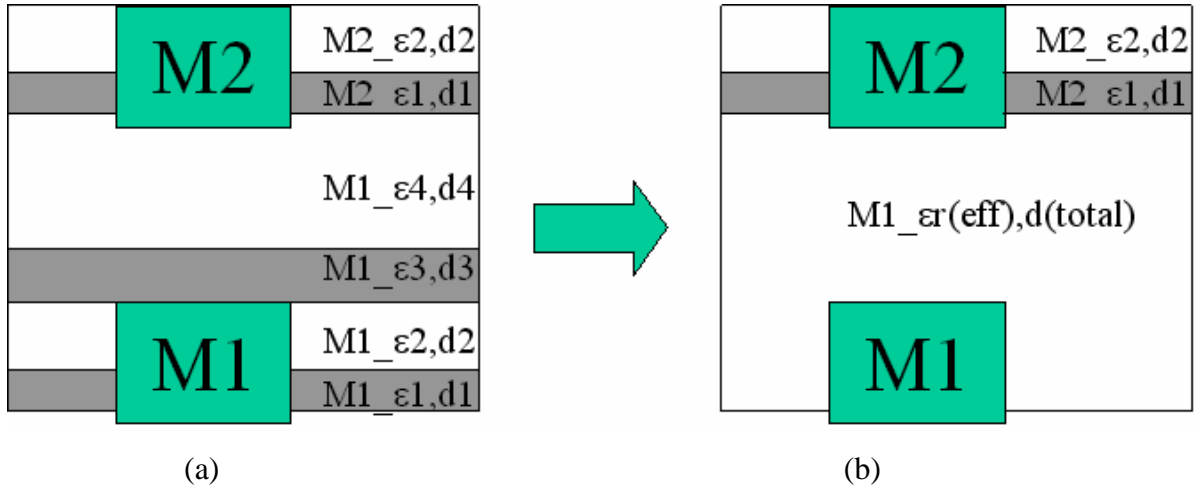


Figure 3.7 (a) Multi-layer metals and inter-metal dielectrics with various dielectric constants and thicknesses and Effective oxide dielectric constant and thickness (b) effective dielectric constant representing the composite dielectric layers.

$$D_{eff} = \sum_{i=1}^n d_i \quad (3.1)$$

$$\epsilon_{r,eff} = D_{eff} \times \left(\sum_{i=1}^n \frac{d_i}{\epsilon_{ri}} \right)^{-1} \quad (3.2)$$

3.4 Electromagnetic theory for inductor analysis

For a spiral inductor with current flowing through the metal coils, a magnetic flux denoted as Φ_B can be generated through the area enclosed by the winding coils. The magnetic flux Φ_B is defined as a product of the average magnetic field B times the normal component of the area that it penetrate and given by (3.3). Notes that the average magnetic field B is also named as magnetic flux density.

$$\Phi_B = \oint_C \vec{B} \cdot d\vec{s} \quad (3.3)$$

According to Biot-Savart law, the magnetic field B corresponding to a close loop of metal conducting with current of I can be calculated by (3.4) [4]

$$B = \frac{\mu_0 I}{4\pi} \oint_C \frac{d\vec{l} \times \vec{a}_R}{R^2} \quad (3.4)$$

(3.4) indicates that the magnetic field B is proportional to current I flowing in the metal coil, and then the magnetic flux Φ_B derived from the product of B and area, given in (3.3) follows the proportional relation with respect to I . The proportional coefficient between Φ_B and I is denoted as inductance L in (3.5)

$$\Phi_B = L \cdot I \quad (3.5)$$

If there are N turns of coil in a spiral inductor, the total magnetic flux Λ and the corresponding inductance L are expressed as [4]

$$\Lambda = N \cdot \Phi_B = L \cdot I$$

$$L = \frac{\Lambda}{I} \quad (3.6)$$

For spiral inductors applied in RF circuits operating in high frequencies up to GHz, the effective sheet resistance in the winding metals will increase dramatically above its DC value, namely skin effect. As a result, the conductor losses in the winding metals include not only the joule heating from DC resistance at sufficiently low frequency but also skin effect introduced excess losses, which increases with increasing frequency. The skin effect imposed on a spiral inductor under high frequency operation leads to increase of input impedance $\text{Re}(Z_{in})$ and Q degradation. Besides skin effect, proximity effect is one more important mechanism responsible for increase of effective resistance and Q degradation, which becomes significant for spiral inductors with multi-turn coils. The DC resistance can be easily calculated by the product of metal sheet resistance (static state) and the square number defined by total length over width, as written in (3.7). However, the frequency dependent resistance due to skin effect and proximity is difficult to analyze precisely and sometimes requires EM simulation for a quantitative assessment or prediction.

3.4.1 Conductor loss – Skin effect and Proximity effect

For a conductor operating at sufficiently low frequency, its DC resistance can be calculated by (3.7), in which the sheet resistance R_{sh} refers to the process parameters dependent on each individual metal layer,

$$R_{dc} = R_{sh} \times \frac{\ell}{w}$$

where

R_{sh} : metal sheet resistance in unit of Ω/\square (3.7)

ℓ : metal total length

w : metal width

Regarding the frequency dependence of effective trace resistance under high frequency to several GHz and beyond, EM simulation was performed to identify the current distribution and investigate the underlying mechanisms. Fig. 3.8 presents the current distribution across the conductor and reveals non-uniform distribution with an obvious current crowding near the conductor surface. The phenomenon is known as skin effect.

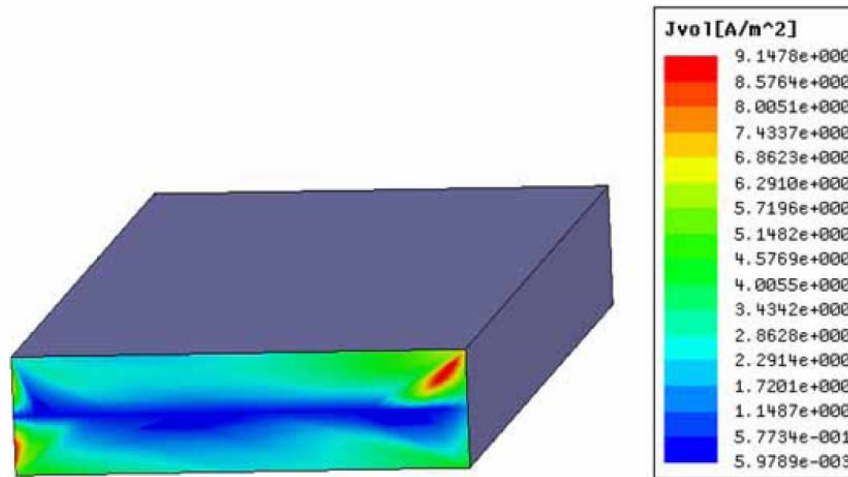


Figure 3.8 EM (HFSS) simulation reveals skin effect apparent in the conductors in which non-uniform current distribution and current crowding near surface will lead to increase of effective resistance in conductors under high frequency operation.

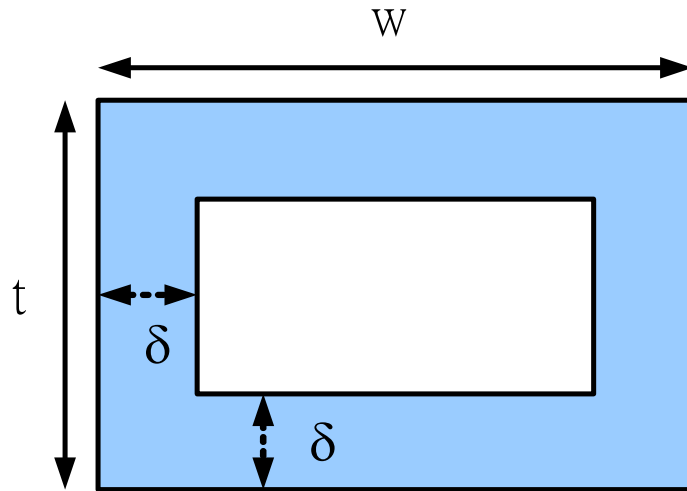


Figure 3.9 The cross section and skin depth definition in a metal line for the analysis of non-uniform current distribution under high frequency operation

For an analysis and modeling of the skin effect, a skin depth δ was specified in Fig. 3.9 in a metal line and used to model the non-uniform current distribution across the metal given by (3.8), in which the current density decay from the maximum value at surface J_0 to the center according to an exponentially decreasing function. The skin depth δ was modeled as shown in (3.9), in which the higher frequency or the higher metal conductivity σ will lead to thinner skin depth and then aggravated skin effect. Taking Cu as an example, its metal conductivity $\sigma = 5.531 \times 10^7 \text{ } \Omega/m$ will result in a skin depth δ of around $2.1 \mu\text{m}$ at 1.0 GHz and as thin as $0.93 \mu\text{m}$ at 5.0 GHz, which is much thinner than metal width in general applications, including logic, analog, and RF circuits.

$$J(y) = J_0 \times e^{-\frac{y}{\delta}} \quad (3.8)$$

Skin effect is defined by skin depth δ in which most of the current is localized at high frequency. The skin depth (δ) is calculated by equation (3.9). Show the electric field decays and reaches surface electric field $\frac{1}{e}$ times of largest thickness.

$$\delta = \sqrt{\frac{2}{\omega\mu_0\sigma}} \quad (3.9)$$

The current (I) is obtained by integrating the current density J over the wire cross-sectional area. Since J only varies in the y direction (Fig.3.8), I can be calculated as

$$I = \int_s \bar{J} \cdot d\bar{s} = J_0 w \delta (1 - e^{-\frac{t}{\delta}}) \quad (3.10)$$

where t is the physical thickness of the wire. The frequency dependent thickness appearing in the last term of (3.10) is defined as an effective thickness,

$$t_{eff}(\omega) = \delta (1 - e^{-\frac{t}{\delta}}) \quad (3.11)$$

The dc series resistance, R_{dc} , free from frequency dependence can be expressed as

$$R_{dc} = \frac{\ell}{\sigma A} = R_{sh} \frac{\ell}{w} \quad (3.12)$$

where A is the area of the cross-section, and R_{sh} is the resistance per unit area. The frequency dependent series resistance, due to skin effect can be derived based on R_{dc} and frequency dependence in t_{eff} as follows

$$R_s(\omega) = \frac{\ell}{\sigma A_{eff}(\omega)} \quad (3.13)$$

where

$$A_{eff}(\omega) = w \cdot t_{eff}(\omega)$$

$$R_s(\omega) = \frac{\ell}{\sigma w \delta (1 - e^{-\frac{t}{\delta}})} \quad (3.14)$$

Note that the increase of effective series resistance, due to skin effect approaches an asymptote following a square root function of the frequency given in (3.14). In comparison, proximity effect presents a strong function of frequency and may lead to resistance increase at a higher than linear rate and dominate Q degradation at higher frequency. In the following, 3D EM simulation was carried out to investigate the proximity effect on current distribution in a multi-turn spiral inductor under increasing frequency and its impact on effective resistance. For very low frequency at 0.01 GHz as

shown Fig. 3.10, the current flow in the metal trace presents a uniform distribution. However, for increasing frequency to 10 GHz, as shown in Fig. 3.11, the EM simulation reveals dramatically non-uniform current distribution in the multi-turn metal coils. Proximity effect originated from EM field coupling between adjacent coils is proposed as the mechanism besides skin effect, responsible for current re-distribution and increase of resistance at sufficiently high frequency.

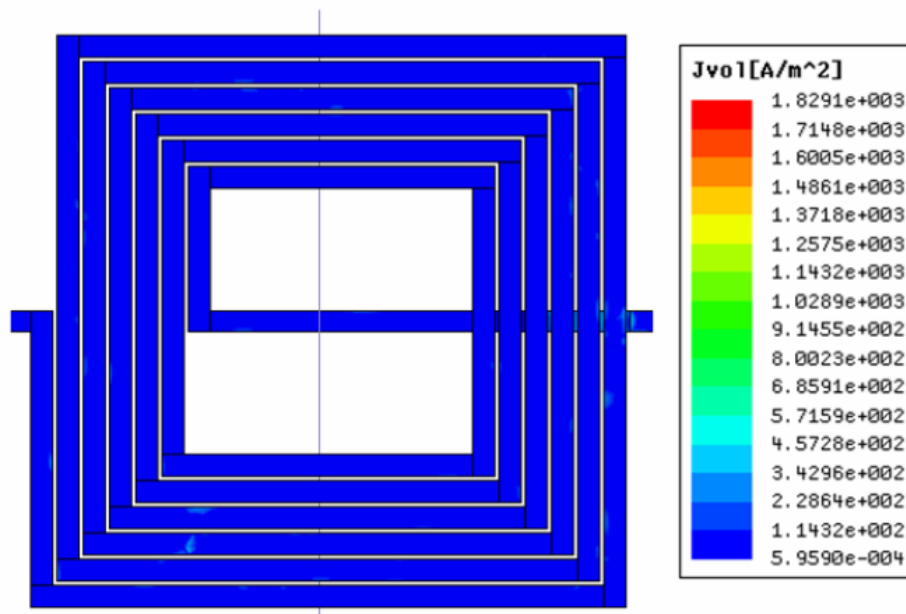


Figure 3.10 Current density distribution in the multi-turn metal coils of an inductor, at very low frequency 0.01 GHz. The EM simulation done by HFSS indicates a perfect uniform distribution in the metal trace, free from current crowding effect.

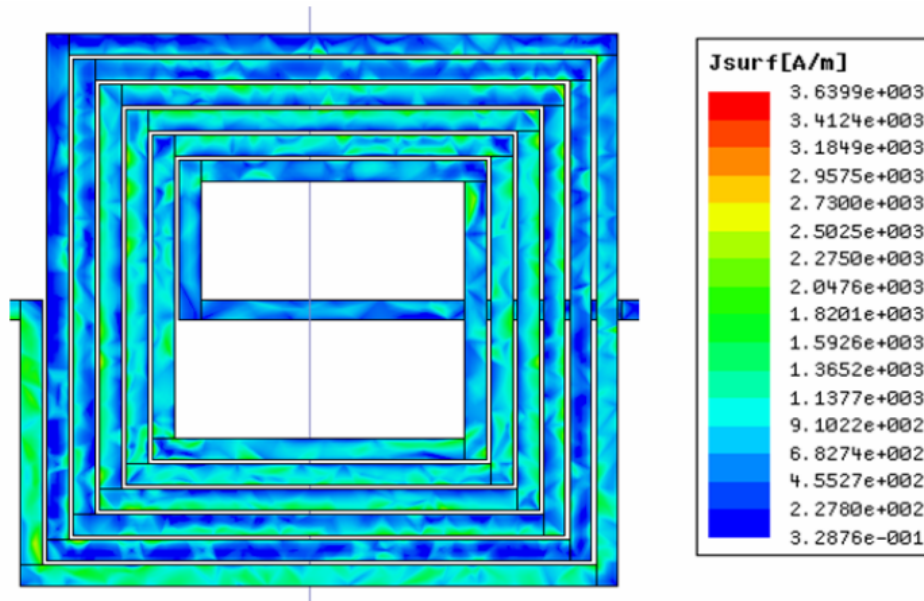


Figure 3.11 Current density distribution in the multi-turn metal coils of an inductor, at very high frequency, 10 GHz. The EM simulation done by HFSS indicates a dramatic non-uniform current distribution in the metal trace, accounting for proximity effect.

Even though the proximity effect induced current crowding has been known for a long time, and the general mechanism was cited and interpreted in couple of literatures. However, quite few works were done to realize a quantitative prediction without resort to numerical simulation. In this thesis, an analytical model will be derived to calculate and predict the frequency dependent resistance associated with proximity effect and facilitate an accurate prediction of Q at very high frequency.

The basic mechanism underlying the current crowding originated from proximity effect can be understood through an illustration in Fig. 3.12. The magnetic field B in the adjacent coil penetrates the target metal trace in the direction normal to the surface. According to Lenz's law, eddy currents will be created in the target metal trace with a direction to generate a magnetic flux opposite to that introduced from the adjacent coil. As a result, the generated eddy currents add to the excitation current on the inner edge (near the center of spiral coils) while subtract from the excitation current on the outer edge. It explains why the current crowding was created and the dramatic increase of effective

resistance.

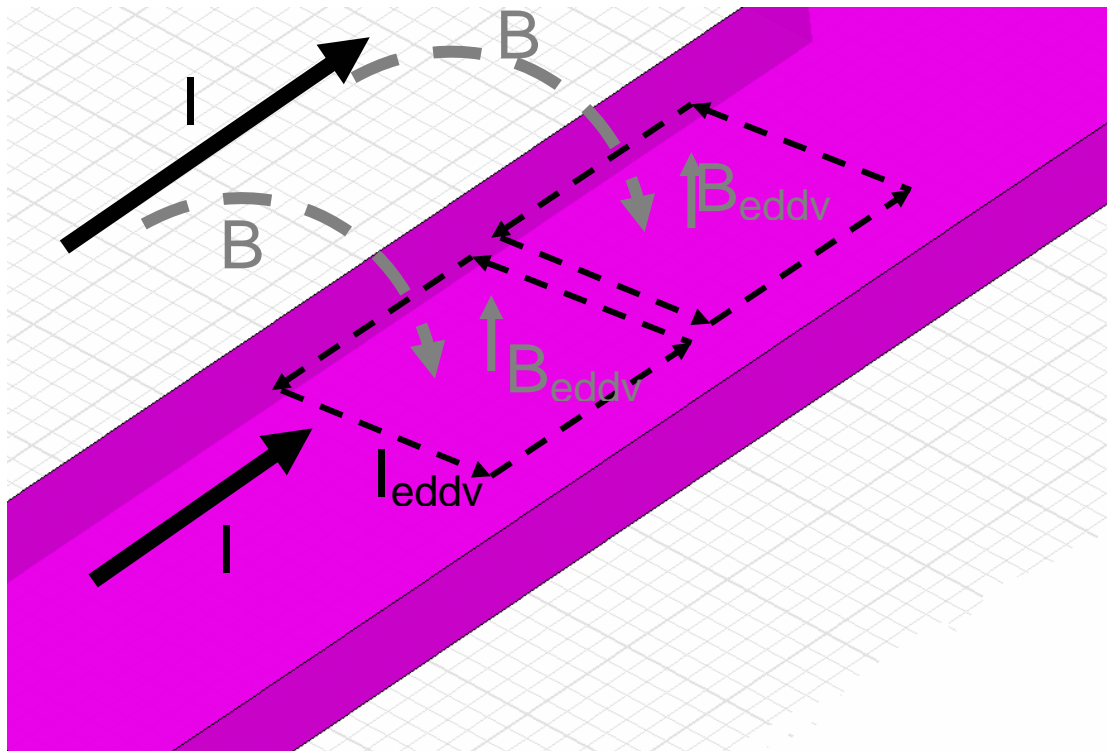


Figure 3.12 Eddy currents generated according to Lenz's law, with a direction in phase with excitation current on the inner edge (near the center of spiral coils) but opposite to the excitation current on the outer edge. The phenomenon explains current crowding caused by proximity effect in multi-turn spiral inductors.

Applying the mentioned theory in a multi-turn spiral inductor as shown in Fig. 3.13, it can facilitate an understanding of the proximity effect. The eddy current opposite to the excitation current on the edge near the adjacent coil leads to non-uniform current distribution revealed by EM simulation in Fig. 3.11. Note that proximity effect becomes significant at sufficiently high frequency and dominates skin effect as mentioned previously.

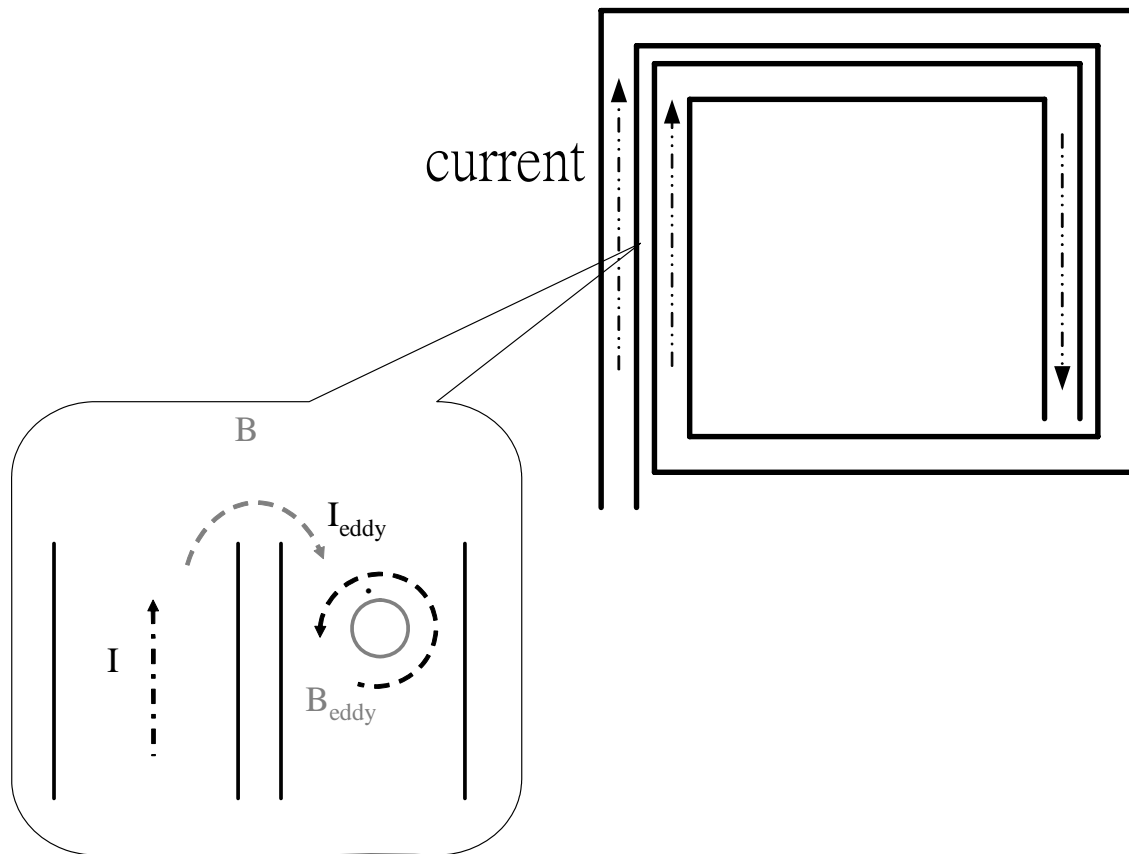


Figure 3.13 Eddy currents generated according to Lenz's law, with a direction in phase with excitation current on the inner edge (near the center of spiral coils) but opposite to the excitation current on the outer edge. The phenomenon explains current crowding caused by proximity effect in multi-turn spiral inductors.

In the following, analytical models will be derived for calculating the effective resistance associated with eddy currents due to proximity effect denoted as \overline{R}_{eddy} , and the introduced excess power loss defined as P_{eddy} .

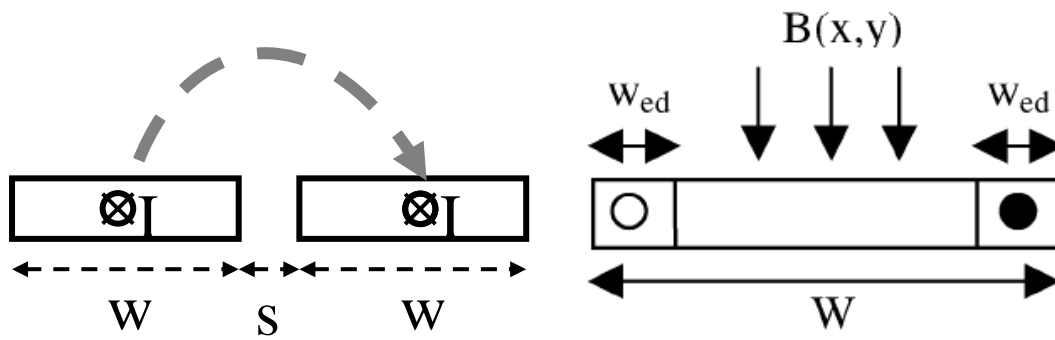


Figure 3.14 Cross section of a metal trace showing the normal magnetic field $B(x, y)$, and eddy current flowing round the edges within a width of w_{ed} .

Figure 3.14 shows the eddy current induced in a metal trace due to magnetic fields from adjacent conducting wires where $B(x, y)$ is the magnetic flux density normal to the metal segment. EM simulations show that the distribution of current induced by an external magnetic field occurs along the width of the metal trace, and not across its thickness. Eddy current introduced in a metal trace due to magnetic fields from neighboring wires follows Lenz's law and leads to current crowding effect, so called proximity effect. Therefore, we assume that the eddy current flows near the edges of the metal only within an effective width of w_{ed} . Though $B(x, y)$ varies within the segment, for the sake of a simple analytical formula, it is reasonable to assume a constant B , which is approximately the value at the middle of the metal trace along the center line. B is calculated from the excitation current in all other parallel metal wires in the inductor. Note that the contribution of eddy currents in another segment toward B will roughly cancel since they flow in opposite directions at the two edges of a segment. Assume that there is on phase delay between the excitation currents in different traces, which is acceptable for the inductor size and frequency range studied.

Based on Ampere's law, the magnetic field at a distance r from an infinite wire conducting a current I can be expressed as

$$B = \frac{\mu_0 I}{2\pi r} \quad (3.15)$$

The magnetic field B introduced from the neighboring metal wire can be derived as

$$B(i) = \frac{\mu_0 I}{2\pi(w + s)} \quad (3.16)$$

In equation (3.16), w is the width of the metal wire, s is the distance between two adjacent wires

According to Faraday's law of electromagnetic induction, an electromagnetic field (emf) can be induced by the time varying magnetic flux introduced from adjacent metal wire addressed in (3.15)~(3.16). The emf was generated around a close loop in the conductor and created an electric field in the loop, given by (3.17)

$$\begin{aligned} \text{Faraday law : } \nabla \times \bar{E} &= -\frac{\partial \bar{B}}{\partial t} \\ \text{emf} &= \oint_c \bar{E} \cdot d\bar{l} = -\frac{d\Phi_B}{dt} \\ \Phi_B &= \int_s \bar{B} \cdot d\bar{s} \end{aligned} \quad (3.17)$$

Concurrently, the emf acting on the conducting material generated a current around the loop, namely eddy current. The induced eddy current corresponds to the electric field following ohm's law, expressed in (3.18). In accordance with Faraday's law, the eddy currents dissipate energy and create a magnetic field that tends to oppose the change in the magnetic flux

Following (3.17) and the cross section of winding metal with induced magnetic field in Fig. 3.15, the electrical field and eddy current can be derived as follows.

$$\oint_c \vec{E} \cdot d\vec{l} = E\ell \quad (3.18)$$

$$-\frac{d}{dt} \int_s \vec{B} \cdot d\vec{s} = \omega B\ell x \quad (3.19)$$

(3.17) ~ (3.19) to derive E

$$E = \omega Bx \quad (3.20)$$

According to ohm's law

$$J_{eddy} = \sigma E = \sigma \omega Bx \quad (3.21)$$

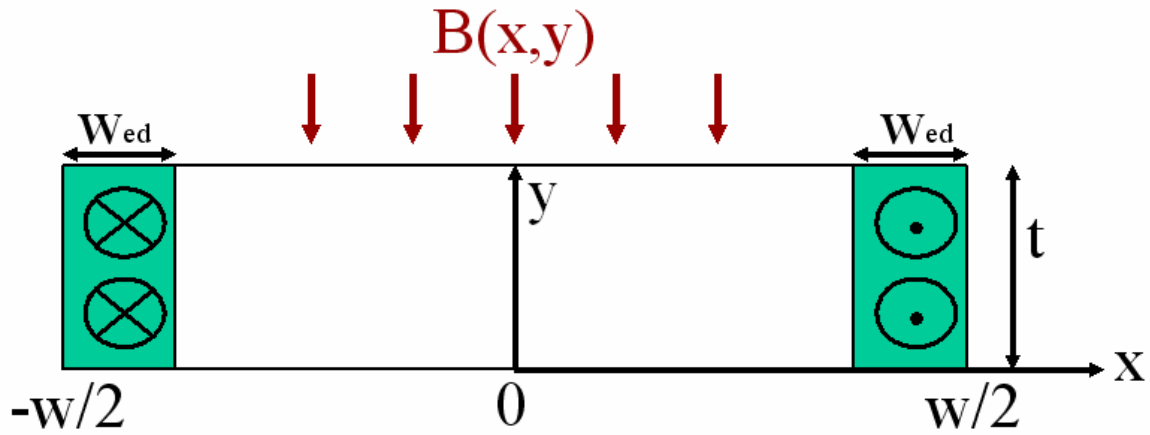


Figure 3.15 Cross section of a metal trace showing the normal magnetic field $B(x,y)$, and eddy current flowing within a width w_{ed} round the edges

The eddy currents introduced from adjacent metal wires, due to proximity effect become another source of power dissipation and Q degradation in spiral inductors. The power dissipation due to proximity effect induced eddy currents can be calculated as follows. First, specify the eddy currents flow within a finite width of w_{ed} around the edges of a metal trace, as shown in Fig. 3.15. The power dissipation P_{eddy} is treated as the joule heating associated with eddy currents I_{eddy} confined in w_{ed} around edges of the metal trace in two sides, and the corresponding resistance defined as R_{eddy} . Based on the

argument, the formulas are derived in the following.

$$P_{eddy}(i) = R_{eddy} I_{eddy}^2 \quad (3.22)$$

$$R_{eddy}(x) = \frac{\ell}{\sigma A(x)} = \frac{\ell}{\sigma t \cdot dx} \quad (3.23)$$

$$I_{eddy}(x) = J_{eddy}(x) \times t \cdot dx \quad (3.24)$$

From (3.21) ~ (3.24)

$$P_{eddy}(i) = 2 \times \int_0^{w_{ed}} \underbrace{\frac{1}{\sigma t dx}}_{R(x)} \underbrace{(\sigma \omega B(i) x t dx)^2}_{I^2} \quad (3.25)$$

Taking $B(i)$ derived in (3.16)

$$P_{eddy}(i) = \left[\frac{\ell t \sigma \omega^2 \mu_0^2 I^2}{6\pi^2 (w+s)^2} \left(\left(\frac{w}{2}\right)^3 - \left(\frac{w}{2} - w_{ed}\right)^3 \right) \right] I^2 \quad (3.26)$$

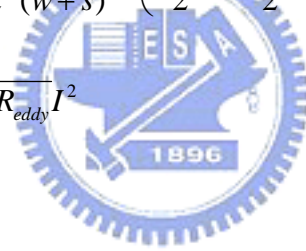
where I is the excitation current in the metal wire

Define $\overline{R_{eddy}}$ as the effective resistance due to eddy current

$$\overline{R_{eddy}} = \frac{\ell t \sigma \omega^2 \mu_0^2}{6\pi^2 (w+s)^2} \left(\left(\frac{w}{2}\right)^3 - \left(\frac{w}{2} - w_{ed}\right)^3 \right) \quad (3.27)$$

then

$$P_{eddy}(i) = \overline{R_{eddy}} I^2 \quad (3.28)$$



Assume that the distribution of eddy currents is analogous to that of excitation currents I due to skin effect. Then w_{ed} is defined as a skin depth given by (3.11). Then the effective resistance due to eddy currents $\overline{R_{eddy}}$ can be further derived as follows.

$$w_{ed} = \delta \left(1 - e^{-\frac{w}{\delta}}\right) \quad (3.29)$$

$$\overline{R_{eddy}} = \frac{\ell t \sigma \omega^2 \mu_0^2}{6\pi^2 (w+s)^2} \left\{ \left(\frac{w}{2}\right)^3 - \left[\frac{w}{2} - \delta \left(1 - e^{-\frac{w}{\delta}}\right) \right]^3 \right\} \quad (3.30)$$

$$\delta = \sqrt{\frac{2}{\omega \mu_0 \sigma}}$$

According to above inference, the total power dissipation and the corresponding series resistance under high frequency, namely R_{ac} can be revised to contain skin effect

and proximity effect.

$$P_{ac} = P_{skin} + P_{eddy} \quad (3.31)$$

$$P_{skin} = R_{skin} I^2 \quad (3.32)$$

$$P_{eddy} = \overline{R_{eddy}} I^2 \quad (3.33)$$

$$P_{ac} = R_{ac} I^2 = (R_{skin} + \overline{R_{eddy}}) I^2 \quad (3.34)$$

so

$$R_{ac} = R_{skin} + \overline{R_{eddy}} \quad (3.35)$$

where R_{skin} is the resistance incorporating skin effect given in (3.14)

$$R_{skin} = R_s(\omega) = \frac{\ell}{\sigma w \delta (1 - e^{-\frac{t}{\delta}})} \quad (3.36)$$

$\overline{R_{eddy}}$ is the effective resistance due to proximity effect, written in (3.30)

$$\overline{R_{eddy}} = \frac{\ell t \sigma \omega^2 \mu_0^2}{6\pi^2 (w+s)^2} \left\{ \left(\frac{w}{2} \right)^3 - \left[\frac{w}{2} - \delta (1 - e^{-\frac{w}{\delta}}) \right]^3 \right\} \quad (3.37)$$

then the series resistance under high frequency R_{ac} containing both skin effect and proximity effect can be expressed as

$$R_{ac} = \frac{\ell}{\sigma w \delta (1 - e^{-\frac{t}{\delta}})} + \frac{\ell t \sigma \omega^2 \mu_0^2}{6\pi^2 (w+s)^2} \left\{ \left(\frac{w}{2} \right)^3 - \left[\frac{w}{2} - \delta (1 - e^{-\frac{w}{\delta}}) \right]^3 \right\} \quad (3.38)$$

3.4.2 Substrate loss – Capacitive coupling and Inductive eddy currents

In addition to the conductor losses contributed from skin effect and proximity addressed in section 3.4.1, substrate losses is one more important factor responsible energy loss and Q degradation in on-chip inductors. According to Maxwell equations for EM analysis, there are two kinds of different mechanisms responsible for the substrate losses. One is electric loss caused by capacitive coupling effect, and another one is the magnetic loss due to eddy currents induced by the magnetic coupling, both between the metal coils and the semiconducting substrate underneath. The capacitive coupling effect can be understood by Gauss law and the magnetic coupling can be explained by Faraday and Lenz's law as addressed previously (section 3.4.1) for conductor losses. Note that substrate losses tend to increase dramatically with increasing frequency and may dominate proximity effect as the primary factor responsible for f_{SR} as well as Q degradation. This

subject and associated challenges stimulate our motivation in this work to overcome substrate losses and conductor losses for achieving broadband inductors with f_{SR} up to 70 GHz.

Fig. 3.16 presents analysis of input impedance $\text{Re}(Z_{in})$ for conventional symmetric inductor by using full wave EM simulation and simplified model incorporating proximity effect. The comparison with measurement indicates the simplified model with proximity effect only under-estimates $\text{Re}(Z_{in})$, due to inappropriate neglect of substrate loss effects. As for a quadruple semi-symmetric inductor shown in Fig. 3.17, a new symmetric inductor realized in this work for broadband design, the comparison with measurement indicates the simplified model with proximity effect can fit $\text{Re}(Z_{in})$ of this new symmetric inductor. Through a careful analysis and comparison on the inductor layouts and geometries, it can be identified that conventional symmetric inductors suffer worse substrate coupling introduced energy loss, due to larger capacitive coupling and magnetic coupling (eddy currents on the substrate). It accounts for the effective suppression of substrate losses in this new symmetric inductor and the mechanism contributing significant improvement in f_{SR} . Furthermore, EM simulation revealed a trade-off between proximity effect and substrate coupling in symmetric inductors with different layouts. For the conventional fully symmetric inductor with multi coils, the substrate coupling effect dominates proximity at higher frequency. As for the new symmetric inductors design for broadband design, proximity effect dominated even up to 100 GHz.

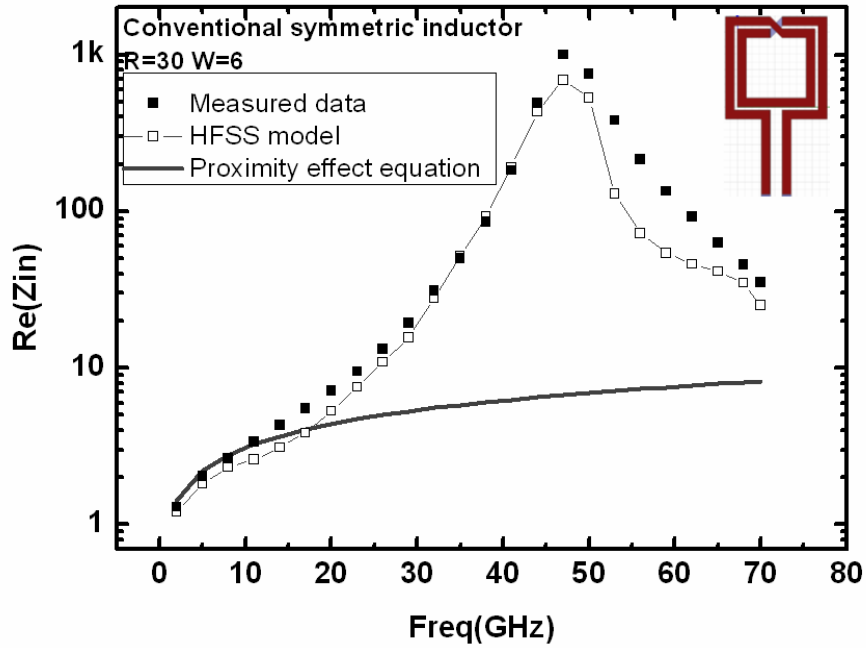


Figure 3.16 Analysis of input impedance $Re(Z_{in})$ for conventional symmetric inductor by full wave EM simulation and simplified model incorporating proximity effect. The comparison with measurement indicates the simplified model with proximity effect only under-estimates $Re(Z_{in})$.

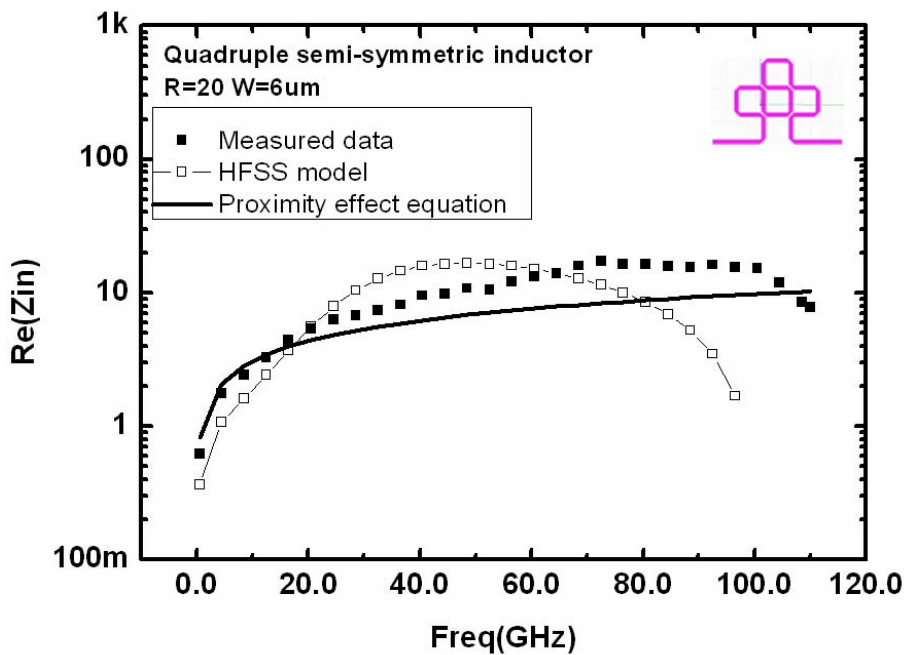


Figure 3.17 Analysis of input impedance $Re(Z_{in})$ for quadruple semi-symmetric inductor (new design for broadband applications) by full wave EM simulation and analytical model incorporating proximity effect. The comparison with measurement indicates the simplified model with proximity effect can fit $Re(Z_{in})$ of quadruple semi-symmetric inductor.

Chapter 4

Broadband and symmetric Inductor Design

With the advancement of Si CMOS technology and its advantages in high speed, high integration level, and low cost, Si RF CMOS becomes a vital technology to realize a single-chip communication integrated circuit. Going with the development path, on-chip inductors become a key component in RF integrated circuits such as LNA, VCO, filters, and impedance matching networks, and will determine RF circuit performance in terms of gain, power, and noise. However, the on-chip inductor design faces several challenges, such as broadband and high-Q, as well as area estate. The major difficulty comes from the energy loss associated with low resistivity Si substrate. The lossy substrate introduces challenges, not only in performance optimization but also in simulation and modeling.

In recent years, symmetric inductors were proposed to replace widely used spiral inductors for achieving higher Q and broader band at a smaller area. Moreover, two-port symmetry as an intrinsic property of symmetric inductors is an important feature desired for widely used differential circuits for low noise and high gain design

In this thesis, new symmetric inductors with features of broadband and high-Q will be design with performance target of $f_{SR} \geq 70$ GHz and $Q_{max} \geq 15$ to enable applications in V-band microwave circuits. 3D EM simulation was performed to guide layout design for achieving the target performance. Some critical issues emerging from this practice on small inductor design in terms of EM simulation, ultra-high frequency measurement, and de-embedding methods will be discussed.

4.1 Symmetric inductor design and fabrication

As mentioned previously, on-chip inductors become a critically important component in RF circuits such as VCO, LNA, and impedance matching networks. For conventional inductors, quality factor Q and self-resonance frequency f_{SR} are well known parameters affecting RF circuit performance. As for differential circuit topology widely used in analog and RF circuits, the differential excitation (i.e., voltages and currents of two signals are 180° out of phase but with the same magnitude) has become an important operation mode of choice. It is because that differential mode operations can provide better noise immunity and higher gain. Taking this advantage for broadband and low noise design, symmetric inductors with new layouts and geometries were designed and fabricated in this work.

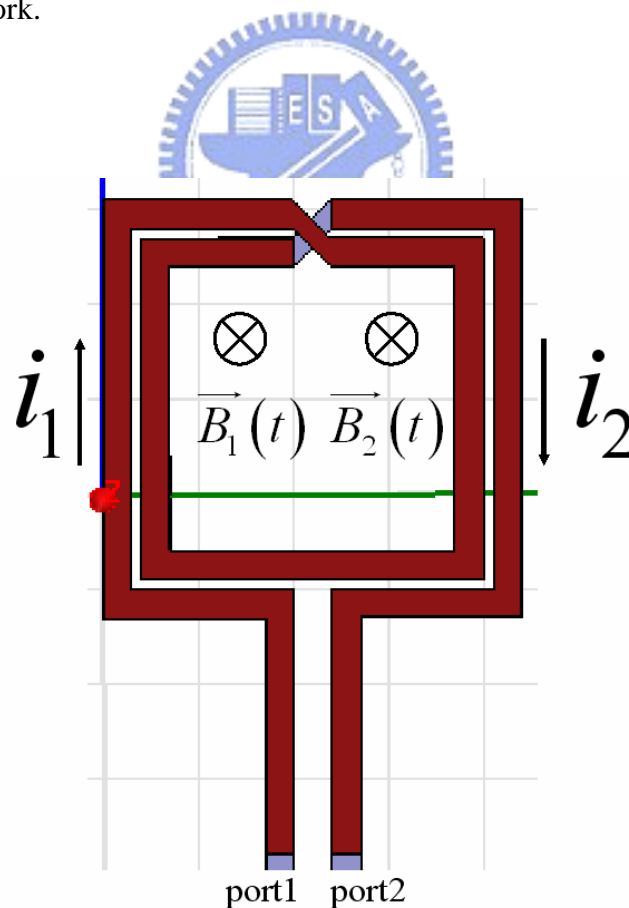
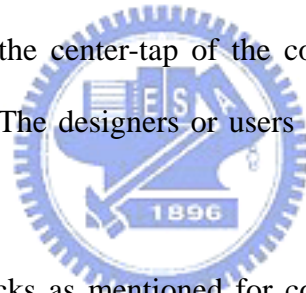


Figure 4.1 The layout of a conventional differential inductor.

First, the conventional symmetric inductor illustrated in Fig. 4.1 was designed for differential excitation (i.e., voltages and current at port 1 and port 2 are 180° out of phase). When driven differentially, the voltages on adjacent conducting strips are anti-phase, however, current flows in the same direction along each adjacent conductor shown in Fig. 4.1 (i.e., signal currents i_1 and i_2 flow in the same direction on any side). This reinforces the magnetic field produced by the parallel groups of conductors and increases the overall inductance per unit area. However, the conventional differential inductor is not really symmetrical in geometry. As shown in Fig. 4.1, we have to use the top metal to crossover the second to top metal at the intersection. The two signals would no longer be 180° out of phase after they flew through the intersection since they have passed different paths and materials. And for some applications, circuit designer has to use a differential inductor with center-tap. But the center-tap of the conventional differential inductor as defined is not the real center. The designers or users cannot even know where the exact center is.



To overcome the drawbacks as mentioned for conventional symmetric inductors, a fully symmetric inductor was proposed [12]. As shown in Fig. 4.2, its layout is fully symmetrical in geometry and electricity and the center tap as defined is no doubt to be the real center. In order to compare the symmetrical characteristic, high frequency performance, and potential trade-off between conventional and fully symmetric inductors, layout and fabrication for these two kinds of inductors with the same metal trace width, space, and similar length were done on the same test chip.

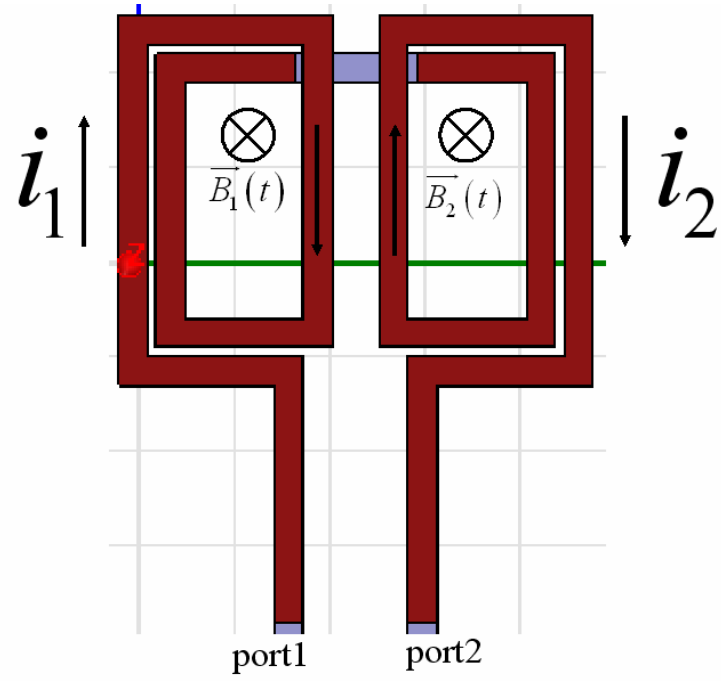


Figure 4.2 The layout of a fully symmetrical inductor.

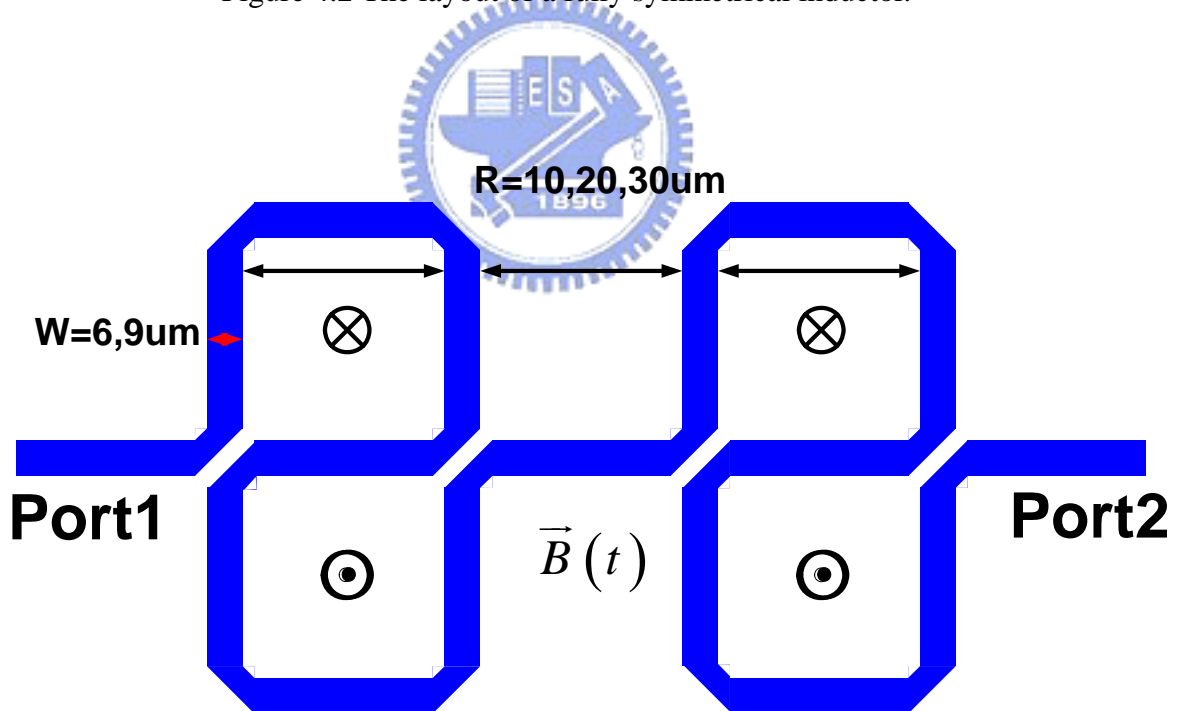


Figure 4.3 The layout of a quadruple symmetric inductor.

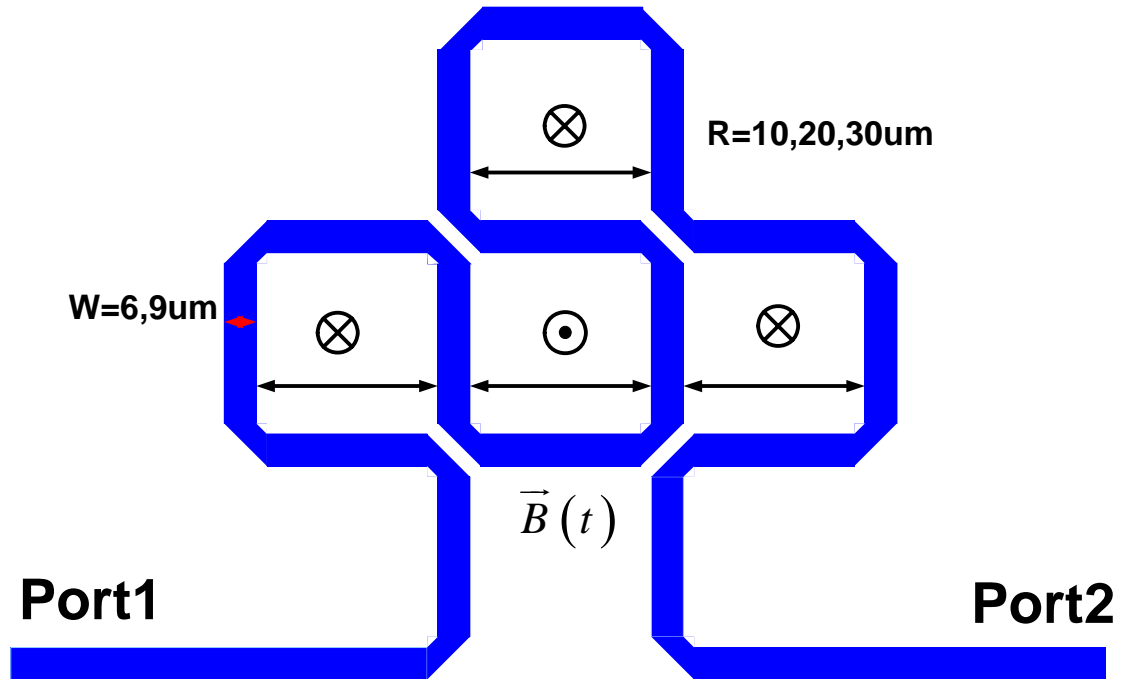


Figure 4.4 The layout of a quadruple semi-symmetric inductor.

In addition to conventional and fully symmetric inductors, new symmetric inductors with novel layout and structure design, namely quadruple symmetric and semi-symmetric inductors are proposed in this work to overcome the drawbacks and potential trade-offs in existing ones. For this objective, $0.13\mu\text{m}$ RF CMOS process was adopted to fabricate the proposed new symmetric inductors. Totally, eight layers of metal by Cu are available and the top metal (metal-8) thickness is $3.35\mu\text{m}$. The proposed novel symmetric inductors as shown in Fig. 4.3 and Fig. 4.4 can solve the asymmetry problem suffered by conventional symmetric inductors. However, there maybe appear a potential trade-off with performance such as degraded mutual inductance and resulted smaller Q, which are similar with those of fully symmetric inductors.

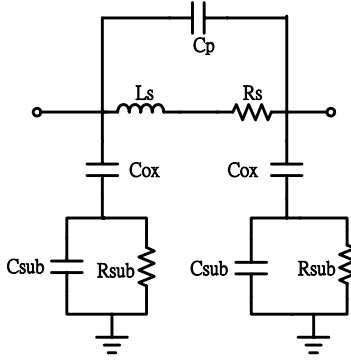
4.2 EM simulation for layout optimization

To meet the performance target, such as $f_{SR} \geq 70$ GHz and $Q_{max} \geq 15$ specified for broadband RFIC design, an analysis on single- π model was performed to identify the model parameters effect on three key performance factors like Q_{max} , f_{max} , and f_{SR} . single- π model was selected due to its simplicity and acceptable confidence level in trend analysis, rather than precision over broadband of frequencies. The results as shown in Table 4.1 indicates helpful guideline for increasing Q_{max} as well as f_{SR} , and the trade-off between each other. It is demonstrated that the suppression of capacitive elements like C_{ox} , C_{sub} , and C_p can help increase f_{SR} and Q_{max} , simultaneously. Similarly, decrease of substrate resistance, R_{sub} can raise both f_{SR} and Q_{max} . Reducing the metal coil resistance R_s can improve Q_{max} , but nearly nothing to do with f_{SR} . As for the inductive element L_s , a trade-off between f_{SR} and Q_{max} appears. The smaller L_s can help increase f_{SR} but will degrade Q_{max} at the same time.

Based on this guideline from equivalent circuit analysis, new symmetric inductors with two kinds of layouts, namely quadruple symmetric and quadruple semi-symmetric inductors were designed, as shown in Fig. 4.3 and Fig. 4.4, respectively. Two primary features are incorporated in our new design. One is the elimination of adjacent metal traces for every individual coil to reduce proximity effect and the induced excess resistances at higher frequency that can help maintain sufficient Q over broader frequencies. Another one is top metal (M8) only for implementing spiral coils. The avoidance of metal-7 (M7) under M8 can potentially realize two advantages such as smaller C_p as well as C_{ox} , and lower R_s due to elimination of vias between different metal layers. This approach is considered a better one than patterned ground shielding (PGS) method in terms of higher f_{SR} . It is attributed to simultaneous suppression of capacitive and inductive coupling (eddy current). Note that the potential drawbacks as expected are the degradation of available magnetic induction represented by L_s and the limitation in Q improvement. In the

following, EM simulation will be performed to verify the proposed design concept.

Table 4.1 Equiavlent circuit model parameters effect on inductor performance Q_{\max} , f_{\max} and f_{SR} – singl- π model as an example.

	Q_{\max}	f_{\max}	f_{SR}
Cox ↑	↓	↓	↓
Csub ↑	↓	↓	↓
Rsub ↑	↑	↑	↑
Cp ↑	↓	↓	↓
Ls ↑	↑	↓	↓
Rs ↑	↓	↓	---

The first step for an inductor design is an appropriate selection of the optimized metal trace width in terms of minimal series resistance R_{ac} over high frequencies. Note that R_{ac} has been derived based on EM theory in section 3.4.1, in which R_{ac} is consisted of two components, given by $R_{ac} = R_{skin} + \overline{R_{eddy}}$ in (3.38), with expressions of R_{skin} in (3.36) and $\overline{R_{eddy}}$ in (3.37). For a specified metal width w and thickness t , $\overline{R_{eddy}}$ due to proximity effect increases proportionally with ω^2 and will eventually dominate R_{skin} at sufficiently high frequency. As for a specified frequency, the width dependences in opposite directions between R_{skin} and $\overline{R_{eddy}}$ as shown in (3.36) and (3.37) will lead to an optimal width corresponding to the minimal R_{ac} . Fig. 4.5 presents R_{skin} and $\overline{R_{eddy}}$ calculated under fixed metal thickness at $t=3.35 \mu\text{m}$ and over varying metal widths

in $W=1\sim 15\ \mu\text{m}$, associated with different frequencies $f = 1, 5, 10, 15, \text{ and } 20\text{GHz}$. The results exhibit the smaller R_{skin} while the larger $\overline{R_{eddy}}$ with increasing width over $1\sim 15\ \mu\text{m}$, and the significant dominance of $\overline{R_{eddy}}$ over R_{skin} at larger width and higher frequency. Fig. 4.6 indicates $R_{ac} = R_{skin} + \overline{R_{eddy}}$ under varying widths to look for the optimal width responsible for the minimal R_{ac} . It demonstrates a monotonical reduction of R_{ac} with increasing width at sufficiently low frequency $f < 10\ \text{GHz}$, but a turn-around curve with minimal R_{ac} at a certain width for increasing frequency beyond 10 GHz. The optimal widths responsible for the minimal R_{ac} are identified to be around $W = 9, 6, 4\ \mu\text{m}$ corresponding to $f = 10, 15, 20\ \text{GHz}$. To verify the prediction from the developed models incorporating skin effect and proximity effect, new symmetric inductors with $W = 6, 9\ \mu\text{m}$ were designed and fabricated in this work.

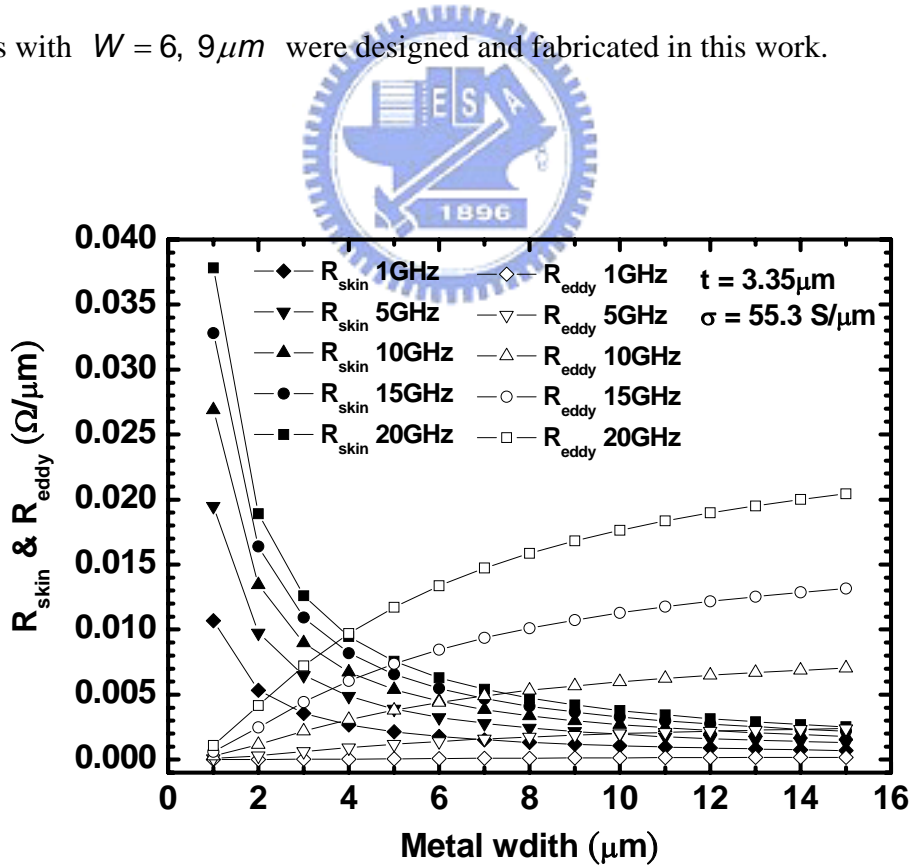


Figure 4.5 The series resistances due to skin effect and proximity effect R_{skin} and $\overline{R_{eddy}}$ calculated by (3.36) and (3.37) under specified metal thickness $t = 3.35\ \mu\text{m}$ and over varying widths $w = 1\sim 15\ \mu\text{m}$, associated with different operating frequencies

$f = 1, 5, 10, 15, 20 \text{ GHz}$.

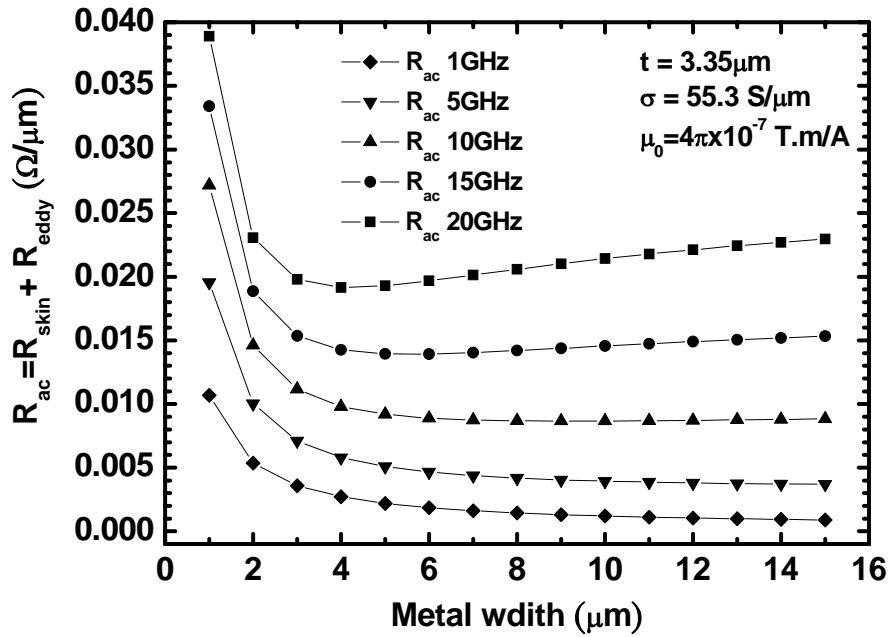


Figure 4.6 The total series resistance consisting of R_{skin} and $\overline{R_{eddy}}$ calculated by (3.38) under specified metal thickness $t = 3.35 \mu\text{m}$ and over varying widths $w = 1 \sim 15 \mu\text{m}$, associated with different operating frequencies $f = 1, 5, 10, 15, 20 \text{ GHz}$.

4.3 De-embedding structure design for new symmetric inductors

The S-parameters of the device under test (DUT) are measured using on-wafer testing with Agilent E8364B PNA and probe station as shown in Fig. 4.7. Two port measurement was performed using a pair GSG pads. As shown in Fig. 4.8, each GSG pad consists of one signal pad (S) at the center and two identical ground pads (G) at two sides. Note that every two pads have an interval of $100\text{-}\mu\text{m}$ between their centers, namely pad pitch of $100\text{-}\mu\text{m}$. Besides, a mask layer to remove the passivation should be laid out properly on the GSG-pads so that the probe is able to stab right onto the top metal layer. For two-port S-parameters measurement, two GSG-pads are placed at two sides with their ground pads connected together on chip, illustrated in Fig. 4.8. This connection is to make sure a common ground for two RF probes. In order to avoid undesired phenomena like eddy current interacting with DUT, an open loop for this ground connection must be ensured. A

general practice for this purpose is leaving two ground pads at the same side not connected at the lowest metal, i.e. M1.

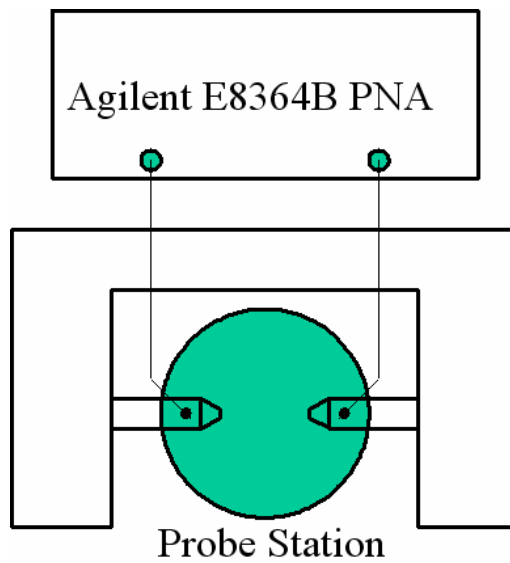


Figure 4.7 On-wafer measurement setup with Agilent E8364B PNA and probe station for two-port test structures.

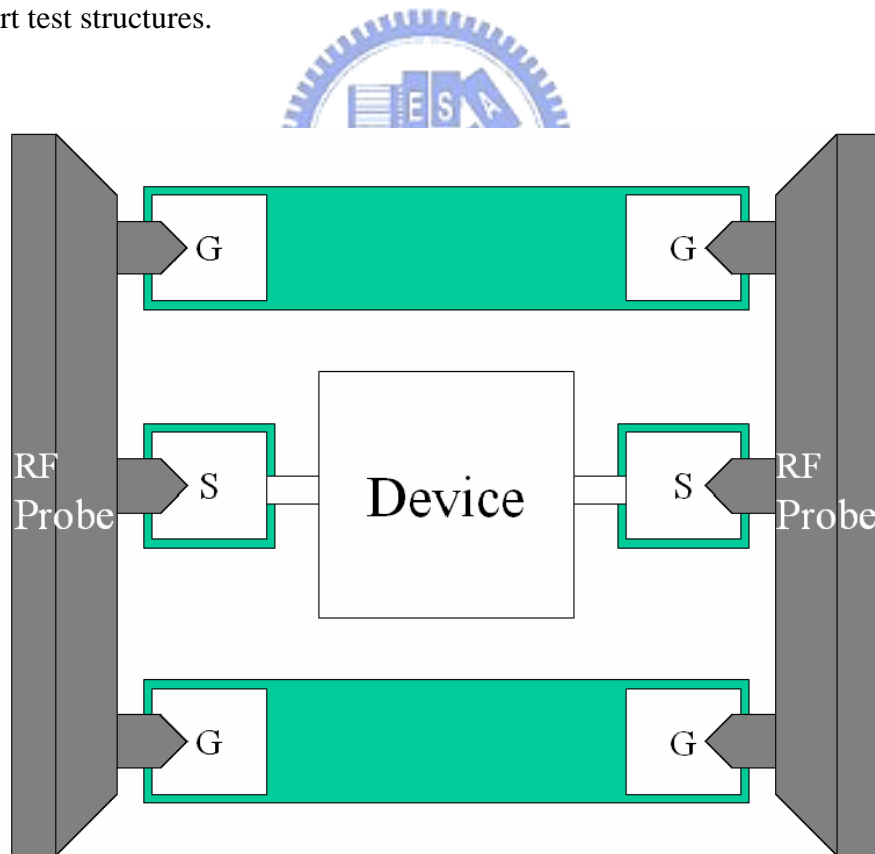


Figure 4.8 Coplanar GSG RF probes with the device under test (DUT) at the center enclosed by the pair of GSG pads.

The S-parameters achieved by measuring DUT in the test structure as shown in Fig. 4.8 will include the parasitic of the GSG-pads. Hence a procedure called “de-embedding” is required to extract the intrinsic S-parameters of the devices. Two step de-embedding method consisting of open and through or open and short dummy pads was recommended for a standard two-port test structure to remove the parasitic RLC from pads, interconnect lines, and substrate. Unfortunately, the through or short de-embedding intended for elimination of parasitic RL from sometimes leads to over or under de-embedding in miniaturized devices like very small inductors for broadband applications to 70 GHz and beyond. The errors originated from through or short de-embedding will introduce a dramatic deviation in intrinsic characteristics extracted and problem in equivalent circuit model development. To overcome this tough issue, a dedicated layout was designed for the small inductors as shown in Fig. 4.9, in which the DUT – a quadruple symmetric inductor is placed exactly in the center between two signal pads (S-pad) of the pair of GSG pads. In this way, the metal lines connecting DUT to two S-pads can be minimized in the distance and incorporated into the open dummy pad for de-embedding, and then through de-embedding can be saved with very minor difference. As a results, an open de-embedding with schematics and procedure illustrated in Fig. 4.10 can serve as an adequate de-embedding method with acceptable accuracy over broadband of frequencies.—

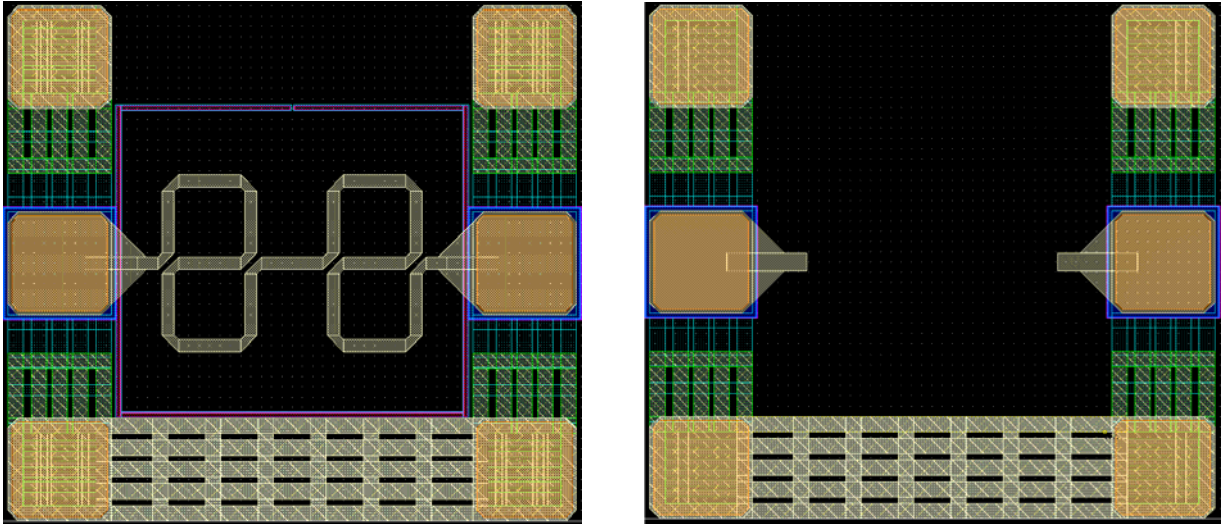


Figure 4.9 The layouts of a Quadruple symmetric inductor and open dummy pads for open de-embedding.

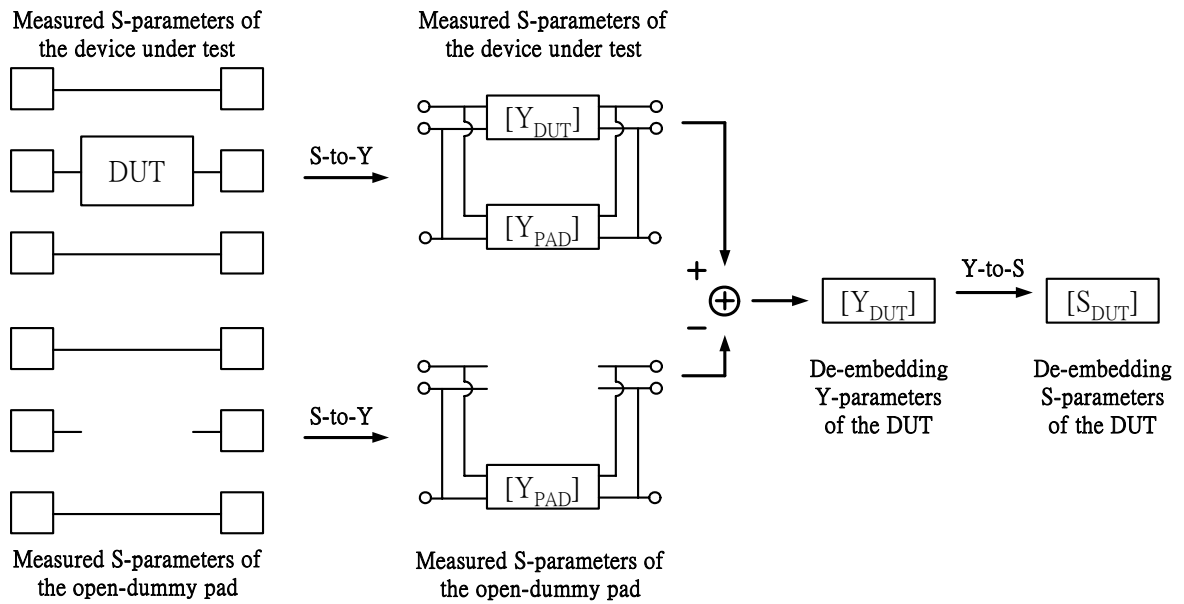


Figure 4.10 The schematics and procedure for illustrating open-pad de-embedding method.

4.4 High frequency characteristics of new symmetric inductors – measurement and EM simulation

For broadband symmetric inductor design, EM simulation was performed to guide layout and geometry optimization for achieving the specified performance target. Following an improved simulation environment set up for HFSS as shown in Fig. 3.4., two categories of broadband inductors, namely quadruple symmetric and quadruple semi-symmetric inductors were designed. Note that EM simulation setup in Fig.3.4. with horizontal mode RF signal injection at top metal (M8) and GR at bottom metal (M1) is a key determining an accurate simulation for very small inductors aimed at broadband design up to 70GHz. Regarding the geometry design, metal trace widths of $W = 6, 9\mu m$ were selected based on an analysis of high frequency series resistances in terms of skin and proximity effects described in previous section. Coil radius of $R = 10, 20, 30\mu m$ were designed in accordance with selected widths to meet the target of inductance and key performance parameters such as Q and f_{SR} .

In the following , EM simulation by HFSS was carried out to make a comparison between measured data after an open de-embedding and the intrinsic characteristics in terms of two-port S-parameters (S_{11}, S_{22}), $L(\omega)$, $\text{Re}(Z_{in}(\omega))$, $\text{Re}(-1/Y_{21})$, and $Q(\omega)$. Note that different EM simulation setups with vertical mode for conventional one and horizontal mode for the new one were specified for a verification. Fig. 4.11 indicates the measured and simulated S-parameters (S_{11}, S_{22}) for a quadruple symmetric inductor with layout in Fig. 4.3 and the smallest dimension of $R=10\mu m$, and $W=6\mu m$ in this design. The key performance parameters $L(\omega)$, $\text{Re}(Z_{in}(\omega))$, $\text{Re}(-1/Y_{21})$, and $Q(\omega)$ derived from S-parameters are presented in Fig. 4.12. The comparison over high frequencies up to 110 GHz reveals a dramatic deviation in HFSS simulation from measured performance parameters ($L(\omega)$, $\text{Re}(Z_{in}(\omega))$, $\text{Re}(-1/Y_{21})$, and $Q(\omega)$) when conventional setup (dash lines)

was employed, even though the mismatch in S-parameters in Fig. 4.11 is not worse than simulated results using a new setup (lines). The severe deviations can be identified as over-estimated $Q(\omega)$ associated with under-estimated $\text{Re}(Z_{in}(\omega))$ and $\text{Re}(-1/Y_{21})$. Referring to HFSS simulation using the improved setup with horizontal mode and GR at M1 in Fig. 4.12, the problem with that of conventional one can be mitigated and the severe deviation is effectively reduced.

Similar results were identified from larger inductors with $R=20, 30 \mu\text{m}$ and W fixed at $6 \mu\text{m}$. Fig. 4.13 and 14 present the results for $R=20 \mu\text{m}$ and $W=6 \mu\text{m}$. As for the inductor with largest $R=30 \mu\text{m}$ and the same width, $W=6 \mu\text{m}$, results are demonstrated in Fig. 4.15 for two-port S-parameters and Fig. 4.16 for four performance parameters. The comparison over various geometries suggests that EM simulation for miniaturized inductors aimed at broadband design is critically sensitive to environmental setup such as RF signal injection mode and GR placement. The improvement realized by the horizontal mode in high frequency performance parameters ($L(\omega)$, $\text{Re}(Z_{in}(\omega))$, $\text{Re}(-1/Y_{21})$, and $Q(\omega)$) makes HFSS simulation useful for small inductor simulation and broadband design.

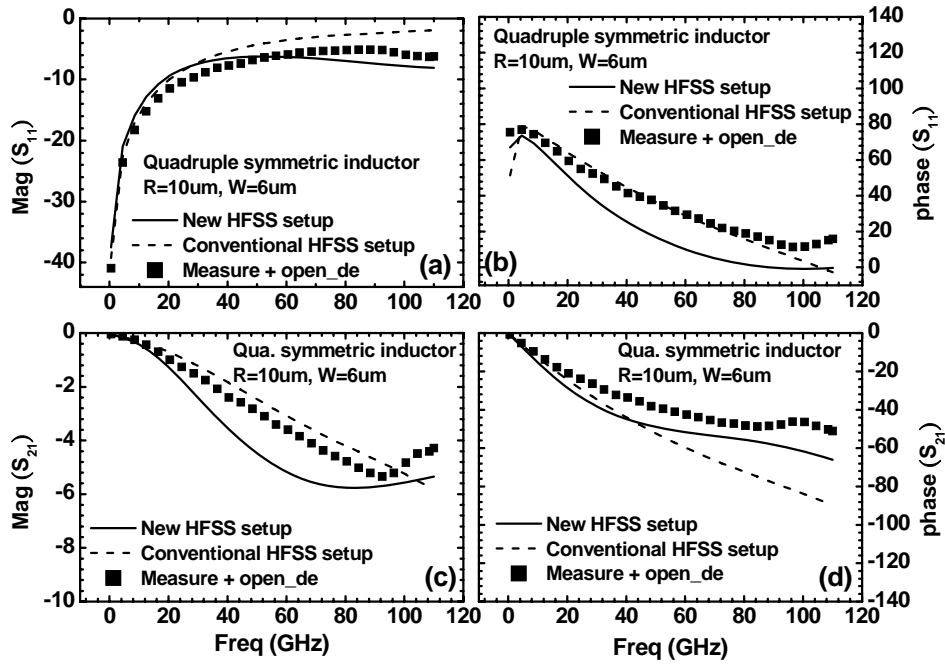


Figure 4.11 Comparison between measurement and HFSS simulation with two conventional (vertical mode) and new (horizontal mode) setups, for a quadruple symmetric inductor with a small dimension of $R=10\mu\text{m}$, $W=6\mu\text{m}$ (a) magnitude(S_{11}) (b) phase(S_{11}) (c) magnitude(S_{21}) (d) phase(S_{21}).

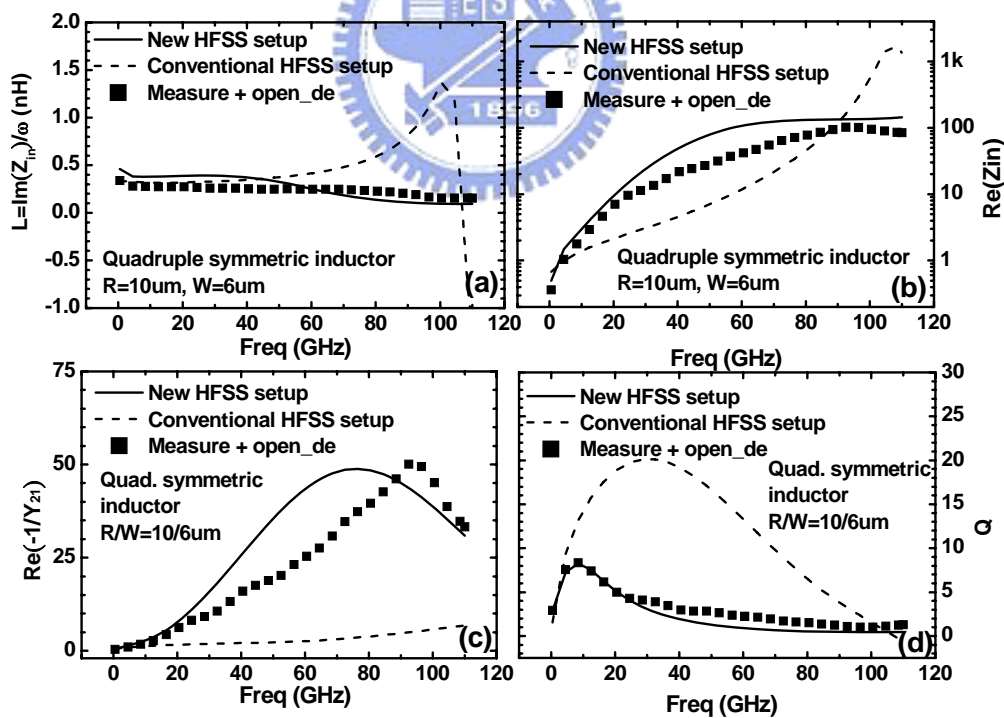


Figure 4.12 Comparison between measurement and HFSS simulation with two conventional (vertical mode) and new (horizontal mode) setups, for a quadruple symmetric inductor with a small dimension of $R=10\mu\text{m}$, $W=6\mu\text{m}$ (a) $L = \text{Im}(Z_{in})/\omega$ (b) $\text{Re}(Z_{in})$ (c) $\text{Re}(-1/Y_{21})$ (d) Q .

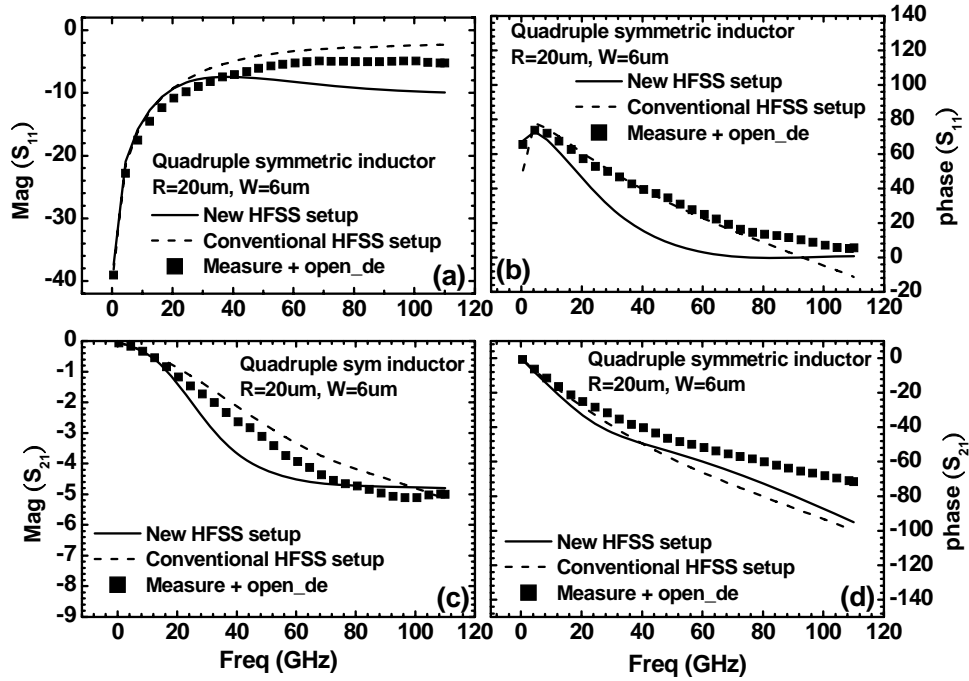


Figure 4.13 Comparison between measurement and HFSS simulation with two conventional (vertical mode) and new (horizontal mode) setups, for a quadruple symmetric inductor with a small dimension of $R=20\mu\text{m}$, $W=6\mu\text{m}$ (a) magnitude(S_{11}) (b) phase(S_{11}) (c) magnitude(S_{21}) (d) phase(S_{21}).

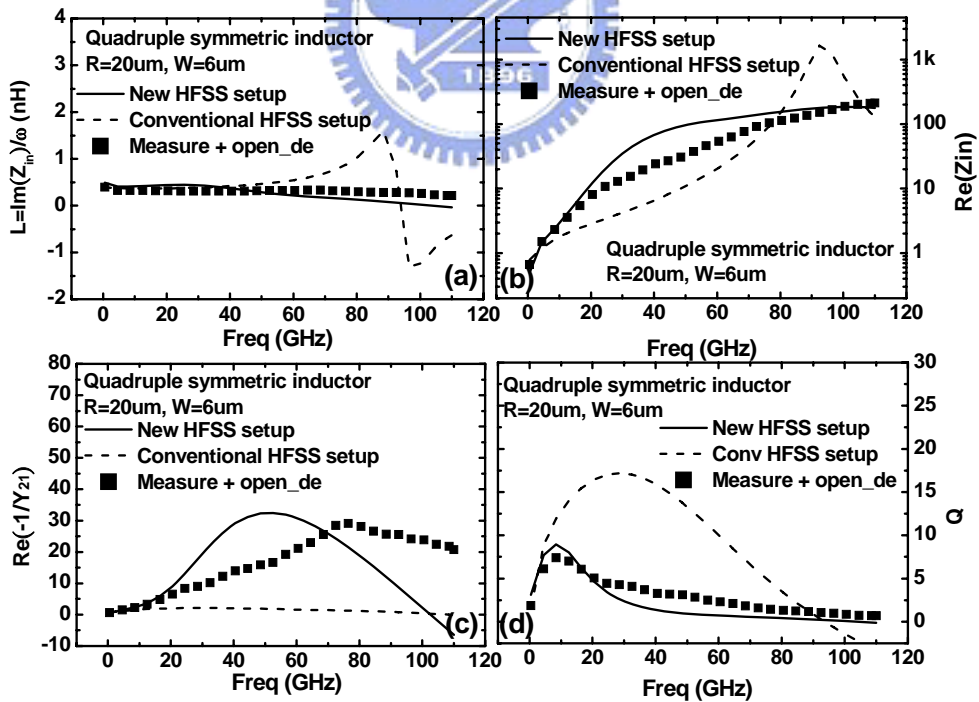


Figure 4.14 Comparison between measurement and HFSS simulation with two conventional (vertical mode) and new (horizontal mode) setups, for a quadruple symmetric inductor with a small dimension of $R=20\mu\text{m}$, $W=6\mu\text{m}$ (a) $L = \text{Im}(Z_{in})/\omega$ (b) $\text{Re}(Z_{in})$ (c) $\text{Re}(-1/Y_{21})$ (d) Q .

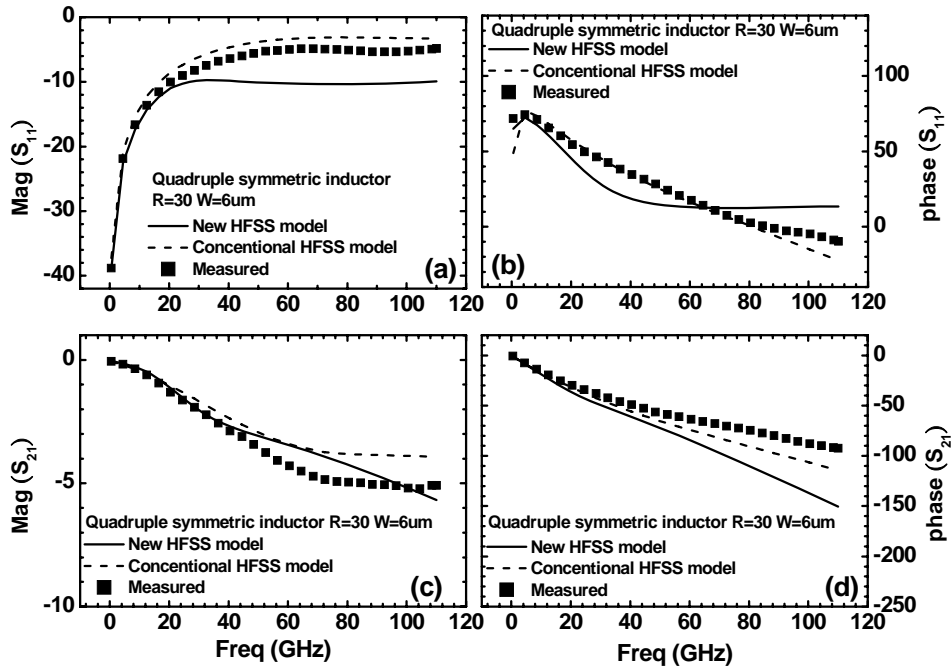


Figure 4.15 Comparison between measurement and HFSS simulation with two conventional (vertical mode) and new (horizontal mode) setups, for a quadruple symmetric inductor with a small dimension of $R=30\mu\text{m}$, $W=6\mu\text{m}$ (a) magnitude(S_{11}) (b) phase(S_{11}) (c) magnitude(S_{21}) (d) phase(S_{21}).

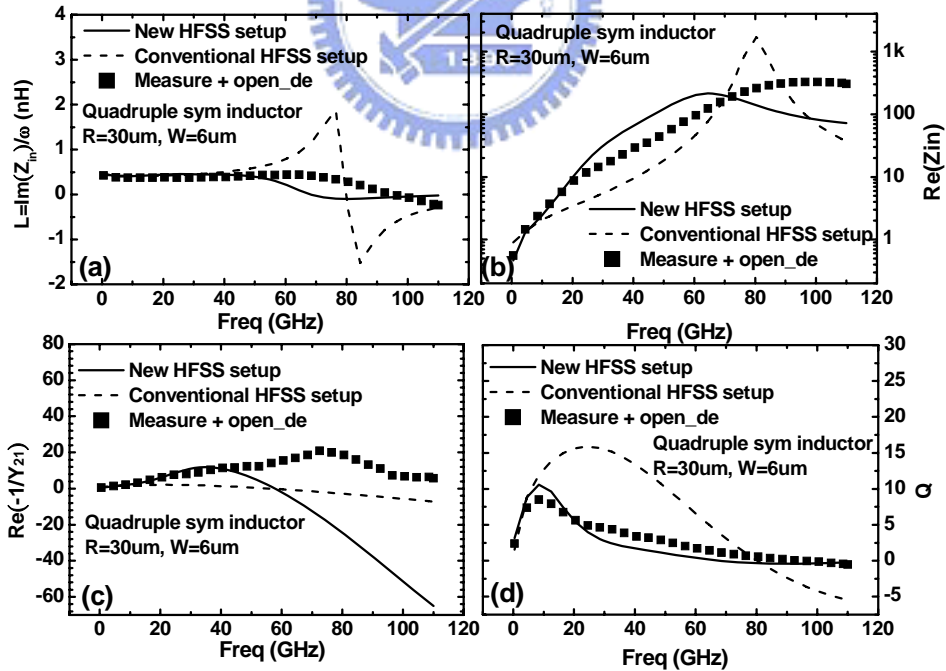


Figure 4.16 Comparison between measurement and HFSS simulation with two conventional (vertical mode) and new (horizontal mode) setups, for a quadruple symmetric inductor with a small dimension of $R=30\mu\text{m}$, $W=6\mu\text{m}$ (a) $L = \text{Im}(Z_{in})/\omega$ (b) $\text{Re}(Z_{in})$ (c) $\text{Re}(-1/Y_{21})$ (d) Q .

4.5 Comparison between new symmetric inductors and conventional symmetric inductors

As mentioned previously, the new symmetric inductors design in this work were aimed at two primary goals. One is broadband and high-Q for ultra-wide band applications and another one is an improved symmetry compared with conventional symmetric inductors. To verify the latter one, conventional symmetric inductors were fabricated together with new symmetric inductors on the same chip for a comparison. Note that the conventional symmetric inductors were designed with the same coil radius and metal trace width as those of new symmetric inductors for a fair comparison in f_{SR} , Q , and other parameters under a similar area estate.

4.5.1 Two-port high frequency parameters under a single-ended excitation

Fig. 4.17 demonstrates two-port S-parameters measured for conventional and new symmetric inductors with $R=30\mu\text{m}$ and $W=6\mu\text{m}$. The comparison reveals an obviously lower frequency for conventional inductor to change phase(S_{21}) from inductive mode to capacitive and suggests the lower f_{SR} for self-resonance. The larger self inductance L_s and parasitic capacitances like $C_{ox1,2}$, C_p , and C_{sub} associated with conventional symmetric inductors are considered the potential factors responsible for the apparently lower resonance frequency. Fig. 4.18 presents high frequency performance parameters $L(\omega)$, $\text{Re}(Z_{in})$, $\text{Re}(-1/Y_{21})$, and $Q(\omega)$ derived from S-parameters. The comparison indicates a larger L_s for conventional symmetric inductors at lower frequency prior to self resonance and change from inductive mode to capacitive mode at around 40 GHz, which corresponds to an occurrence of self resonance. On the other hand, the quadruple symmetric inductor can keep an inductive mode being free from self resonance over very high frequency to near 100 GHz. As a result, quality factor Q can be maintained positive in a broadband region of near 100 GHz for the quadruple symmetric inductor, which is significantly broader than that of conventional inductors, limited to around 40 GHz. In the following

section, equivalent circuit models will be developed for conventional and quadruple symmetric inductors for a comparison in terms of model parameters, f_{SR} , and occupied chip area.

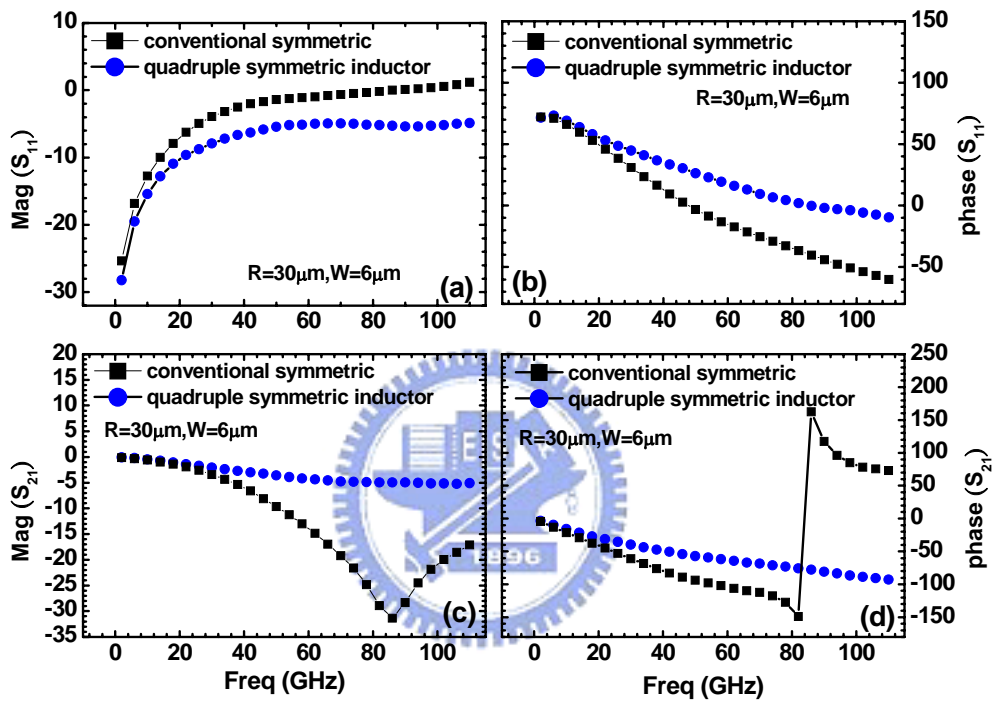


Figure 4.17 Comparison between the conventional and quadruple symmetric inductors in the measured S-parameters over frequencies in 1~110GHz (a) magnitude (S_{11}) (b) phase(S_{11}) (c) magnitude (S_{21}) (d) phase(S_{21}). The coil radius and metal trace width are $R=30\mu\text{m}$ and $W=6\mu\text{m}$ for both conventional and quadruple symmetric inductors.

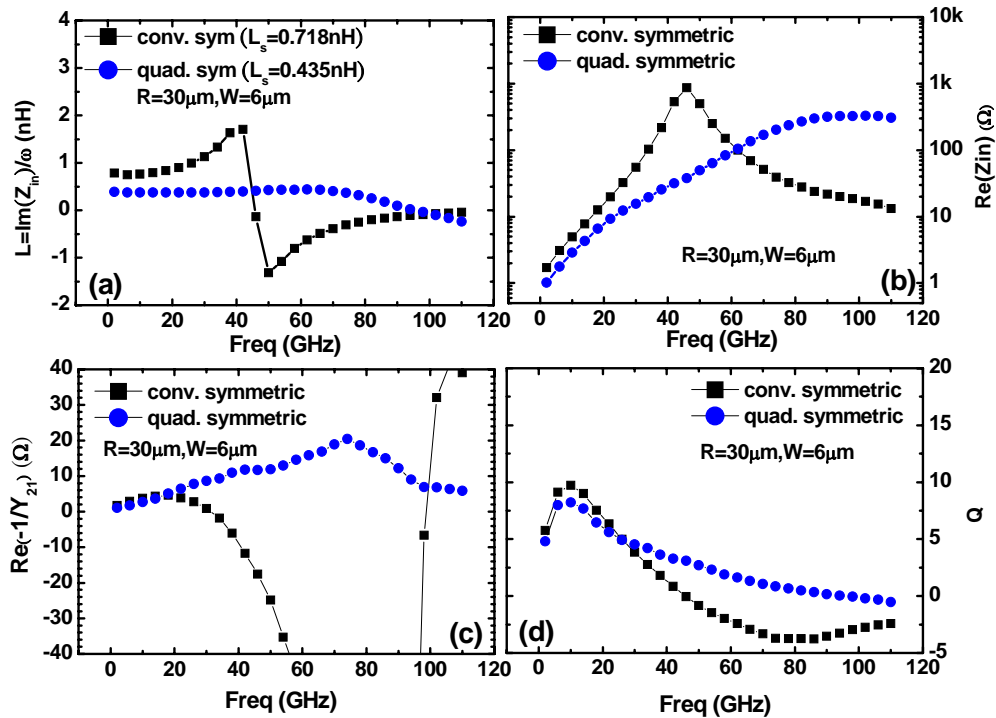


Figure 4.18 Comparison between the conventional and quadruple symmetric inductors in performance parameters derived from S-parameters over frequencies in 1~110GHz (a) $L = \text{Im}(Z_{in})/\omega$ (b) $\text{Re}(Z_{in})$ (c) $\text{Re}(-1/Y_{21})$ (d) Q . The coil radius and metal trace width are $R=30\mu\text{m}$ and $W=6\mu\text{m}$ for both conventional and quadruple symmetric inductors.

4.5.2 Comparison of high frequency performance between single-ended and differential excitations – new and conventional symmetric inductors

According to the theoretical analysis in chapter 2, the advantages provided by a symmetric inductor under a differentially driven operation than that under a single-ended mode operation trigger our motivation in this work for a broadband symmetric inductor design. Fig. 4.19 presents the comparison in input impedance under single-ended and differential excitations, namely Z_{in} and Z_d for quadruple symmetric and conventional symmetric inductors with the same coil radius and metal trace width, $R=30\mu\text{m}$ and $W=6\mu\text{m}$. Both measurement and HFSS simulation indicate an effective suppression of $\text{Re}(Z_d)$ under a differential excitation than $\text{Re}(Z_{in})$ under a single-ended excitation, over increasing frequency. Regarding the imaginary part of input impedance and the represented frequency dependent inductance ($L(\omega) = \text{Im}(Z_{in})/\omega$), the differential mode

operation can help extend the change of inductive mode to capacitive mode impedances due to self resonance to an apparently higher frequency. The lower $\text{Re}(Z_d)$ than $\text{Re}(Z_{in})$ and retarded change to capacitive mode in $\text{Im}(Z_d)$ compared to $\text{Im}(Z_{in})$ suggest that differential operation can improve Q as well as f_{SR} , and offer advantages in broadband design. Both quadruple symmetric and conventional symmetric inductors indicate similar results in Fig. 4.19(a),(b) and Fig. 4.19(c),(d) respectively, but quadruple symmetric inductors in our design exhibit an obviously broader bandwidth over the change of impedance mode. Note that HFSS simulation demonstrates a similar trend but reveals a significant deviation from the measurement.

Fig. 4.20 presents the quality factor Q_{se} under a single-ended excitation and Q_d under a differential excitation. For quadruple symmetric inductors shown in Fig. 4.20(a), Q_d keeps nearly identical with Q_{se} at lower frequency below what corresponding to maximal Q (Q_{max}), denoted as f_{max} , and becomes significantly higher than Q_{se} at higher frequency above f_{max} . Regarding the self-resonance frequency f_{SR} corresponding to zero Q , the differential mode can escalate f_{SR} from around 96 GHz to above 110 GHz (limitation of measurement in VNA). As for conventional symmetric inductors illustrated in Fig. 4.20(b), similar trend was demonstrated in Q_d enhancement over Q_{se} and higher f_{SR} under a differential mode operation. Note that f_{SR} for conventional symmetric inductors is raised from 45 GHz for a single-ended excitation to 60 GHz for a differential excitation, that are around two times lower than those of quadruple symmetric inductors with the same R and W . Again, HFSS simulation can predict mentioned high frequency performance parameters (Z_{in} , Z_d , Q_{se} , Q_d , f_{SR}) with a close match with measurement for conventional symmetric inductors, but suffers significant deviation from measurement for quadruple symmetric inductors.

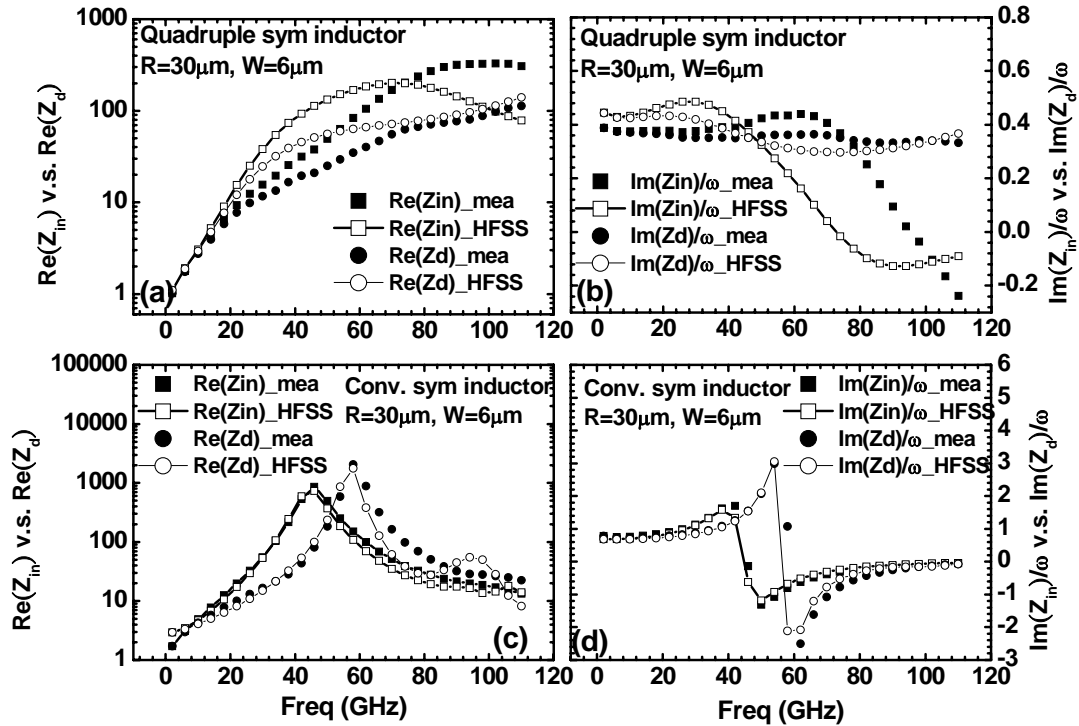


Figure 4.19 Comparison of Z_{in} under a single-ended excitation and Z_d under a differential excitation from measurement and HFSS simulation (a) $Re(Z_{in})$ and $Re(Z_d)$ (b) $Im(Z_{in})/\omega$ and $Im(Z_d)/\omega$ for quadruple symmetric inductors (c) $Re(Z_{in})$ and $Re(Z_d)$ (d) $Im(Z_{in})/\omega$ and $Im(Z_d)/\omega$ for conventional symmetric inductors. The coil radius and metal trace width are $R=30\mu m$ and $W=6\mu m$ for both conventional and quadruple symmetric inductors.

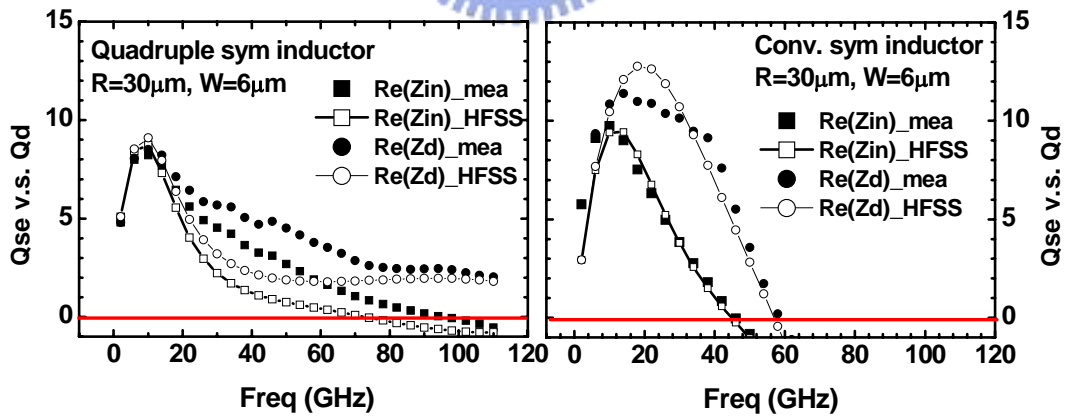


Figure 4.20 Comparison of Q_{se} under a single-ended excitation and Q_d under a differential excitation from measurement and HFSS simulation (a) Q_{se} and Q_d for quadruple symmetric inductors (b) Q_{se} and Q_d for conventional symmetric inductors. The coil radius and metal trace width are $R=30\mu m$ and $W=6\mu m$ for both conventional and quadruple symmetric inductors.

4.6 Enhanced T-model - the equivalent circuit and model parameters

An equivalent circuit model, namely enhanced T-model was developed for the new symmetric inductors, i.e. quadruple symmetric and semi-symmetric inductors in this design. The enhanced T-model is composed of two primary RLC networks corresponding to spiral coils and silicon substrate underneath, which play a key role responsible for the conductor loss and substrate loss respectively. Note that accurate simulation of energy losses in conducting coils and semi-conducting substrate is indispensable for achieving broadband accuracy aimed for an on-chip inductors, particularly for broadband up to 70 GHz and beyond in this work.

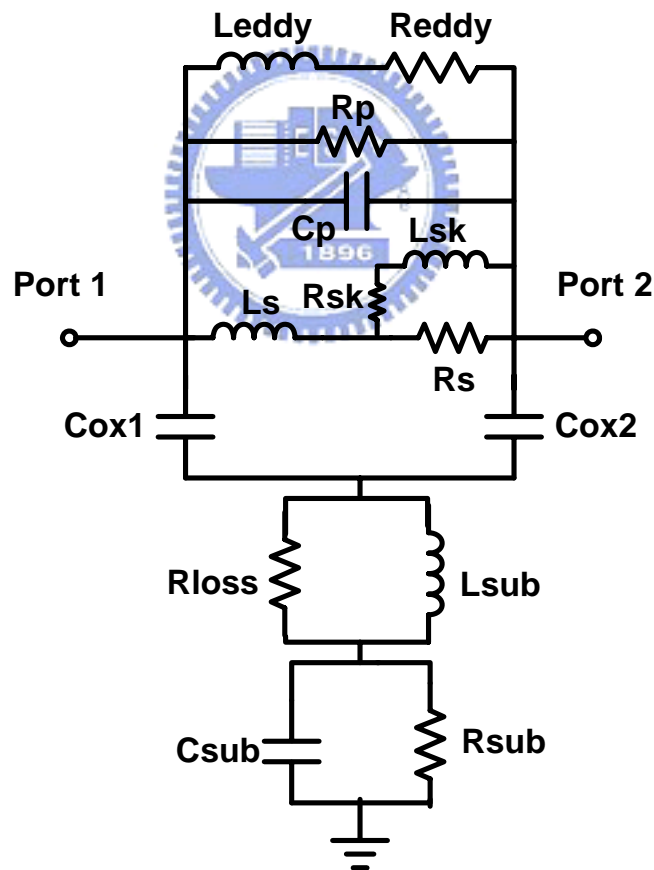


Figure 4.21 The enhanced T-model for on-chip quadruple symmetric and semi-symmetric inductors.

Figure 4.21 illustrates the circuit schematics of our proposed enhanced T-model for small inductors, in which two primary RLC networks are linked through C_{ox1} and C_{ox2} to simulate the coupling between the spiral coils and lossy substrate underneath. First, the physical property of each element in the enhanced T-model will be defined as follows. In RLC network above $C_{ox1(2)}$ accounting for spiral coils, R_S and L_S represent the series resistance and inductance in metal coils at sufficiently low frequency. Considering skin effect apparent in conductors at higher frequency, a series RL denoted as R_{sk} and L_{sk} were implemented in parallel with R_S and then in series with L_S . For model simplicity, a single $R_{sk}L_{sk}$ branch was employed for simulating surface layer resistance and inductance. Provided that more ladder branches were adopted, the skin effect can be accurately modeled over a broader bandwidth. In addition to skin effect, proximity effect may become even more dominant at very high frequency of our focus going above 70 GHz in this design. Then one more series RL, namely R_{eddy} and L_{eddy} were created in parallel with the series $R_S L_S$ and parallel $R_p C_p$ to simulate the proximity effect due to EM field coupling between adjacent coils, and the resulted current re-distribution as well as increase of resistance at higher frequency. Herein, R_p represents the coils' conductor loss originated from lossy substrate return path and C_p accounts for a feedforward capacitance due to line-to-line coupling between port-1 and port-2. As a result, the spiral coil network is composed of totally 8 elements, such as R_S , L_S , R_{sk} , L_{sk} , R_{eddy} , L_{eddy} , R_p , and C_p . Note that all the RLC elements are independent of frequency to ensure computation efficiency and scalability over various dimensions of the inductors.

As for substrate RLC network below $C_{ox1(2)}$, there are four elements, namely R_{sub} , C_{sub} , L_{sub} and R_{loss} adopted in the enhanced T-model. R_{sub} and C_{sub} represent the lossy substrate resistance and capacitance. L_{sub} and R_{loss} were implemented to simulate eddy current induced substrate loss in which L_{sub} accounts for the reactive power loss crossing the substrate, and R_{loss} is responsible for the resistive loss or joule heat dissipation.

4.7 Enhanced T-model model simulation results and comparison with measurement for new symmetric inductors

The broadband accuracy and scalability of the enhanced T-model parameters have been verified and will be presented in this section. Besides, the improvement of Q and f_{SR} realized by differential topology compared with the single-end counterpart will be analyzed through our enhanced T-model equivalent circuit analysis.

4.7.1 Broadband Accuracy of the Enhanced T-model and Guideline for Broadband On-chip Inductor Design

Table 4.2 summarized the enhanced T-model parameters extracted for quadruple symmetric and semi-symmetric inductors with fixed width at $W=6\mu\text{m}$ and various R of 10, 20, 30 μm . The self-resonance frequencies f_{SR} calculated by an analytical model developed in our previous work [18] given by (4.1) are provided for all inductors with various R as one of the most important performance parameters for broadband design. For both kinds of inductors, the larger R leads to the lower f_{SR} due to larger L_S and larger parasitic capacitances, such as C_p , C_{ox1} , C_{ox2} , and C_{sub} . The comparison between two kinds of inductors reveals an important result that quadruple symmetric inductors can provide high f_{SR} , attributed to smaller parasitic capacitances like C_{ox1} , C_{ox2} , and C_{sub} associated with every specified R .

Table 4.2 Enhanced T-model parameters for quadruple symmetric and quadruple semi-symmetric inductors with W=6μm and R= 10, 20, 30 μm.

New inductors		Quad. Sym. inductors			Quad. Semi-sym. inductors		
Metal trace width		W=6 μm			W=6 μm		
R	μm	10	20	30	10	20	30
L _S	nH	0.3376	0.3674	0.42	0.325	0.4023	0.469
R _S	Ω	0.395	0.573	0.693	0.524	0.638	0.732
L _{SK}	nH	0.855	0.7303	0.53	0.878	0.755	0.554
R _{SK}	Ω	0.259	0.4028	0.6188	0.2626	0.4256	0.6314
L _{eddy}	nH	1.622	2.207	3.303	1.01	1.96	3.03
R _{eddy}	Ω	24.35	63.808	85.5	34.38	67.2	87.6
R _P	Ω	281.99	404.72	440.17	386.72	437.62	460.43
C _P	fF	0.393	0.393	0.393	0.393	0.393	0.393
C _{OX1}	fF	3.04	5.12	9.3	4.16	7.42	10.95
C _{OX2}	fF	3.04	5.12	9.3	4.16	7.42	10.95
R _{loss}	Ω	218.41	260.39	327.15	230.876	269.66	328.305
R _{sub}	Ω	647.81	568.16	456.52	614.629	564.54	432.69
L _{sub}	nH	0.151	0.171	0.195	0.1638	0.1749	0.1865
C _{sub}	fF	9.123	12.05	15.13	10.003	18.326	22.87
f _{SR}	GHz	162.97	126.08	91.98	146.96	101.16	78.95

$$f_{SR} = \frac{1}{2\pi} \sqrt{\frac{1}{L_s} \times \left(\frac{C_{ox1} + C_{ox2} + C_{sub}}{C_p (C_{ox1} + C_{ox2} + C_{sub}) + C_{ox1} (C_{sub} + C_{ox2})} \right)} \quad (4.1)$$

In the following, the simulation by enhanced T-model and comparison with measured data over ultra wide band will be presented. First, Fig. 4.22 presents two-port S-parameters for the quadruple symmetric inductor with R=10μm and W=6μm in which a good agreement between enhanced T-model and measurement is realized for S₁₁ in both magnitude and phase over very broad frequencies up to 110 GHz. Regarding S₂₁, good match is achieved for phase(S₂₁) up to 40 GHz but worse deviation is suffered by mag.(S₂₁) at frequencies above 20 GHz. The true mechanisms underlying the deviation in S₂₁ is not well understood at current stage. The results suggest that some intrinsic problems in conventional de-embedding and method and equivalent circuit model may be

responsible for the deviation. Further effort is required through future works for necessary improvement. Based on two-port S-parameters, key performance parameters, such as $L=\text{Im}(Z_{in})/\omega$, $\text{Re}(Z_{in})$, $\text{Re}(-1/Y_{21})$, and Q can be derived for a rigorous verification on inductor performance over a broad range of frequencies and the accuracy of enhanced T-model for simulating high frequency characteristics for broadband inductors on Si substrate. The results shown in Fig. 4.23 for quadruple symmetric inductor with mentioned dimensions ($R=10\mu\text{m}$ and $W=6\mu\text{m}$) indicate a good agreement in $L=\text{Im}(Z_{in})/\omega$, $\text{Re}(Z_{in})$, and Q but reveal an obvious deviation in $\text{Re}(-1/Y_{21})$ at higher frequencies above 20 GHz. It is believe that the mismatch in $\text{Re}(-1/Y_{21})$ is correlated with that in S_{21} and comes from the same origin. Further effort will be put in future work for understanding the mechanism and improvement solutions. Similar results were measured from larger inductors in the category of quadruple symmetric inductors, with the same layout and width ($W=6\mu\text{m}$) but larger radius of $R=20$ and $30\mu\text{m}$. Fig. 4.24 presents S_{11} and S_{21} for $R=20\mu\text{m}$ and Fig. 4.25 illustrates the corresponding results of $L=\text{Im}(Z_{in})/\omega$, $\text{Re}(Z_{in})$, $\text{Re}(-1/Y_{21})$, and Q . As for $R=30\mu\text{m}$, the largest one among the splits, two-port S-parameters are demonstrated in Fig. 4.26 and four key performance parameters depicted in Fig. 4.27. Note that the larger R leads to lower frequency for self-resonance featured by a fall-off in $L(\omega)$ and zero Q .

As for the second category of inductors, namely quadruple semi-symmetric inductors, two-port S-parameters are shown in Fig. 4.28, 4.30, and 4.32 for different dimensions of $R=10$, 20 , and $30\mu\text{m}$ respectively. Fig. 4.29, 4.31, and 4.33 present the results of $L=\text{Im}(Z_{in})/\omega$, $\text{Re}(Z_{in})$, $\text{Re}(-1/Y_{21})$, and Q corresponding to the splits of R . Note that the larger R leads to the larger inductance near DC condition (very low frequency) and the larger Q_{max} to certain extent. This trend applies to both categories of inductors – quadruple symmetric and semi-symmetric inductors. Note that both kinds of inductors with different layouts can realize ultra-high f_{SR} above 80 GHz for all dimensions ($R=10$, 20 , $30\mu\text{m}$.)

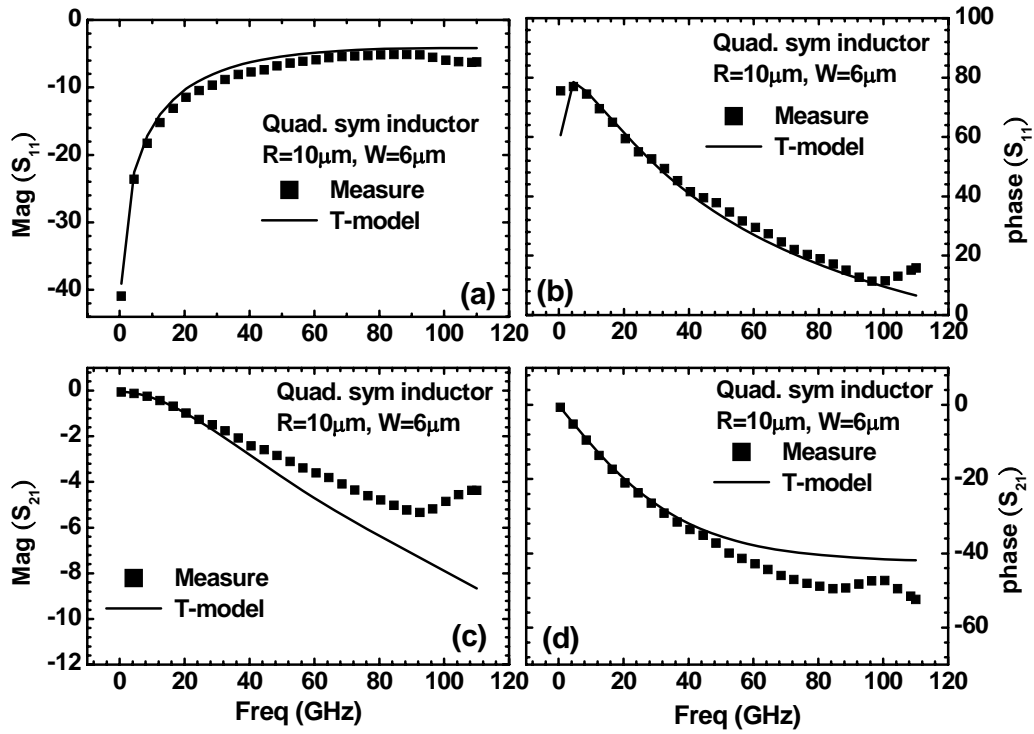


Figure 4.22 Comparison of S_{11} and S_{21} between measurement and simulation by enhanced T-model for quadruple symmetric inductor with $R=10$ and $W=6\mu\text{m}$ (a) $\text{Mag}(S_{11})$ (b) $\text{Phase}(S_{11})$ (c) $\text{Mag}(S_{21})$ (d) $\text{Phase}(S_{21})$.

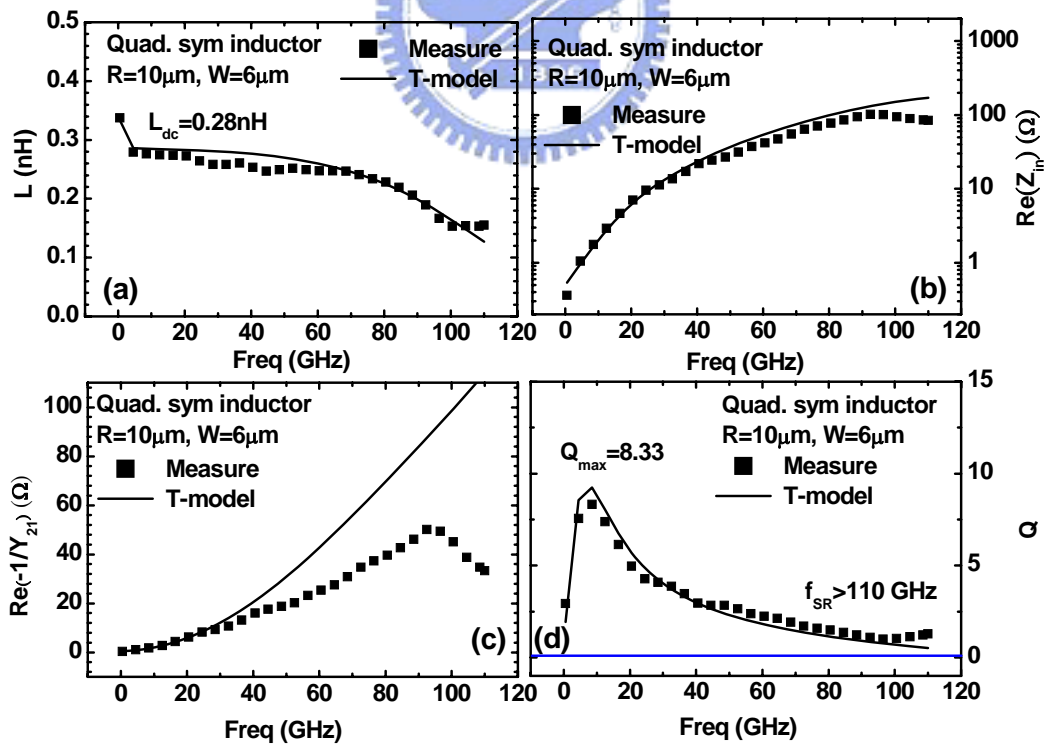


Figure 4.23 Comparison of high frequency impedances and Q between measurement and simulation by enhanced T-model for quadruple symmetric inductor, $R=10$, $W=6\mu\text{m}$ (a) $L=\text{Im}(Z_{in})/\omega$ (b) $\text{Re}(Z_{in})$ (c) $\text{Re}(-1/Y_{21})$ (d) Q .

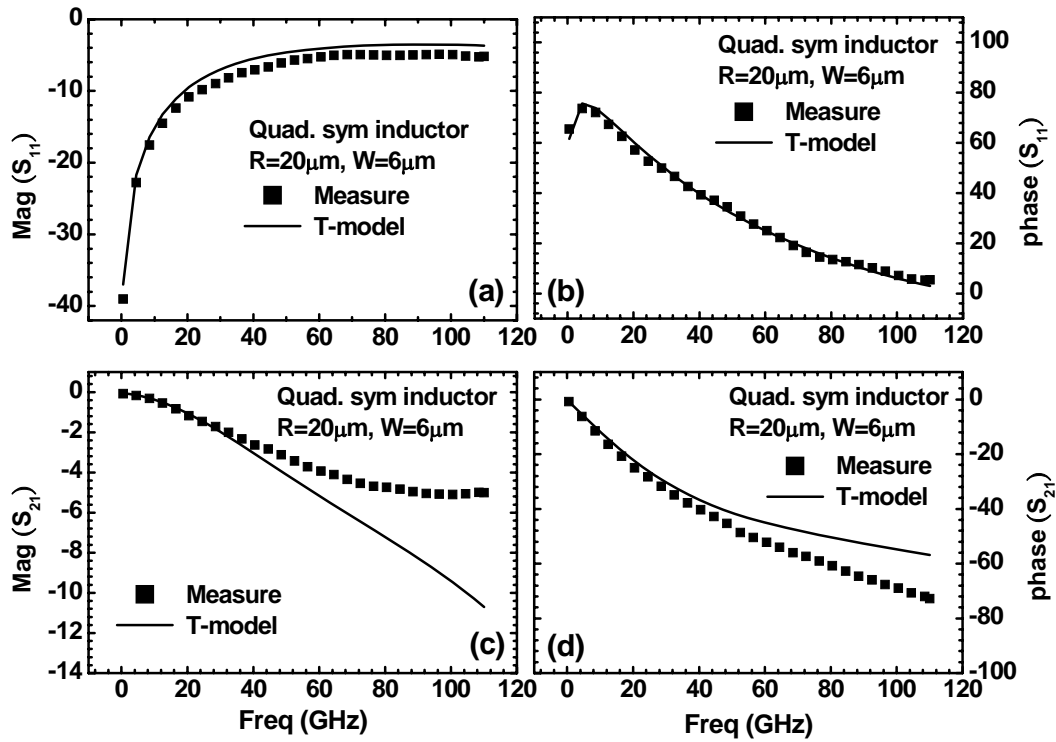


Figure 4.24 Comparison of S_{11} and S_{21} between measurement and simulation by enhanced T-model for quadruple symmetric inductor with $R=20\mu\text{m}$ and $W=6\mu\text{m}$ (a) $\text{Mag}(S_{11})$ (b) $\text{Phase}(S_{11})$ (c) $\text{Mag}(S_{21})$ (d) $\text{Phase}(S_{21})$.

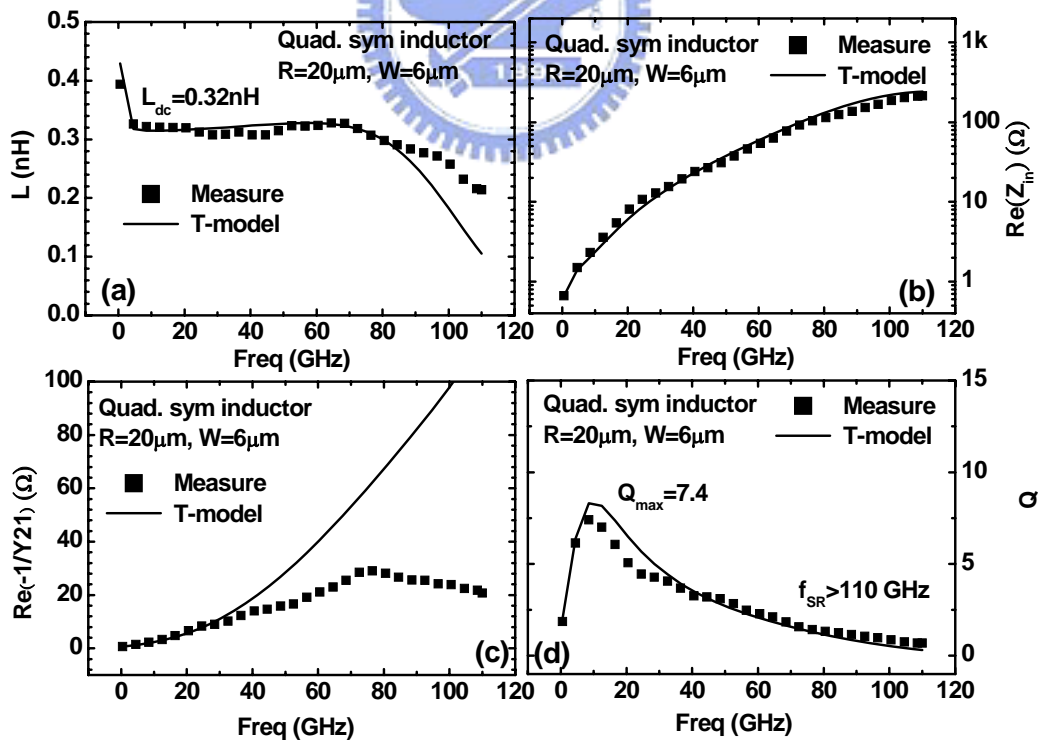


Figure 4.25 Comparison of high frequency impedances and Q between measurement and simulation by enhanced T-model for quadruple symmetric inductor, $R=20\mu\text{m}$, $W=6\mu\text{m}$ (a) $L=\text{Im}(Z_{in})/\omega$ (b) $\text{Re}(Z_{in})$ (c) $\text{Re}(-1/Y_{21})$ (d) Q .

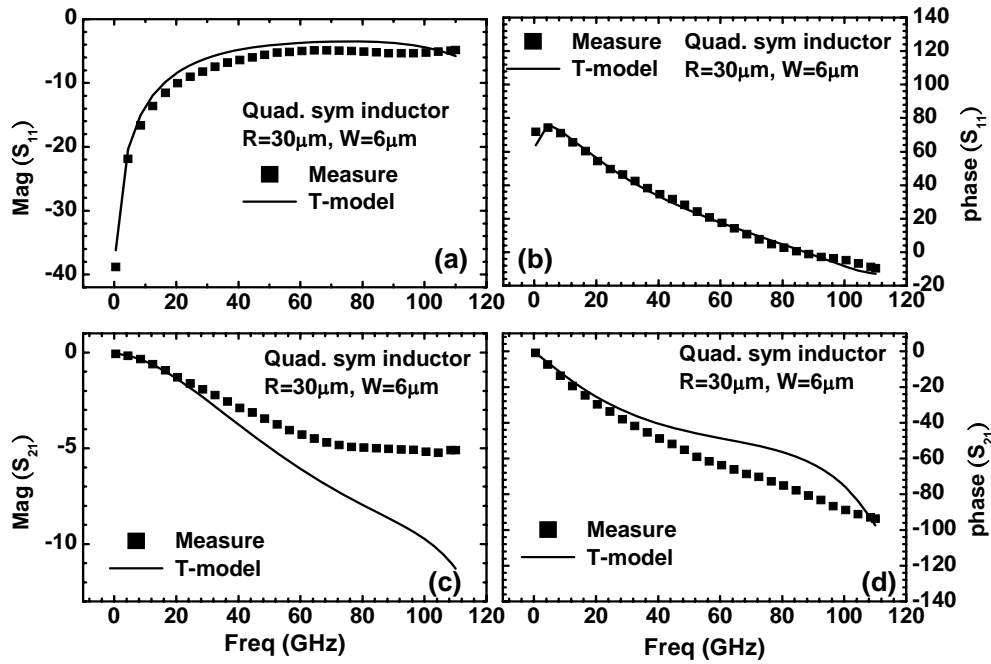


Figure 4.26 Comparison of S_{11} and S_{21} between measurement and simulation by enhanced T-model for quadruple symmetric inductor with $R=30\mu\text{m}$ and $W=6\mu\text{m}$ (a) $\text{Mag}(S_{11})$ (b) $\text{Phase}(S_{11})$ (c) $\text{Mag}(S_{21})$ (d) $\text{Phase}(S_{21})$.

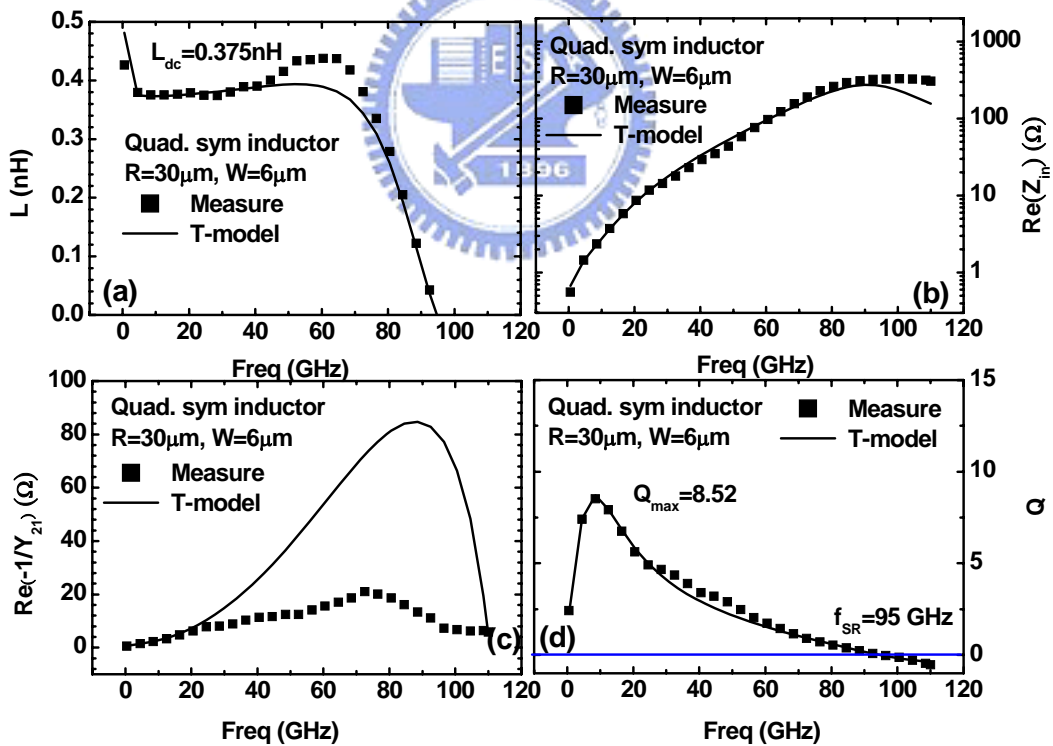


Figure 4.27 Comparison of high frequency impedances and Q between measurement and simulation by enhanced T-model for quadruple symmetric inductor, $R=30\mu\text{m}$, $W=6\mu\text{m}$ (a) $L=\text{Im}(Z_{in})/\omega$ (b) $\text{Re}(Z_{in})$ (c) $\text{Re}(-1/Y_{21})$ (d) Q .

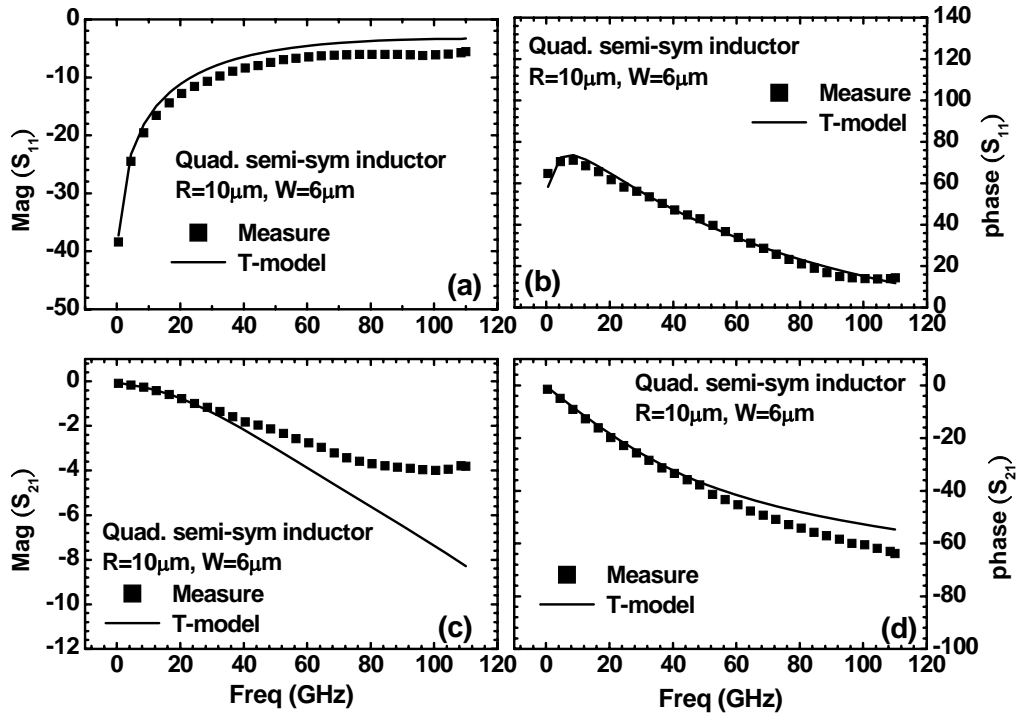


Figure 4.28 Comparison of S_{11} and S_{21} between measurement and simulation by enhanced T-model for quadruple semi-symmetric inductor with $R=10$ and $W=6\mu\text{m}$ (a) $\text{Mag}(S_{11})$ (b) $\text{Phase}(S_{11})$ (c) $\text{Mag}(S_{21})$ (d) $\text{Phase}(S_{21})$.

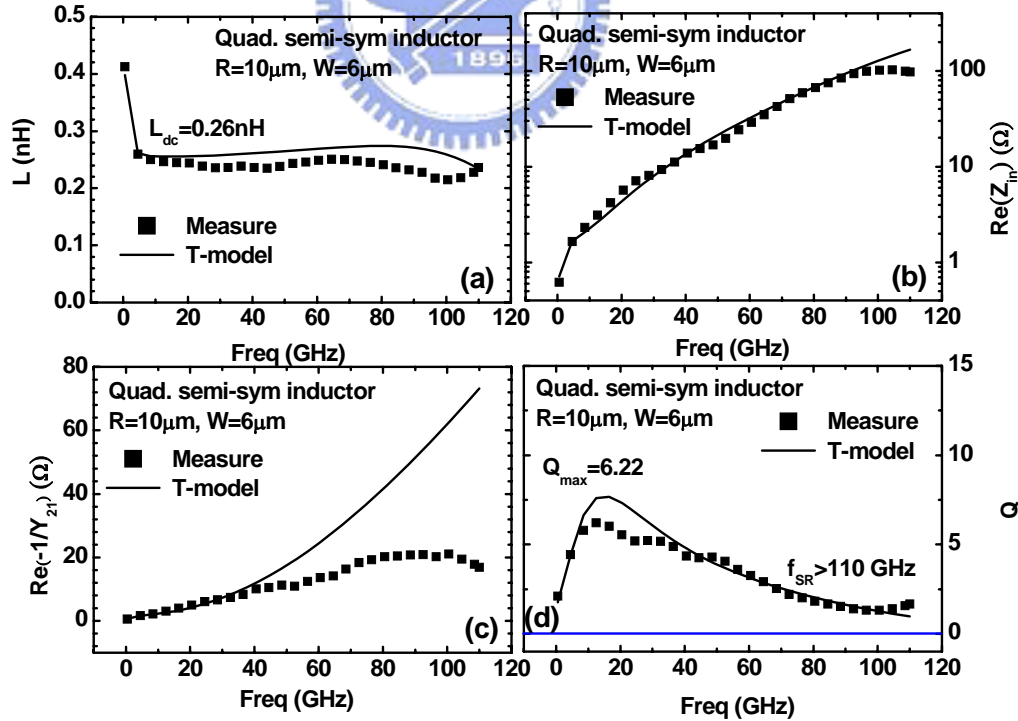


Figure 4.29 Comparison of high frequency impedances and Q between measurement and simulation by enhanced T-model for quadruple semi-symmetric inductor, $R=10$, $W=6\mu\text{m}$ (a) $L = \text{Im}(Z_{in})/\omega$ (b) $\text{Re}(Z_{in})$ (c) $\text{Re}(-1/Y_{21})$ (d) Q .

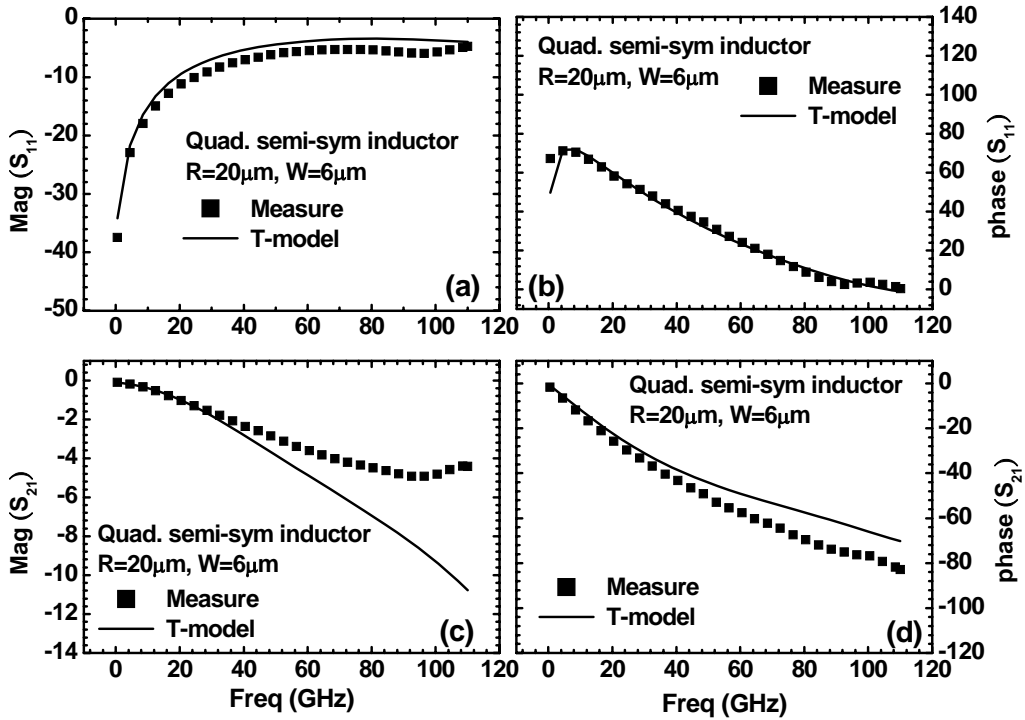


Figure 4.30 Comparison of S_{11} and S_{21} between measurement and simulation by enhanced T-model for quadruple semi-symmetric inductor with $R=20$ and $W=6\mu\text{m}$ (a) $\text{Mag}(S_{11})$ (b) $\text{Phase}(S_{11})$ (c) $\text{Mag}(S_{21})$ (d) $\text{Phase}(S_{21})$.

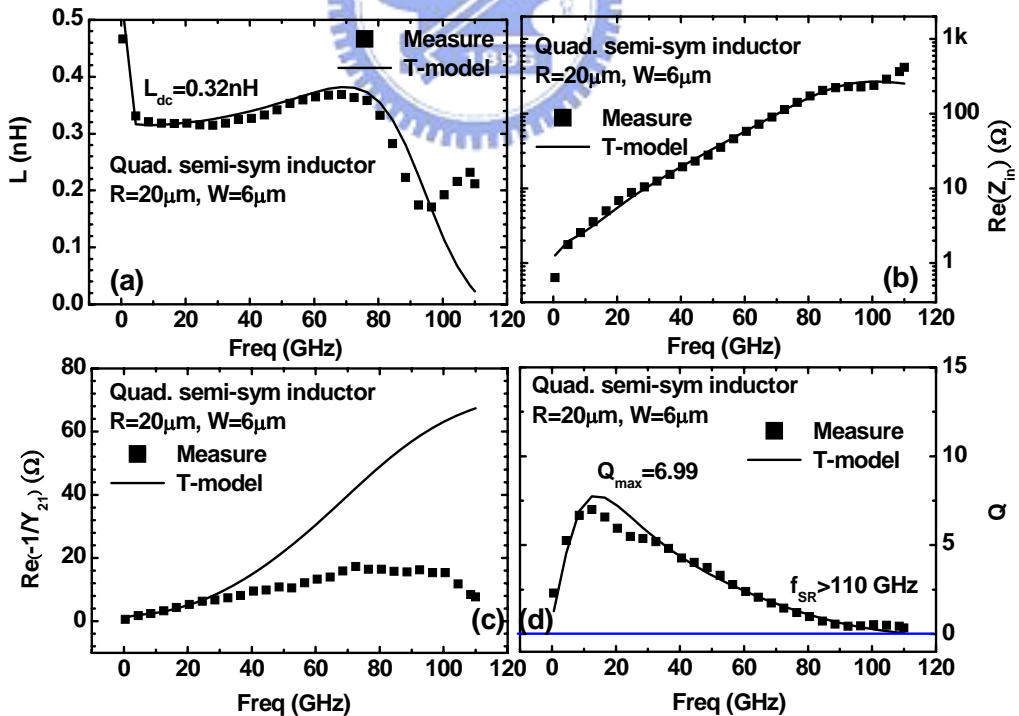


Figure 4.31 Comparison of high frequency impedances and Q between measurement and simulation by enhanced T-model for quadruple semi-symmetric inductor, $R=20$, $W=6\mu\text{m}$ (a) $L = \text{Im}(Z_{in})/\omega$ (b) $\text{Re}(Z_{in})$ (c) $\text{Re}(-1/Y_{21})$ (d) Q .

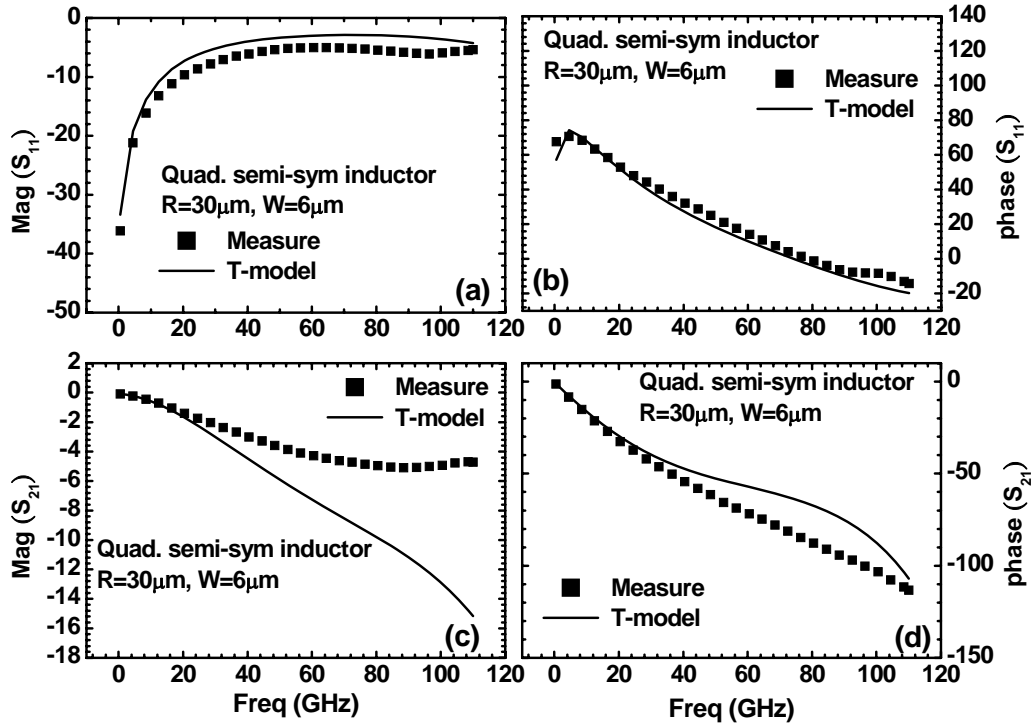


Figure 4.32 Comparison of S_{11} and S_{21} between measurement and simulation by enhanced T-model for quadruple semi-symmetric inductor with $R=30$ and $W=6\mu\text{m}$ (a) $\text{Mag}(S_{11})$ (b) $\text{Phase}(S_{11})$ (c) $\text{Mag}(S_{21})$ (d) $\text{Phase}(S_{21})$.

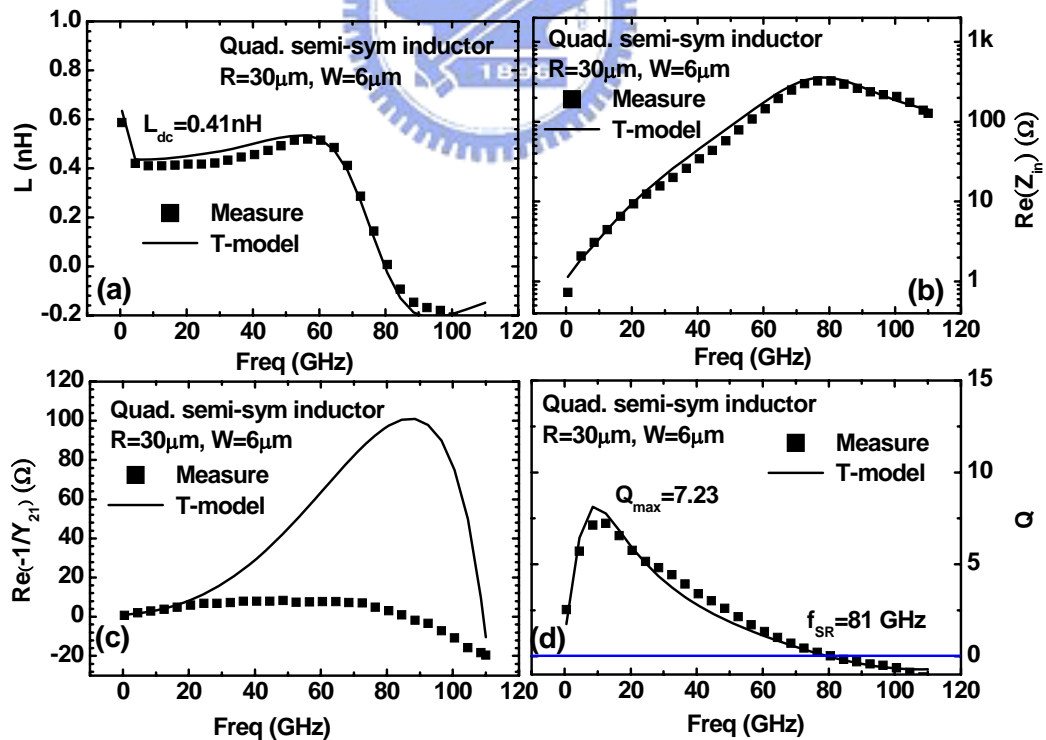


Figure 4.33 Comparison of high frequency impedances and Q between measurement and simulation by enhanced T-model for quadruple semi-symmetric inductor, $R=30$, $W=6\mu\text{m}$ (a) $L = \text{Im}(Z_{in})/\omega$ (b) $\text{Re}(Z_{in})$ (c) $\text{Re}(-1/Y_{21})$ (d) Q .

4.7.2 Scalability of the Enhanced T-model

Beside broadband accuracy, the scalability of an equivalent circuit model is one more important feature, which can facilitate an optimal design through circuit simulation. The scalability of the enhanced T-model is verified over inductors with various coil radii, $R=10, 20, 30 \mu\text{m}$. Fig. 4.34 presents four elements in the spiral coil network, L_s , R_s , R_p , and C_p as well as coil to substrate coupling capacitance C_{ox} versus the coil radius. All the model parameters except C_p follow a linearly increasing function of R . C_p keeps a constant independent of R . Regarding the remaining elements in spiral coil network responsible for skin effect and proximity effect, R_{sk} , L_{eddy} , and R_{eddy} present a linearly increasing function of R while L_{sk} reveals an opposite trend, i.e. a linearly decreasing function, as shown in Fig. 4.35. As for model parameters associated with the substrate network, all of them except R_{sub} , i.e. L_{sub} , R_{loss} , and C_{sub} , match a linearly increasing function of R , shown in Fig. 4.36. Note that $1/R_{sub}$ rather than R_{sub} follows a linear function increasing with R . The smaller R_{sub} corresponding to the larger coil radius R accounts for the worse substrate loss. The aforementioned results demonstrated in Fig. 4.34-4.36 are for quadruple symmetric inductors. Regarding quadruple semi-symmetric inductors, a similar trend is measured and presented in Fig. 4.37-4.38 for spiral coil networks' elements and Fig. 4.39 for substrate network elements.

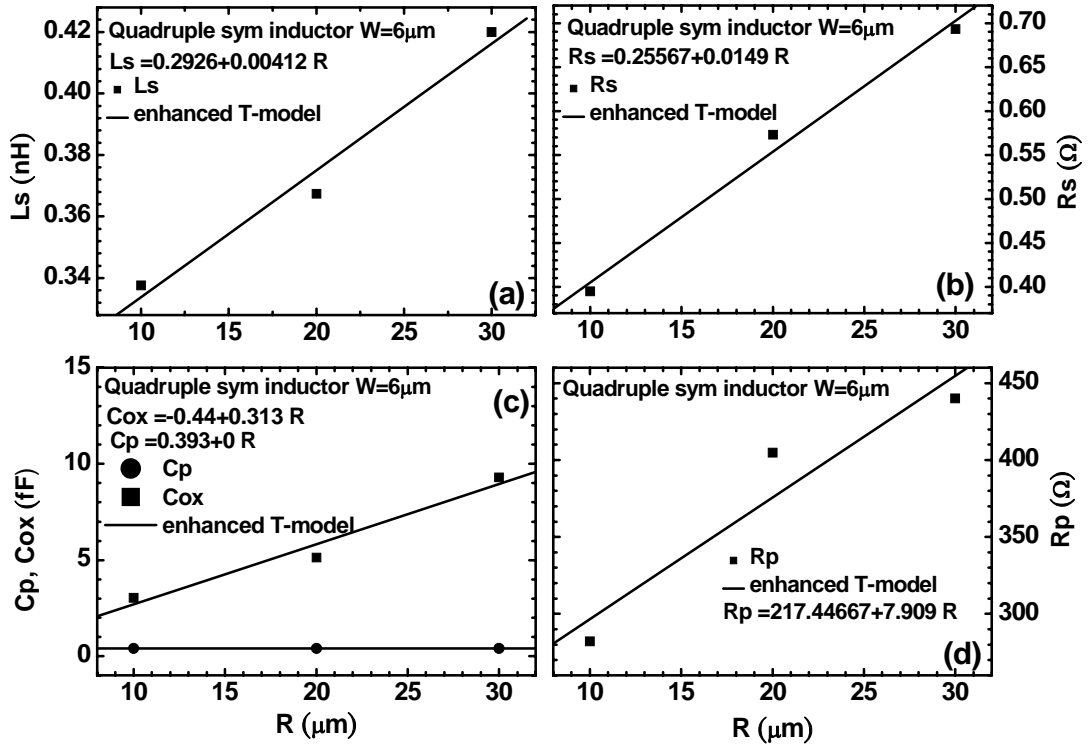


Figure 4.34 Enhanced T-model parameters for quadruple symmetric inductors. Spiral coil RLC network parameters versus radius (a) L_s (b) R_s (c) C_p and C_{ox} (d) R_p .

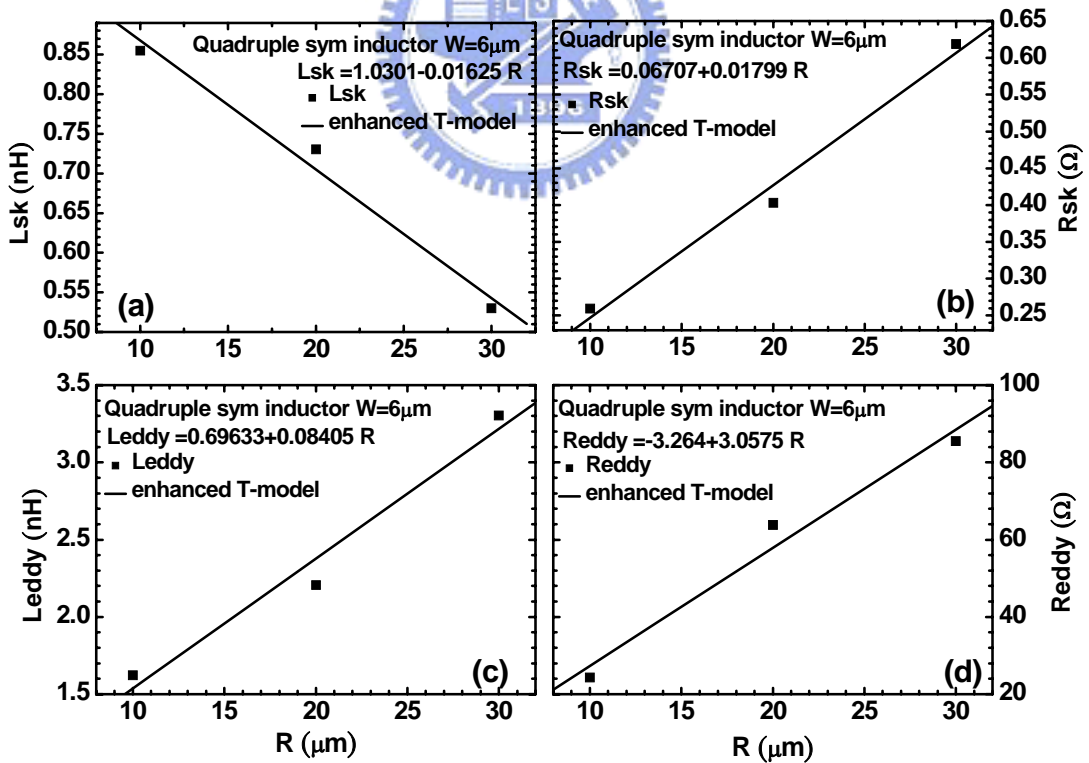


Figure 4.35 Enhanced T-model parameters for quadruple symmetric inductors. Skin effect and proximity effect parameters versus radius (a) L_{sk} (b) R_{sk} (c) L_{eddy} (d) R_{eddy} , in spiral coil network.

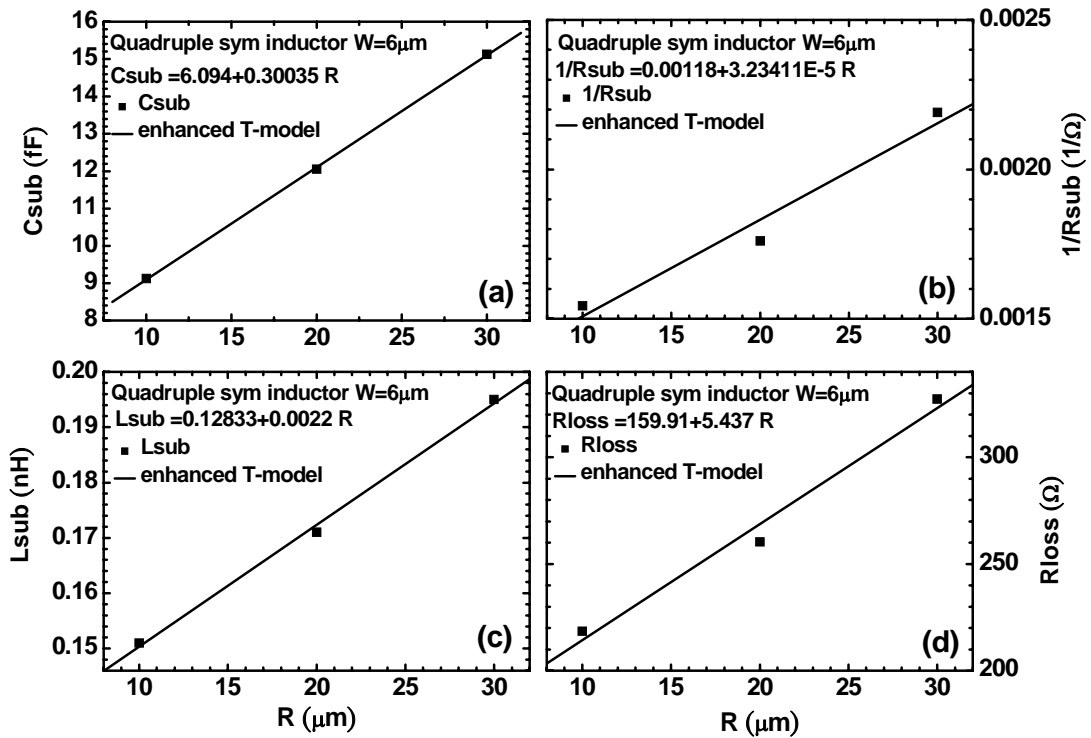


Figure 4.36 Enhanced T-model parameters for quadruple symmetric inductors. Substrate RLC network parameters versus radius (a) C_{sub} (b) $1/R_{\text{sub}}$ (c) L_{sub} (d) R_{loss} .

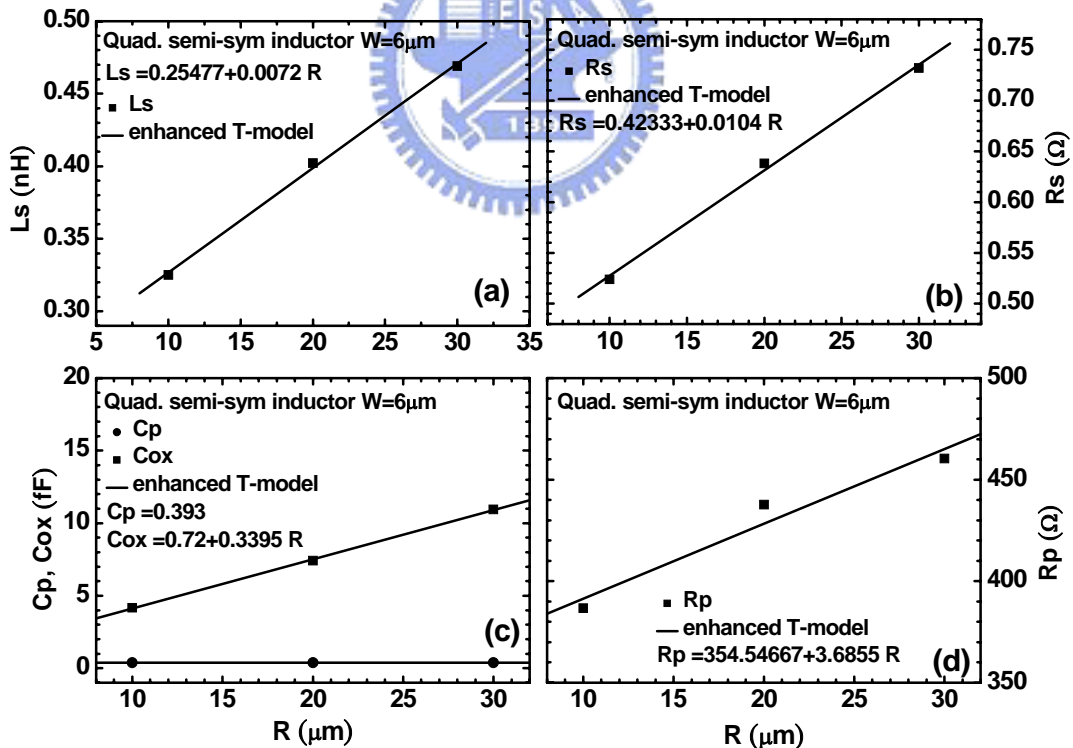


Figure 4.37 Enhanced T-model parameters for quadruple semi-symmetric inductors. Spiral coil RLC network parameters versus radius (a) L_s (b) R_s (c) C_p and C_{ox} (d) R_p .

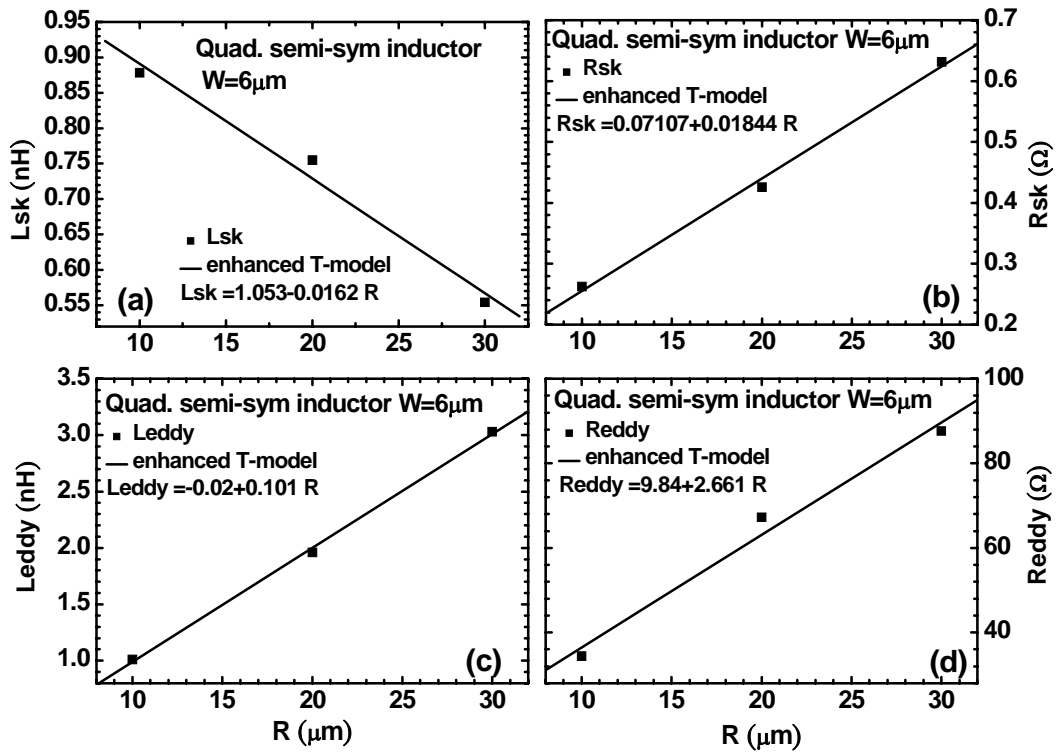


Figure 4.38 Enhanced T-model parameters for quadruple semi-symmetric inductors. Skin effect and proximity effect parameters versus radius (a) L_{sk} (b) R_{sk} (c) L_{eddy} (d) R_{eddy} , in spiral coil network.

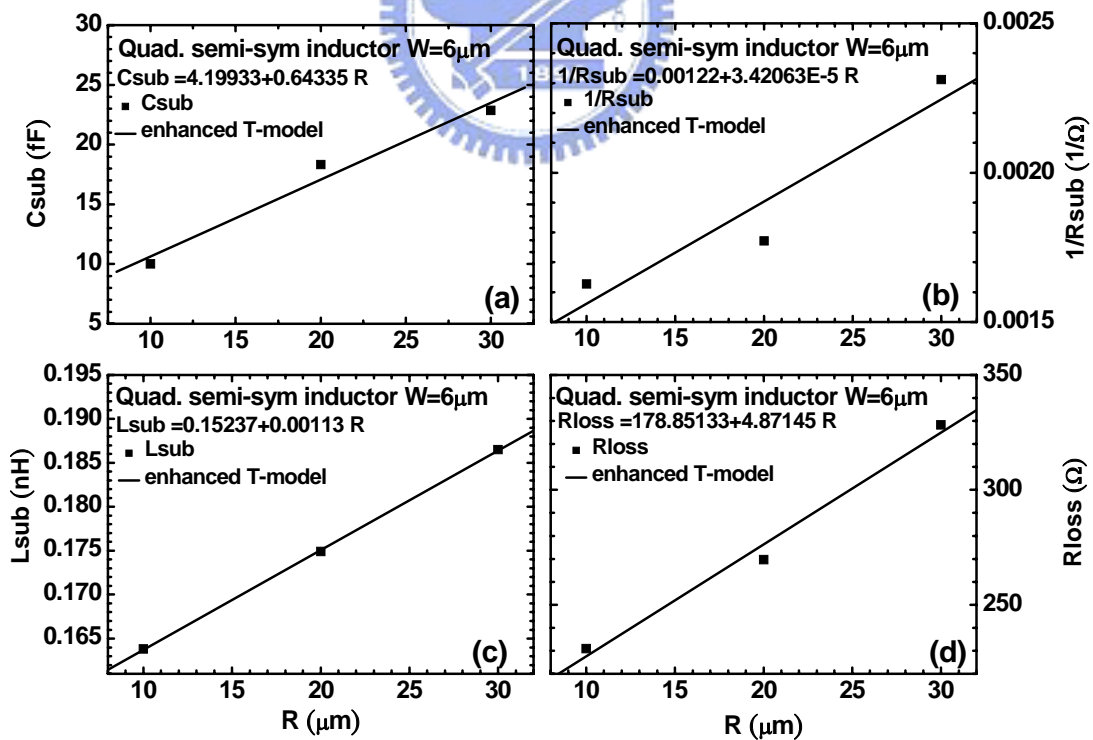


Figure 4.39 Enhanced T-model parameters for quadruple semi-symmetric inductors. Substrate RLC network parameters versus radius (a) C_{sub} (b) $1/R_{sub}$ (c) L_{sub} (d) R_{loss} .

Chapter 5

Conclusions and Future work

In this thesis, new symmetric inductors targeting for V-band applications have been designed and fabricated in 0.13 μm RF CMOS process. The measured characteristics can meet broadband performance with f_{SR} higher than 80 GHz for all dimensions in the design, which is above the target of 70GHz. EM simulation (HFSS) and the developed equivalent circuit model (enhanced T-model) can simulate the broadband characteristics over 110 GHz. A simple analytical model previously derived from T-model can precisely predict f_{SR} associated with various dimensions.

A couple of open questions identified from the silicon data in this design create several interesting topics for future work as follows. Inappropriately low Q was considered as the first weakness appearing in current design. Q above 10 is a common target specified for general RF integrated circuit design. However, the best record achievable from this work for Q_{max} is around 8.33, still below the common target $Q=10$. Inappropriately large $\text{Re}(Z_{\text{in}})$ associated with the small inductance $L=\text{Im}(Z_{\text{in}})/\omega$ is identified as the key problem. Skin effect and proximity effect are proposed as two primary mechanisms responsible for the increase of series resistance in a conductor under high frequency, reflected in soaring $\text{Re}(Z_{\text{in}})$ and falling Q. In section 3.4.1, frequency dependent models have been derived for calculating ac resistance R_{ac} composed of R_{skin} and $\overline{R_{\text{eddy}}}$ corresponding to skin effect and proximity effect in (3.36) and (3.37). Considering R_{skin} and $\overline{R_{\text{eddy}}}$ going an opposite trend in terms of material and geometric parameters, such as w , t , and σ , it reveals an extremely difficult problem in reducing R_{skin} and $\overline{R_{\text{eddy}}}$ simultaneously. 3D full-wave simulation will be carried out to do a serious verification on the derived models

for $R_{ac} = R_{skin} + \overline{R_{eddy}}$ under varying metal widths, thicknesses, conductivities w , t , σ , and operating frequencies. An immediate issue to be solved is the elimination of substrate loss in the structure setup for EM simulation. It is necessary to decouple conductor loss from substrate loss for verifying skin and proximity effects in conductors.

Improvement in Q and f_{SR} under a differential excitation is one of the most important advantages for adopting symmetric inductors in RF circuit design, particularly attractive in ultra-wide band applications. The high frequency characteristics measured from the fabricated symmetric inductors over 110 GHz prove the advantages through a comparison in Q and f_{SR} between single-ended and differentially driven excitations. However, the enhanced T-model in current form cannot reproduce the advantages measured under a differential excitation, such as Q_d versus Q_{se} . The simulation performed by enhanced T-model presents nearly the same Q and f_{SR} corresponding to single-ended and differential mode operations. The undesired mismatch suggests that an appropriate modification on current model is indispensable and identified as one of key topics in future work.

The third problem is concerning the large deviation in $\text{Re}(-1/Y_{21})$ between measurement and simulation – both HFSS and enhanced T-model. The deviation increases with frequency and becomes dramatic at very high frequency when $\text{Re}(-1/Y_{21})$ fall-off appears in measurement. The enhanced T-model in current form cannot predict $\text{Re}(-1/Y_{21})$ fall-off at high frequency, even beyond f_{SR} . The results suggest that substrate loss induced impact on $\text{Re}(-1/Y_{21})$ was under-estimated by the enhanced T-model, and a relevant modification on the substrate network model is required for an improvement. Note that an appropriate modification on the substrate network model going the right direction should solve the problems in differential mode and $\text{Re}(-1/Y_{21})$ simultaneously. An improved parameter extraction method with ensured consistency for different user is one more task in this aspect.

The last one considered important for future work is an improved de-embedding method for miniaturized inductors. The improvement should cover both de-embedding structure design and de-embedding algorithm.

Besides the mentioned problems for a continuous study in future work, the mechanisms underlying conductor loss and substrate loss, and the trade-off between high f_{SR} and large Q will be extensively explored to realize a deep understanding and facilitate an optimal inductor design for broadband and high Q .



References

- [1] M. Niknejad, and R. G. Meyer, Design, Simulation and Applications of Inductors and Transformers for Si RF ICs, Kluwer Academic 2000.
- [2] H.G. Booker, Energy in Electromagnetism. London/New York; Peter Peregrinus (on behalf of the IEE), 1981.
- [3] David M. Pozar, Microwave Engineering 3rd edition, University of Massachusetts at Amherst 2005.
- [4] David K. Cheng, Field and Wave Electromagnetics 2nd edition, University of Massachusetts at Amherst 1989.
- [5] J. R. Long, and M. A. Copeland, "The Modeling, Characterization, and Design of Monolithic Inductors for Silicon RF IC's," *IEEE Journal of Solid-State Circuits*, vol.32, no.3 pp.357-369, Mar. 1997.
- [6] C. P. Yue and S. S. Wong, "Physical modeling of spiral inductors on silicon", *IEEE Transactions on Electron Devices*, vol. 47, pp.560-568, March 2000.
- [7] M. Danesh, J.R. Long, R. Hadaway, and D. Harnage, "A Q-factor enhancement technique for MMIC inductors in silicon technology," in *Proc. IEEE Int. Microwave Symp. And RFIC Symp., Baltimore, MD, June 1998*, pp.217-220.
- [8] Sunderarajan S. Mohan, Maria del Mar Hershenson, Stephen P. Boyd, and Thomas H. Lee, "Simple Accurate Expressions for Planar Spiral Inductances," *IEEE Journal of Solid-State Circuits*, vol.34, no.10, October 1999.
- [9] C.-C. Tang, C.-H. Wu, and S.-I. Liu, "Miniature 3-D Inductors in Standard CMOS Process," *IEEE Journal of Solid-State Circuits*, vol. 37, no. 4, pp. 471-480, Apr. 2002.
- [10] C. P. Yue and S. S. Wong, "On-Chip Spiral Inductors with Patterned Ground Shields for Si-Based RF IC's", *IEEE Journal of Solid-State Circuits*, vol.33, no.5,

pp.743-752,May 1998.

- [11] Mina Danesh and John R. Long, "Differentially Driven Symmetric Microstrip Inductors," *IEEE Transactions on Microwave Theory and Techniques*, vol. 50, no. 1, pp. 332-341, Jan. 2002.
- [12] J.-H. Gau, S. Sang, R.-T. Wu, F.-J. Shen, H.-H. Chen, A. Chen, J. Ko, "Novel fully symmetrical inductor" *IEEE Electron Device Letters*, vol. 25, pp. 608-609, Sept. 2004.
- [13] C. B. Sia, K. S. Yeo, W. L. Goh, T. N. Swe, J. G. Ma, M. A. Do, J. S. Lin and L. Chan, "A Simple and Scalable Model for Spiral Inductors on Silicon," *Modeling and Simulation of Microsystem*, pp. 358-361, 2001.
- [14] Cao Yu, R.A. Groves, N.D. Zamdmer, J.-O. Plouchart, R.A. Wachnik, Huang Xuejue, T.-J. King, Hu Chenming, "Frequency-Independent Equivalent-Circuit Model for On-Chip Spiral Inductors," *IEEE Journal of Solid-State Circuits*, vol. 38, no. 3, pp. 419-426, March. 2003.
- [15] J. Gil, Shin Hyungcheol, "A Simple Wide-Band On-Chip Inductor Model for Silicon-Based RF ICs," *IEEE Transactions on Microwave Theory and Techniques*, vol. 51, no. 9, pp. 2023-2028, Sept. 2003.
- [16] J. C. Guo and T. Y. Tan "A Broadband and Scalable Model for On-chip Inductors Incorporating Substrate and Conductor Loss Effects," in 2005 RFIC Tech. Digest, June 12-14, Long Beach, CA, pp.593-596.
- [17] J. C. Guo and T. Y. Tan "A Broadband and Scalable On-chip Inductor Model Appropriate for Operation Modes of Varying Substrate Resistivities," in 2006 RFIC Tech. Digest, June 11-13, San Francisco, USA, pp.537-540.
- [18] J. C. Guo and T. Y. Tan "A Broadband and Scalable Model for On-chip Inductors Incorporating Substrate and Conductor Loss Effects," *IEEE Trans. on Electron Devices*, vol. 53, no.3, pp.413-421, Mar. 2006.

- [19] J. C. Guo and T. Y. Tan “ A Broadband and Scalable Lumped Element Model for Fully Symmetric Inductors under Single-Ended and Differentially Driven Operations,” *IEEE Trans. on Electron Devices*, vol.54, no.8, pp.1878-1888, August, 2007.
- [20] W. B. Kuhn, N. M. Ibrahim, “Analysis of Crowding Effects in Multiturn Spiral Inductors,” *IEEE Transactions on Microwave Theory and Techniques*, vol. 49, no. 1, pp. 31-38, Jan. 2001.
- [21] K. Y. Tong and C. Tsui, "A Physical Analytical Model of Multilayer On-Chip Inductors," *IEEE Transactions on Microwave Theory and Techniques*, vol. 53, no. 4, pp. 1143-1149, April 2005.
- [22] C.-C. Tang, C.-H. Wu, and S.-I. Liu, “Miniature 3-D Inductors in Standard CMOS Process,” *IEEE Journal of Solid-State Circuits*, vol. 37, no. 4, pp. 471-480, Apr. 2002.
- [23] John David Jackson, *Classical Electrodynamics*, August 10, 1998.

